



Aalborg Universitet

AALBORG UNIVERSITY
DENMARK

Structure, Crystallization and Optical Properties of Rare Earth Doped Oxyfluoride Glasses

Li, Zhencai

DOI (link to publication from Publisher):
[10.54337/aau473637702](https://doi.org/10.54337/aau473637702)

Publication date:
2022

Document Version
Publisher's PDF, also known as Version of record

[Link to publication from Aalborg University](#)

Citation for published version (APA):
Li, Z. (2022). *Structure, Crystallization and Optical Properties of Rare Earth Doped Oxyfluoride Glasses*. Aalborg Universitetsforlag. <https://doi.org/10.54337/aau473637702>

General rights

Copyright and moral rights for the publications made accessible in the public portal are retained by the authors and/or other copyright owners and it is a condition of accessing publications that users recognise and abide by the legal requirements associated with these rights.

- Users may download and print one copy of any publication from the public portal for the purpose of private study or research.
- You may not further distribute the material or use it for any profit-making activity or commercial gain
- You may freely distribute the URL identifying the publication in the public portal -

Take down policy

If you believe that this document breaches copyright please contact us at vbn@aub.aau.dk providing details, and we will remove access to the work immediately and investigate your claim.

**STRUCTURE, CRYSTALLIZATION AND
OPTICAL PROPERTIES OF RARE
EARTH DOPED OXYFLUORIDE
GLASSES**

**BY
ZHENCAI LI**

DISSERTATION SUBMITTED 2022



AALBORG UNIVERSITY
DENMARK

STRUCTURE, CRYSTALLIZATION AND OPTICAL PROPERTIES OF RARE EARTH DOPED OXYFLUORIDE GLASSES

by

Zhencai Li



AALBORG UNIVERSITY
DENMARK

Dissertation submitted 2022

Dissertation submitted: March 2022

PhD supervisor: Prof. Yuanzheng Yue,
Aalborg University

PhD committee: Associate Professor Mads Koustrup Jørgensen (chair)
Aalborg University, Denmark

Professor Christian Rüssel
Jena University, Germany

Professor Alex Hannon
Rutherford Appleton Laboratory, United Kingdom

PhD Series: Faculty of Engineering and Science, Aalborg University

Department: Department of Chemistry and Bioscience

ISSN (online): 2446-1636
ISBN (online): 978-87-7573-920-2

Published by:
Aalborg University Press
Kroghstræde 3
DK – 9220 Aalborg Ø
Phone: +45 99407140
aauf@forlag.aau.dk
forlag.aau.dk

© Copyright: Zhencai Li

Printed in Denmark by Stibo Complete, 2022



CV

Mr. Zhencai Li was born in Liaocheng, Shandong, P. R. China in May 1990. He obtained his Bachelor's degree in Materials Chemistry from Binzhou University (2015) and then got his Master's degree in materials Engineering from Kunming University of Science and Technology, P. R. China in 2018. He started his PhD study at Department of Chemistry and Bioscience in Aalborg University in April 2019, which is funded by China Scholarship Council (CSC). His research has been focused on structure, crystallization and optical properties of rare earth doped oxyfluoride glasses during his three years PhD study.

ENGLISH SUMMARY

Traditional oxyfluoride glass-ceramics (GCs) are a kind of multiphase material that contains fluoride crystallites embedded in the oxide glass matrix. These materials have attracted much attention as superior candidates for active rare-earth (RE) ions. Thus, a large number of optical applications based on RE ions doped oxyfluoride GCs have been developed during the recent three decades. However, the optical oxyfluoride GCs cannot achieve ultrahigh optical properties owing to the decrease of the light transmittance and the small-sized (below 100 nm) fluoride crystallites after heat treatment (HT). To overcome this limitation, this project aims to explore a new type of high transparent oxyfluoride GCs, in which large-sized fluoride crystals can be formed in the oxide glass matrix during quenching. The impact of chemical composition, subsequent HT and melting temperature on the structure, crystallization and optical properties of RE ions doped melt-quenching derived oxyfluoride GCs has been thoroughly investigated.

The impact of network modifiers $\text{LaF}_3/\text{La}_2\text{O}_3$ ratio on the glass structure, crystallization behavior, optical properties of Er^{3+} - Yb^{3+} doped melt-quenching derived oxyfluoride glasses and GCs were investigated. It was found that the area of the fluoride-rich phase in the phase-separated oxyfluoride glasses increases with increasing the modifiers ratio, which was agreed well with the results of MD simulations. This led to the decrease of crystallization activation energy of fluoride crystals and resulted in the formation of around 200 nm sized flower-like Ba_2LaF_7 crystals in the oxide glass matrix. However, the optical transmittance of the studied samples decreases with the increase of the ratio, whereas the Up-conversion luminescence (UCL) increases.

Appropriate heat treatment (HT) above the glass transition temperature (T_g) on the translucent melt-quenching derived 7LaF samples was conducted based on the above-mentioned results. Interestingly, the light transmittance of 7LaF samples increased with increasing HT temperature, which is in contrast to common sense, where the transmittance of oxyfluoride GCs lowered after HT. This anomalous phenomenon was attributed to the fact that the refractive index (n) of the residual glass matrix approaches that of Ba_2LaF_7 crystals via HT, and thereby light scattering is minimized. In addition, HT also enhanced the UCL of the studied samples. Thus, this HT strategy could inspire other host materials.

The effect of four melting temperatures on the properties of four melt-quenching derived oxyfluoride glass and GCs was investigated. It was found that the derived sample became more heterogeneous with lowering the melting temperature, and this enhanced the formation of Ba_2LaF_7 crystals. Consequently, the light transmittance of the GCs decreased, whereas the UCL increased. Upon HT, the crystallinity of the heat-treated samples was increased, leading to the enhancement of UCL and the

variation of light transmittance. Thus, glass properties can be tailored by a combined approach, i.e., by varying both the melting temperature and HT.

The impact of YF_3/LaF_3 ratio on the glass properties of the melt-quenching derived oxyfluoride GCs was also investigated. It was found that a series of fluoride crystals such as complex fluoride crystals and BaYF_5 crystals can be formed during quenching via adjusting the composition. Additionally, the derived samples gradually became transparent and the 3La4Y sample containing complex fluorite crystals exhibited the highest UCL intensity. This indicated that it could be a more promising host material compared with 7LaF sample. Furthermore, the temperature sensing performance of the heat-treated 7YF sample was evaluated, the outstanding performances mean the heat-treated 7YF sample is an excellent temperature-sensing material.

DANSK RESUME

Traditionelle oxyfluorid keramiske glas (GCs) er et multifase materiale som indeholder fluorid krystalliter indlejret i en oxid glas matrix. Disse materialer har tiltrukket meget opmærksomhed for deres evne til at inkorporere sjældne jordartsmetal (RE) ioner. På baggrund af dette har der i de seneste tre årtier blevet udviklet et stort antal af optiske teknologier baseret på RE ioner. Dog kan optiske oxyfluorid GCs ikke opnå ultrahøje optiske egenskaber på baggrund af en sænkelse af optisk transmission. Dette tab forekommer af at varmebehandlingen (HT) og krystalliternes størrelse (mindre end 100 nm). For at overkomme denne begrænsning vil dette projekt undersøge en ny type af høj transmissions oxyfluorid GCs. Disse nye GCs har store fluoride krystaller som bliver dannet i oxid glas matrixen under køling. Effekten af kompositionen, HT og smeltning, på strukturen, krystallisering og optiske egenskaberne af RE ion dopet oxyfluorid GCs er blevet undersøgt.

Effekten af $\text{LaF}_3/\text{La}_2\text{O}_3$ netværksmodifikator forholdet på glas struktur, krystalliserings karakteristika, optiske egenskaber af Er^{3+} - Yb^{3+} dopet oxyfluorid glas og GCs blev undersøgt. Det blev observeret at området af den fluorid rige fase i faseseparatorer oxyfluorid glas øges med øget $\text{LaF}_3/\text{La}_2\text{O}_3$ forhold. Dette fund stemmer godt overens med resultater fra MD-simuleringer. Dette medførte et tab i aktiveringsenergien for krystallisering af fluorid krystaller og resulterede i formering af 200 nm store blomster formet Ba_2LaF_7 krystaller i oxid glas matrixen. Den optiske transmission faldt med øget $\text{LaF}_3/\text{La}_2\text{O}_3$ forhold, mens at op-konvertings luminescens (UCL) steg. Passende HT over glasovergangstemperaturen (T_g) af gennemsigtige bratkølet 7LaF prøver var udført baseret på de ovennævnte resultater. Lystransmissionen af 7LaF prøverne steg med øget HT-temperatur. Dette atypiske fænomen er tilskrevet at brydningsindekset (n) af den resterende glasmatrix tilnærmer sig brydningsindekset for Ba_2LaF_7 ved HT og dermed minimeres lys spredningen. Derudover øgede HT også UCL af prøverne. Dermed kan denne HT-strategi bruges som inspiration for andre værtmaterialer.

Effekten af fire smeltetemperaturer på egenskaberne af oxyfluorid glas og GCs blev undersøgt. Prøverne blev mere heterogene ved lavere smeltetemperatur, hvilket øgede formeringen af Ba_2LaF_7 krystaller. Som konsekvens af dette faldt lystransmissionen af GCs imens at UCL steg. Krystalliniteten steg under HT, hvilket medførte forbedringen af UCL og variationen i lystransmission. Dette viser at glasegenskaber kan tilpasses gennem en kombineret tilgang ved at variere både smelte temperaturen og HT.

Effekten af YF_3/LaF_3 forholdet på glas egenskaber af oxyfluorid GCs blev også undersøgt. Ved at variere kompositionen af reaktanter er det muligt at danne fluorid krystaller, eksempelvis komplekse fluorid krystaller og BaYF_5 krystaller, under glas dannelsen. Prøverne blev gradvist mere transparente og 3La4Y prøverne der

indeholder komplekse fluorid krystaller udviste den højeste UCL styrke. Dette indikerer at disse materialer er potentielt mere lovende vært materialer sammenlignet med 7LaF prøven. Derudover blev varmemølings evnen af HT 7YF prøven undersøgt, hvor dens enestående egenskaber viser at HT 7YF prøven er velegnet som varmemålende materialer.

ACKNOWLEDGEMENTS

I would like to thank a great number of people for their help with my PhD study. I cannot imagine to accomplish my PhD study and research without their kind support. First of all, I am very grateful to my supervisor Prof. Dr. Yuanzheng Yue. I met and knew him five years ago when I attended an academic conference in China, and I was thrilled by his enthusiasm, scientific perception and rigor. I enjoyed the time with him for sharing research ideas, discussing experimental results, revising our papers as well as drinking a cup of coffee. I am very grateful to his insightful guidance during my entire PhD study.

Secondly, I want to give my thank to my collaborator Professor Yanfei Zhang from Qilu University of Technology for her advice. I was inspired by her creativity and scientific insight. Discussions with her are always joyful and helpful. I benefited greatly from her suggestions and encouragement whenever I meet challenges. Her writing skills impress me and stimulate me to improve my writing ability.

Thirdly, I would like to express my gratitude to my colleagues in the Section of Chemistry: Assoc. Prof. Vittorio Boffa, Prof. Morten M. Smedskjær, Assoc. Prof. Donghong Yu, Assoc. Prof. Morten Christensen, Assoc. Prof. Thorbjørn Nielsen, Assoc. Prof. Mads Jørgensen, Assoc. Prof. Cejna Quist-Jensen, Asst. Prof. Aamer Ali, Dr. Ang Qiao, Dr. Martin B. Østergaard, Dr. Yang Shen, Dr. Rasmus R. Petersen, Dr. Chao Zhou, Dr. Usuma Naknikham, Dr. Kacper Januchta, Dr. Malwina Stepniewska, Dr. Ming Liu, Dr. Anne Sophie Jødal, Dr. Theany To, Dr. Chengwei Gao, Dr. Pengfei Liu, Johan F. Christensen, Dr. Mikkel Bødker, Dr. Junjun Tan, Rasmus S.K. Madsen, Søren S. Sørensen, Peter Jensen, Wessel M.W. Winters, Jiajia Yan, Linling Tan, Xinxin Chen, Xianzheng Ma, Wei Xu, Wei Fan, Xiangting Ren, Annemarie Davidsen, Anne Flensborg, Lisbeth Wybrandt, Michelle Mortensen, Mette Haferbier, Timo Kirwa, Camilla Hvass-Raun, Helen Kjerstein Kristensen and Sara Jellesmark.

I also had a great time working at Qilu University of Technology owing to many excellent and supportive co-workers. I am very grateful to Prof. Jianxing Shen, Prof. Yanfei Zhang, Prof. Shujiang Liu, Prof. Chaofeng Zhu, Assoc. Prof. Qiujuan Zheng, Assoc. Prof. Yuebo Hu, Dr. Yang Shen, Dr. Jiayan Zhang, Dr. Xue Wang, Shibin Qi, Xiangyu Li for the great help in both research and life when I study in there. I also really enjoy working together with them and I express my appreciation to all the researchers and scientists there. I hope they will enjoy their academic life and have a shining future. The experiences are so memorable that I will never forget the fantastic moments there.

I also appreciate my collaborators for their scientific assistance and helpful discussions. They are Assoc. Prof. Lars Jensen, Assoc. Prof. Deyong Wang from Aalborg University, Prof. Haizheng Tao, Dr. Ang Qiao from Wuhan University of Technology. Prof. Jianbei Qiu, Prof. Zhengwen Yang, Prof. Xuhui Xu, Dr. Yong Yang, Engr. Dacheng Zhou, Zhangwen Long, Hao Wu, Rui Zhu, Ke Zhang, Weihui Shen and Dazhao Wang from Kunming University of Science and Technology. Prof. Jincheng Du from University of North Texas, US. Prof. Jianrong Qiu, Assoc. Prof. Xusheng Qiao, Dr Junjie Zhao and Xiuxie Xu from Zhejiang University. Prof. Jinjun Ren, Jiachuan Ni, Tongyao Zhao, Jingbo Yu, Chunying Chen from Shanghai Institute of Optics and Fine Mechanics, Chinese Academy of Sciences. It is my great luck to work with them. I also thank the support from China Scholarship Council (CSC). It provides me with a great opportunity to conduct my research project with many talented researchers and scientists.

Furthermore, I am grateful to my close friends: Wenfu, Na, Kaiqi, Miaomiao, Guoqiang, Jianfang, Juan, Zongzhe, Geng, Wei, Hanwen, Xiaoyuan, Zhaoda, Yida, Yifeng, Tianbao, Baoze, Wenzhao, Yang, Yi, Fan, Guohan, Li, Lianghai and Siya.

In the end, I give my sincere appreciation to my wife Jinfeng Huang, my son Lukas Li and my parents. I really appreciate their support and I could not imagine how I would be without their encouragement and love.

LIST OF ABBRIVATIONS

PG	Precursor glass
GC	Glass-ceramic
GCs	Glass-ceramics
a.u.	Arbitrary unit
BO	Bridging oxygen
NBO	Non-bridging oxygen
XRD	X-ray diffraction
FCC	Face-centered cubic
PDF	Powder diffraction file
CIF	Crystallographic information files
DSC	Differential scanning calorimetry
T_g	Onset temperature of glass transition
T_{c1}	Onset temperature of the first crystallization
T_{c2}	Onset temperature of the second crystallization
T_c	Onset temperature of the main crystallization
T_{m1}	Onset temperature of the first melting point
T_{m2}	Onset of the second melting temperature
ΔH	Crystallization enthalpy
$T_{\text{scan-max}}$	Maximum scanning temperature
MD	Molecular dynamic
SEM	Scanning electron microscopy
TEM	Transmission electron microscopy
STEM	Scanning transmission electron microscopy
HAADF	High-Angle Annular Dark-Field
ACTEM	Aberration-corrected transmission electron microscopy
HRTEM	High-resolution Transmission Electron Microscopy
EDS	Energy-dispersive X-ray spectrometer or spectra
MAS	Magic angle spinning
NMR	Nuclear magnetic resonance
Al(IV)	Four-coordinated aluminum
XPS	X-ray photo spectroscopy
UV	Ultraviolet-visible spectroscopy
Abs	Absorption spectrum (spectra)
UCL	Up-conversion luminescence
LD	Laser diode
n	Refractive index
n_d	n at 587.56 nm
Δn_d	n_d difference
FIR	Fluorescence intensity ratio
TCELS	Thermally coupled energy levels
T	Absolute temperature

S_R	Relative temperature sensitivity
ΔE	Effective energy gap between $^2\text{H}_{1/2}$ and $^4\text{S}_{3/2}$
C	Temperature-independent constant
K_B	Boltzmann constant

TABLE OF CONTENTS

Chapter 1. Introduction.....	1
1.1. Background and Challenges.....	1
1.2. Objectives.....	2
1.3. Thesis Content.....	3
Chapter 2. Experimental Sections	5
2.1. Synthesis	5
2.1.1. Composition-Dependent Oxyfluoride Glasses and Glass-Ceramics	5
2.1.2. Melting Temperature-Based Oxyfluoride Glasses and Glass-Ceramics ..	5
2.2. Characterization Methods	6
2.2.1. X-ray Diffraction (XRD).....	6
2.2.2. Differential Scanning Calorimetry (DSC).....	6
2.2.3. Raman Spectroscopy	6
2.2.4. Ultraviolet–Visible (UV-VIS) Absorption Spectroscopy.....	6
2.2.5. Molecular Dynamics (MD) Simulations	7
2.2.6. Scanning Electron Microscopy (SEM).....	7
2.2.7. Transmission Electron Microscopy (TEM).....	7
2.2.8. Solid-State Nuclear Magnetic Resonance (NMR)	7
2.2.9. Refractive Index (n)	8
2.2.10. Up-Conversion Luminescence (UCL).....	8
2.2.11. Fluorescence Decay Lifetime.....	8
Chapter 3. Oxyfluoride Glasses and Glass-Ceramics with Varying La₂O₃/LaF₃ Ratio	9
3.1. Characterization of Melt-Quenching Derived Oxyfluoride Glasses and Glass-Ceramics	9
3.1.1. Glass Structural Analyses.....	9
3.1.2. Local Structural Analysis	11
3.1.3. Thermodynamic Analysis	12
3.1.4. MD Simulation Analysis.....	14
3.1.5. Morphology of Glasses and Glass-Ceramics	16

3.2. Optical Properties Melt-Quenching Derived Oxyfluoride Glasses and Glass-Ceramics	18
3.2.1. Absorption and Transmittance Spectra	18
3.2.2. UCL and Fluorescence Decay Lifetime	19
3.3. Summary	20
Chapter 4. Impact of Heat Treatment on Properties of Oxyfluoride Glass-Ceramics	21
4.1. Optical, Thermal and Microstructural Analyses	21
4.1.1. Optical Transparency Analysis	21
4.1.2. Thermodynamic Analysis	22
4.1.3. Microstructural Analysis	23
4.1.4. Structural Origin and Evolution of Crystals	26
4.2. Origin of the Increase of Transmittance	28
4.3. UCL Performances	32
4.4. Summary	33
Chapter 5. Melting Temperature-Dependent Oxyfluoride Glasses and Glass-Ceramics	35
5.1. Characterization of Melt-Quenching Derived Oxyfluoride Glasses and Glass-Ceramics	35
5.1.1. Thermodynamic Analysis	35
5.1.2. Glass Structural Analyses	38
5.1.3. Morphology of Glasses and Glass-Ceramics	40
5.2. Optical Properties	43
5.2.1. Transmittance Spectra	43
5.2.2. UCL Spectra	44
5.3. Summary	44
Chapter 6. Oxyfluoride Glass-Ceramics with Varying LaF₃/YF₃ Ratio	47
6.1. Thermodynamic Analysis	47
6.2. Glass Structural Analyses	48
6.3. Morphology Features	50
6.4. Optical Performances	51
6.5. Application of Non-Contact Optical Temperature Sensing	51
6.6. Summary	55

Chapter 7. Conclusions and Perspective	57
7.1. Conclusions.....	57
7.2. Perspective	58
Biography.....	59
List of Publications.....	69

TABLE OF SCHEME

Scheme 1-1 Scheme of the nanocrystallization mechanism in phase-separated oxyfluoride glasses (left one) and two classical types of phase separation in oxyfluoride glasses (right one)..... 1

TABLE OF FIGURES

Figure 3-1 (a) XRD patterns and (b) Raman spectra of 0LaF, 2LaF, 4LaF, 6LaF and 7LaF samples, respectively.	9
Figure 3-2 Structure characterizations by MAS NMR. ^{29}Si (a), ^{27}Al (b), and ^{19}F (c) spectra of 0LaF, 2LaF, 4LaF, 6LaF and 7LaF samples, respectively. \star : spinning sidebands.....	11
Figure 3-3 (a) Overall DSC curves of all the samples. Each enlarged DSC curve of : (b) 0LaF, (c) 2LaF, (d) 4LaF, (e) 6LaF and (f) 7LaF samples, respectively. The onset temperatures of T_g , T_{c1} , T_{c2} , T_c , T_{m1} and T_{m2} are marked in each figure.	13
Figure 3-4 MD simulated glass structure of 0LaF (a), 2LaF (b), 4LaF (c) and 7LaF (d) samples composed of network forming SiO_4 and AlO_4 tetrahedra and network modifiers. Note that Er^{3+} and Yb^{3+} are replaced by La^{3+} to perform MD simulations.	14
Figure 3-5 Coordination number variation of Al^{3+} (a), Ba^{2+} (b), La^{3+} (c) Na^+ (d) and Si^{4+} (e) with increasing LaF_3 content.	15
Figure 3-6 SEM images of 0LaF (a), 2LaF (b), 4LaF (c) and 7LaF (d) samples, respectively.	16
Figure 3-7 SEM images obtained from backscattered electron mode of 0LaF (a), 4LaF (b) and 7LaF (c) samples without etching by HF acid, respectively.	17
Figure 3-8 Absorption spectra (a) and light transmittance spectra (b) with insert photo images (from left to right) of 0LaF, 2LaF, 4LaF, 6LaF and 7LaF samples, respectively.	18
Figure 3-9 UCL spectra (a) and decay lifetime of Er^{3+} in $^2\text{H}_{11/2}$ (b), $^4\text{S}_{3/2}$ (c) and $^4\text{F}_{9/2}$ (d) states of 0LaF, 2LaF, 4LaF, 6LaF and 7LaF samples, respectively.....	19
Figure 4-1 (a) Absorption spectra of 7LaF samples before and after HT at 600, 640, and 680 °C for 4 hours. (b) Transmittance spectra of the above-mentioned samples. Inset: Photo images of 7LaF sample and three 7LaF samples heat-treated at 600, 640, and 680 °C for 4 hours, respectively (from left to right).....	21
Figure 4-2 DSC output of 7LaF sample and three 7LaF samples heat-treated at 600, 640 and 680 °C, respectively, for 4 hours. T_g , T_{c1} , T_c and T_{m1} are marked in the Figure. The area of the first exothermic peak (i.e., the hatched area) represents ΔH determined by the extent of the crystal formation in each sample.	22
Figure 4-3 (a) XRD patterns and (b) Normalized Raman spectra of 7LaF sample and three 7LaF samples heat-treated at 600, 640 and 680 °C, respectively, for 4 hours, where the vibrational modes and the peak positions are indicated.....	24
Figure 4-4 MAS NMR spectra of ^{27}Al (a), ^{29}Si (b) and ^{19}F (c) spectra of 7LaF sample and three 7LaF samples heat-treated at 600, 640 and 680 °C, respectively. \star : spinning sidebands.....	25
Figure 4-5 SEM images of 7LaF sample (a) and three 7LaF samples (b-d) heat-treated at 600, 640, 680 °C for 4 hours, respectively.	26

Figure 4-6	ACTEM images of 7LaF sample (the first row) and three 7LaF samples heat-treated at 600, 640, 680 °C for 4 hours, respectively (See the second, third and fourth row). The first column: Overview images; The second column: Lattice structure of the flower-like Ba ₂ LaF ₇ crystals; The third column: Electron diffraction of the domains (see inset) selected from red dashed circles in their overview images. The fourth column: Formation of the tiny spherical crystals and their evolution with HT temperature (see the black dashed squares in the overview images). Insets: Lattice structure of the tiny spherical crystals selected from black dashed squares.	27
Figure 4-7	(a) n as a function of the light wavelength for 7LaF sample and three heat-treated samples. (b) n_d at the wavelength of 588 nm (black star symbols) and Δn_d between the studied samples and the Ba ₂ LaF ₇ crystallites (red sphere symbols). The error range of n : ± 0.0001	28
Figure 4-8	HAADF-STEM and EDS-mapping micrographs of 7LaF sample (the first row) and three 7LaF samples heat-treated at 600, 640, 680 °C for 4 hours, respectively (the second, third and fourth row). The third column: HAADF-STEM images; EDS-mapping elements: Ba, La and F (see the second, third and fourth columns, respectively).	30
Figure 4-9	¹³⁹ La WURST-QCPMG NMR spectra of both 7LaF-RE free sample with the molar composition of 45SiO ₂ -15Al ₂ O ₃ -12Na ₂ O-21BaF ₂ -7LaF ₃ and 7LaF-RE free sample heat-treated at 640 °C for 4 hours, respectively.	31
Figure 4-10	UCL spectra (a) of 7LaF sample and three 7LaF samples heat-treated at 600, 640, 680 °C for 4 hours, respectively, and decay lifetime of Er ³⁺ in ² H _{11/2} (b), ⁴ S _{3/2} (c) and ⁴ F _{9/2} (d) states 7LaF sample and 7LaF samples heat-treated at 680 °C for 4 hours.	32
Figure 5-1	(a and b) DSC output curves of both the melt-quenching derived (PG1450, PG1500, PG1550 and PG1590) and the corresponding heat-treated samples (GC1450, GC1500, GC1550 and GC1590), respectively. The onset temperatures of T_g , T_{c1} , T_c , T_{m1} and T_{m2} are marked in Figure 5-1, respectively. The area of the first exothermic peak (i.e., the hatched area) represents ΔH determined by the extent of the crystal formation in each sample.	35
Figure 5-2	DSC output curves of PG1450 (a), PG1500 (b), PG1550 (c) and PG1590 (d) samples by repeated scan to $T_{scan-max}$ of 740, 700, 720, 690 °C, respectively, for three times at the same up-scan and down-scan rate of 10 °C/min.	37
Figure 5-3	XRD patterns of PG1450, PG1500, PG1550 PG1590, GC1450, GC1500, GC1550 and GC1590 samples, respectively.	38
Figure 5-4	Raman spectra of the melt-quenching derived (a) and the heat-treated samples (b), respectively.	39
Figure 5-5	²⁷ Al MAS NMR spectra of PG1450, PG1500, PG1550 and the PG1590 samples, respectively. (♣) denotes spinning sidebands.	40
Figure 5-6	ACTEM images of PG1450 (a), PG1590 (b), GC1450 (c), and GC1590 (d) samples, respectively.	41
Figure 5-7	SEM graphs of PG1450 (a), PG1590 (b), GC1450 (c), and GC1590 (d) samples, respectively. For GC1450, white flower-like domains and grey regions are	

Ba ₂ LaF ₇ crystals and tiny spherical Ba ₂ LaF ₇ nanocrystals, respectively. For GC1590, small white dot regions are new-formed Ba ₂ LaF ₇ nanocrystals embedded in glass matrix (large black areas).....	42
Figure 5-8 Transmittance spectra of the melt-quenching derived samples (a) and the corresponding heat-treated samples (b), respectively.	43
Figure 5-9 UCL spectra of Er ³⁺ -Yb ³⁺ co-doped melt-quenching derived samples and the heat-treated samples, respectively.....	44
Figure 6-1 DSC curves of 7LaF, 5La ₂ Y, 3La ₄ Y, 1La ₆ Y and 7YF samples, respectively. Onset temperatures of T_g , T_{c1} , T_{c2} , T_c , T_{m1} , T_{m2} and T_{m3} are marked in Figure, respectively.....	47
Figure 6-2 XRD patterns of 7LaF, 5La ₂ Y, 3La ₄ Y, 1La ₆ Y and 7YF samples, respectively.	48
Figure 6-3 Normalized Raman spectra of 7LaF, 5La ₂ Y, 3La ₄ Y, 1La ₆ Y and 7YF samples, respectively.	49
Figure 6-4 SEM images obtained from backscattered electron mode of 7LaF (a) and 7YF (b) samples without etching by HF acid, respectively.	50
Figure 6-5 Transmittance spectra (a) and UCL spectra (b) of Er ³⁺ -Yb ³⁺ co-doped 7LaF, 5La ₂ Y, 3La ₄ Y, 1La ₆ Y and 7YF samples, respectively.	51
Figure 6-6 Normalized UCL spectra of the heat-treated 7YF sample at the temperature range from 313 to 473 K.	52
Figure 6-7 (a) Black fitting curve: Temperature dependence of FIR between $^2H_{11/2} \rightarrow ^4I_{15/2}$ and $^4S_{3/2} \rightarrow ^4I_{15/2}$ transitions of Er ³⁺ of the 7YF sample. (b) Red fitting curve: The sensitivity S_R of the heat-treated 7YF sample.	53
Figure 6-8. Temperature-induced switching of FIR of the heat-treated 7YF sample (alternating between 313 and 473 K).	54

TABLE OF FIGURES

Table 3-1 The onset temperatures of T_g , T_{c1} , T_{c2} , T_c and T_{m1} and T_{m2} of the 0LaF, 2LaF, 4LaF, 6LaF and 7LaF samples, respectively..... 12

Table 4-1 The onset temperatures of T_g and T_{c1} of both 7LaF and 7LaF samples subjected to HT at 600, 640, and 680 °C for 1, 2 and 4 hours, respectively. 23

Table 4-2 Crystallinity in both 7LaF and the three 7LaF samples heat-treated at 600, 640, and 680 °C for 4 hours, respectively. 24

Table 4-3 n and Density of the investigated 7LaF sample and three heat-treated samples..... 29

Table 5-1 The onset temperatures of T_g , T_{c1} , T_c , T_{m1} and T_{m2} of the melt-quenching derived and the heat-treated samples, respectively. 36

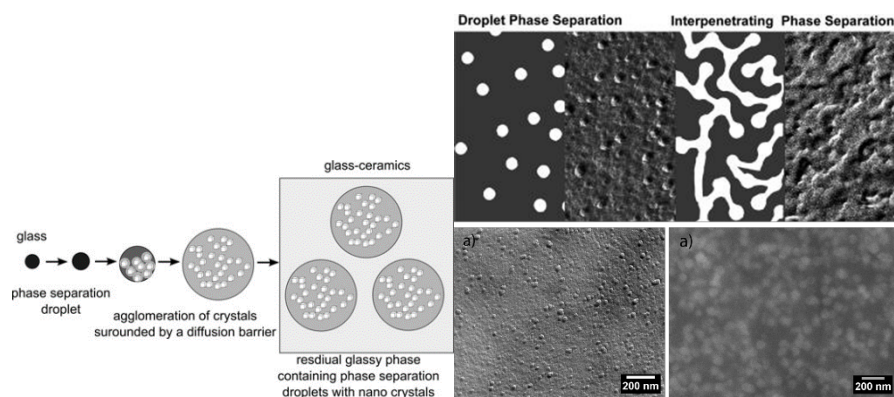
Table 6-1 The onset temperatures of T_g , T_{c1} , T_{c2} , T_c , T_{m1} , T_{m2} and T_{m3} of 7LaF, 5La2Y, 3La4Y, 1La6Y and 7YF samples, respectively..... 48

Table 6-2 ΔE and S_R of several typical FIR-based optical temperature sensors based on UCL from $^2H_{11/2}$ and $^4S_{3/2}$ levels of Er^{3+} ions. 54

CHAPTER 1. INTRODUCTION

1.1. BACKGROUND AND CHALLENGES

Rare earth (RE) ions doped oxyfluoride glass-ceramics (GCs) have been regarded as promising optical materials for optical amplifiers (1), multicolor displays (2), up-conversion (UC) fibers (3), random lasers (4), and optical thermometry (5) since they were first reported by Wang and Ohwaki in 1993 (6). Although the characteristics applications of RE ions doped oxyfluoride GCs are gradually getting mature, advanced technologies and new types of oxyfluoride GCs are still being explored.



Scheme 1-1 The possible crystallization mechanism scheme in phase-separated oxyfluoride glasses (left one) and two classical types of phase separation in oxyfluoride glasses (right one). Figure Taken from Ref. (10)(12)

Oxyfluoride GCs are composite multiphase materials containing fluoride crystallites and oxide glass matrix, where the fluoride crystals are embedded in the oxide glass matrix (7). They are generally prepared by appropriately heat-treating the corresponding oxyfluoride precursor glasses (PGs), which are formed by quenching a liquid from above their liquid temperature to avoid crystallization (8). Compared with oxyfluoride PGs, oxyfluoride GCs usually exhibit enhanced mechanical, thermal and optical properties (9)(10). Therefore, the crystallization in oxyfluoride PGs has undoubtedly become a key research direction. It is reported by Prof. Christian Rüssel in the previous studies (11) that the amorphous phase separation (12)(13), e.g., the fluoride-rich and the aluminosilicate oxide-rich glass phases, would assist the formation of fluoride crystallites in oxyfluoride PGs (14). In other words, the fluoride crystallites can be precipitated from the fluoride-rich phases in the oxyfluoride PGs via appropriate heat treatment (HT) (15). In addition, to understand and predict glass structure and phase transitions of oxyfluoride PGs, Molecular Dynamics (MD) simulation has been proposed and developed by Prof. Jincheng Du. Despite this, the

physical and chemical properties of the separated glass phases have not yet been conclusively determined, and the mechanism of crystallization in those phases remains unclarified. Thus, it is necessary to combine experiments and MD simulations to further clarify the relation between phase separation and crystallization.

On the other hand, many studies focus on the development of functional RE ions doped oxyfluoride GCs for optical applications. Usually, large-sized fluoride crystals and high transparency are vital for enhancing the optical properties of RE ions doped oxyfluoride GCs. However, the growth of fluoride crystals in oxyfluoride PGs is limited by diffusion barriers forming around crystals (16)(17). Thus, it is difficult to precipitate large-sized fluoride crystals and obtain high fraction of fluoride crystals in oxyfluoride PGs (18)(19). Furthermore, the optical transmittance of oxyfluoride GCs is lower than that of their corresponding oxyfluoride PGs since the former has stronger optical absorption and light scattering than the latter. According to the Rayleigh-Gans theory (20), when crystallinity is relatively low and the size of the fluoride crystallites is well below the wavelength of the incident light, the attenuation due to light scattering is negligible (21). As a result, if the fluoride crystallites are less than 30 nm, most of the oxyfluoride GCs will exhibit ultrahigh transmittance due to the limited light scattering and absorption (7). However, both the optical absorption and light scattering loss of oxyfluoride GCs increase rapidly with increasing the fluoride crystallite size and the crystallinity, resulting in reduced light transmittance. On the other hand, if the fluoride crystallites are too small, they cannot accommodate a large amount of RE ions required to achieve high up-conversion luminescence (UCL) efficiency (22)(23)(24). In the end, it is still a challenge to gain large-sized fluoride crystallites, high crystallinity, and high transmittance in oxyfluoride GCs via HT. To overcome this challenge, the melt-quenching derived oxyfluoride GCs, that is, the desired fluoride crystals formed in the oxyfluoride PGs during quenching, are explored by researchers (5). Thus, numerous melt-quenching derived oxyfluoride GCs containing different fluoride crystals such as NaLuF₄, KTb₂F₇, and K₃YF₆, have been reported in recent years (25)(26)(27). However, this still cannot obtain aimed oxyfluoride GCs after HT owing to low crystallinity and optical transmittance. Therefore, the development of new types of oxyfluoride GCs with high transparency, large-scaled fluoride crystals, high crystallinity has been attracting more attention in recent years. Concerning the relation between amorphous phase separation and crystallization, amorphous phase separation might be the key factor to design the required oxyfluoride GCs for optical devices.

1.2. OBJECTIVES

This PhD project aims to investigate some puzzles that remained in oxyfluoride GCs, such as the microstructure of melt-quenching derived oxyfluoride GCs and the formation mechanisms of fluoride crystals in phase separation regions. More specifically, this thesis focuses on adjusting the type of glass network modifiers in the chemical composition to investigate the glass structure and crystallization behavior of

the melt-quenching derived oxyfluoride GCs. Furthermore, this thesis also attempts to regulate melting temperature and conduct proper HT to further understand their relations. In short, by adjusting the chemical composition and subsequent HT to minimize the differences in refractive index (n) between fluoride crystal and residual glass matrix, an ideal optical host material with high transparency, high crystallinity and large-scale fluoride crystals is found in this thesis. The main objectives of this thesis are summarized as below:

- Formation of composition-dependent melt-quenching derived oxyfluoride glasses and GCs
- Conduct HT on melt-quenching derived oxyfluoride GCs to enhance the optical properties
- Increasing melting temperature to tailor melt-quenching derived oxyfluoride glasses and GCs
- Adjusting the chemical composition to obtain different melt-quenching derived oxyfluoride GCs
- Heat-treated oxyfluoride GC for the optical application of temperature sensing

1.3. THESIS CONTENT

This thesis contains five journal papers (two published papers, one submitted paper and two papers in preparation). These five papers correspond to Chapter 3, Chapter 4, Chapter 5 and Chapter 6. The papers listed below constitute the thesis content, which will be referred to by their roman numerals:

I. **Li, Z.**, Zhou, D., Jensen, L. R., Qiu, J., Zhang, Y., & Yue, Y., Er³⁺-Yb³⁺ ions doped fluoro-aluminosilicate glass-ceramics as a temperature-sensing material. *Journal of American Ceramic Society*, 104, 4471-4478 (2021).

II. **Li, Z.**, Chen, C., Shen, W., Zhou, D., Jensen, L. R., Qiao, X., Ren, J., Du, J., Zhang, Y., Qiu, J., & Yue, Y., Transformation from Translucent into Transparent Rare Earth Ions Doped Oxyfluoride Glass-Ceramics with Enhanced Luminescence. *Advanced Optical Materials*, DOI: 10.1002/adom.202102713 (2022) (in press).

III. **Li, Z.**, Tan, L., Chen, C., Zhou, D., Jensen, L. R., Ren, J., Zhang, Y., Qiu, J., & Yue, Y., The impact of melting temperature on the properties of rare earth doped oxyfluoride glass/glass-ceramics (under review).

IV. **Li, Z.**, Chen, C., Zhou, D., Jensen, L. R., Qiao, X., Du, J., Zhang, Y., Ren, J., Qiu, J., & Yue, Y., Impact of network modifiers on the formation of rare earth ions doped melt-quenching derived oxyfluoride glass-ceramics (in preparation).

V. **Li, Z.**, Zhang, K., Zhou, D., Jensen, L. R., Zhang, Y., Ren, J., Qiu, J., & Yue, Y., Impact of the LaF_3/YF_3 ratio on the properties of rare earth ions doped melt-quenching derived oxyfluoride glass-ceramics (in preparation).

CHAPTER 2. EXPERIMENTAL

SECTIONS

In this Chapter, sample preparation methods and the characterization techniques of melt-quenching derived oxyfluoride glasses and GCs are presented.

2.1. SYNTHESIS

All the chemicals (99.99%) used for the synthesis are bought from the company of Aladdin. All the samples were prepared from Kunming University of Science and Technology by the author in this thesis. All the structures of samples were verified by matching XRD patterns with simulated ones and reported ones.

2.1.1. COMPOSITION-DEPENDENT OXYFLUORIDE GLASSES AND GLASS-CERAMICS

The composition-dependent oxyfluoride glasses and GCs were prepared by a traditional melt-quenching method (28). The molar compositions of composition-dependent samples are $45\text{SiO}_2\text{-}15\text{Al}_2\text{O}_3\text{-}12\text{Na}_2\text{O-}21\text{BaF}_2\text{-(}7\text{-x)La}_2\text{O}_3\text{-xLaF}_3\text{-}0.5\text{ErF}_3\text{-}1\text{YbF}_3$ ($x = 0, 2, 4, 6$ and 7 , respectively) and $45\text{SiO}_2\text{-}15\text{Al}_2\text{O}_3\text{-}12\text{Na}_2\text{O-}21\text{BaF}_2\text{-(}7\text{-x)LaF}_3\text{-xYF}_3\text{-}0.5\text{ErF}_3\text{-}1\text{YbF}_3$ ($x = 0, 2, 4, 6$ and 7 , respectively). In detail, 10 g raw material for each sample was mixed in proportion and put into an alumina crucible with a lid, which was heated in a muffle furnace under air atmosphere to $1450\text{ }^\circ\text{C}$ for 45 min, respectively. Then each melt was cast quickly onto a steel plate preheated at $300\text{ }^\circ\text{C}$. Subsequently, to remove the permanent thermal stress, each PG sample was annealed at $500\text{ }^\circ\text{C}$ for 8 hours and then slowly cooled down to room temperature inside the furnace. Then all the studied samples were cut into small pieces and polished for property characterizations.

2.1.2. MELTING TEMPERATURE-BASED OXYFLUORIDE GLASSES AND GLASS-CERAMICS

Melting temperature-based samples with the molar composition of $45\text{SiO}_2\text{-}15\text{Al}_2\text{O}_3\text{-}12\text{Na}_2\text{O-}21\text{BaF}_2\text{-}7\text{LaF}_3\text{-}0.5\text{ErF}_3\text{-}1.0\text{YbF}_3$ were also prepared by a melt-quenching method. 10 g of the powdered mixture was melted in an electric furnace in air at $1450, 1500, 1550$, and $1590\text{ }^\circ\text{C}$, respectively, and kept for 45 min. Then each melt was quickly cast onto a heating plate at around $300\text{ }^\circ\text{C}$. Afterwards, each as-cast glass was annealed at $500\text{ }^\circ\text{C}$ for 8 hours and slowly cooled down to room temperature inside the furnace. Then all the studied samples were cut into small pieces and polished for property characterizations.

2.2. CHARACTERIZATION METHODS

The author performed most of the experiments and analyzed all results in this thesis. A co-author contribution is presented in the relevant sections if the experiments or characterizations were not conducted by the author independently.

2.2.1. X-RAY DIFFRACTION (XRD)

XRD patterns were obtained by using PANalytical X-ray diffraction meters in Aalborg University with Cu K α ($\lambda = 1.5406 \text{ \AA}$) radiation during the range of $10 < 2\theta < 90^\circ$ with a step size of 0.013° . All samples were finely grinded before measurement. Standard Powder Diffraction File (PDF) cards of the corresponding crystal structures were obtained from the software Jade 6.5.

2.2.2. DIFFERENTIAL SCANNING CALORIMETRY (DSC)

DSC measurements were performed on a Simultaneous Thermal analyser (STA) 449 F1 Jupiter (Netzsch, Germany) in Aalborg University. Pt/Rh crucibles were used for both samples and the references. The sample mass was normally about 30 mg. The direction of the enthalpy release, i.e., exothermic direction, points downwards in all figures in this thesis. All samples were scanned at $10^\circ\text{C}/\text{min}$ and heated from around 30°C to target temperature (900 or 1000°C) under Argon ambiance. Baselines were collected within the same temperature range and under same temperature rates before each test.

2.2.3. RAMAN SPECTROSCOPY

Raman spectra were obtained from a Micro-Raman spectrometer (inVia, Renishaw) within the range from 200 to 2000 cm^{-1} . All samples were excited by a 532 nm green laser and a typical power of 0.1 W was used to record the Raman shift. All samples were tested two times for error reduction.

2.2.4. ULTRAVIOLET-VISIBLE (UV-VIS) ABSORPTION SPECTROSCOPY

UV-VIS absorption spectra within $200\text{-}1000 \text{ nm}$ were collected from a UV-VIS spectrophotometer (Varian Cary 50) at Aalborg University. Baselines were collected from ambiance for each test. The real spectra were obtained by subtracting the baseline from each original one.

2.2.5. MOLECULAR DYNAMICS (MD) SIMULATIONS

Glass microstructures of the most samples were simulated by our collaborator Jincheng Du from University of North Texas, US. The DL POLY 2.20 package with a set of partial charge pairwise potentials with the form of Buckingham was used in investigating the structures and phase separation of several oxyfluoride glass systems (29). La^{3+} ions were used for representing Er^{3+} and Yb^{3+} ions in the glass composition. All the atoms were contained in the simulation bulk. The input density was theoretically calculated, and the method was described in the previous publications (29). Further details of MD simulations of oxyfluoride glasses can be found in their recent papers (30)(31)(32).

2.2.6. SCANNING ELECTRON MICROSCOPY (SEM)

Field-emission SEM images were acquired from a QUANTA 200 SEM, Zeiss EVO 60 SEM and a Zeiss Gemini SEM 500 with both secondary electron imaging and backscattered electron imaging modes in Alborg University, Qilu University of Technology and Kunming university to investigate the morphology of samples. Before the SEM measurements, most samples were etched in 7% HF solution for 20-25 s. Then all the samples were vacuum dried at 120 °C and then pasted onto the conductive gel before testing.

2.2.7. TRANSMISSION ELECTRON MICROSCOPY (TEM)

TEM photos of some samples were collected from a special aberration-corrected transmission electron microscope (ACTEM, FEI Titan Cubed Themis G2 300) worked at the voltage of 200 KV. In addition, this TEM is equipped with energy-dispersive X-ray spectrometer (EDS), high-angle annular dark-field scanning TEM (HAADF-STEM) and the selected area electron diffraction (SAED). TEM measurements of bulk samples were conducted in Zhongke Kefu Technology Company, while powder samples were measured at Kunming University of Science and Technology. Powder samples were dispersed in ethanol and ultrasonicated for 30 min, and then drop cast to copper mesh before TEM measurements. Bulk samples were prepared via the ion-beam milling Technique.

2.2.8. SOLID-STATE NUCLEAR MAGNETIC RESONANCE (NMR)

Solid-state NMR measurement was conducted by our collaborator Jinjun Ren, who is from Shanghai Institute of Optics and Fine Mechanics, Chinese Academy of Sciences. All details of NMR measurements for ^{19}F and ^{27}Al can be found in Paper II. To probe the distribution of the RE ions in the studied samples, we conducted the ^{139}La NMR measurements. The static spectra of ^{139}La were obtained at 71.2 MHz via the wideband uniform-rate smooth truncation-Carr-Purcell-Meiboom-Gill (WURST-CPMG)

technique. Further details of NMR measurements for ^{139}La can be found in their papers (33)(34).

2.2.9. REFRACTIVE INDEX (n)

n was measured at various wavelengths by KALNEW Precision Refractometer KPR-2000 at 25 °C in Shanghai Institute of Optics and Fine Mechanics, Chinese Academy of Sciences. All the samples were cut into the shape that two adjacent edges are 90 degrees and polished for n measurements.

2.2.10. UP-CONVERSION LUMINESCENCE (UCL)

The UCL spectra were measured by using a HITACHI F-7000 fluorescence spectrophotometer, which was conducted at Kunming University of Science and Technology. The wavelength range is 500-700 nm and all samples were excited by 980 nm laser diode (LD) (excitation power was 0.5 W and the slit was 1 nm).

2.2.11. FLUORESCENCE DECAY LIFETIME

The lifetime measurements were carried out using the method described in Ref. (35) The UC photoluminescence decay curves of both P-GC and the P-GC sample heat-treated at 680 °C for 4 hours were recorded by FLSP-980 spectrophotometer (Edinburgh Instruments Ltd., Edinburgh, UK), and the excitation source was 980 nm laser with the frequency of 500Hz.

CHAPTER 3. OXYFLUORIDE GLASSES AND GLASS-CERAMICS WITH VARYING $\text{La}_2\text{O}_3/\text{LaF}_3$ RATIO

It is known that glass network modifiers, especially alkali earth metal oxide or fluorides such as Na_2O , BaF_2 , La_2O_3 and LaF_3 , can break bridging oxygen (BO) bonds in $[\text{SiO}_4]$ and $[\text{AlO}_4]$ tetrahedra and form non-bridging oxygen (NBO) bonds, thus lowering glass network connectivity and resulting in different microstructures. In addition, glass network modifiers also can induce the formation of amorphous phase separation, which could reduce the crystallization activation energy to form fluoride crystals. Therefore, we first investigate the impact of different chemical compositions on the glass structure of melt-quenching derived oxyfluoride glasses or GCs. The studied molar compositions are $45\text{SiO}_2\text{-}15\text{Al}_2\text{O}_3\text{-}12\text{Na}_2\text{O}\text{-}21\text{BaF}_2\text{-(}7\text{-}x\text{)La}_2\text{O}_3\text{-}x\text{LaF}_3\text{-}0.5\text{ErF}_3\text{-}1\text{YbF}_3$ ($x=0, 2, 4, 6$ and 7 , denominated as 0LaF, 2LaF, 4LaF, 6LaF and 7LaF, respectively). This Chapter is mainly based on Paper IV, in which all the detailed information about the preparation, characterization and optical performances of the melt-quenching derived oxyfluoride glasses or GCs could be found.

3.1. CHARACTERIZATION OF MELT-QUENCHING DERIVED OXYFLUORIDE GLASSES AND GLASS-CERAMICS

3.1.1. GLASS STRUCTURAL ANALYSES

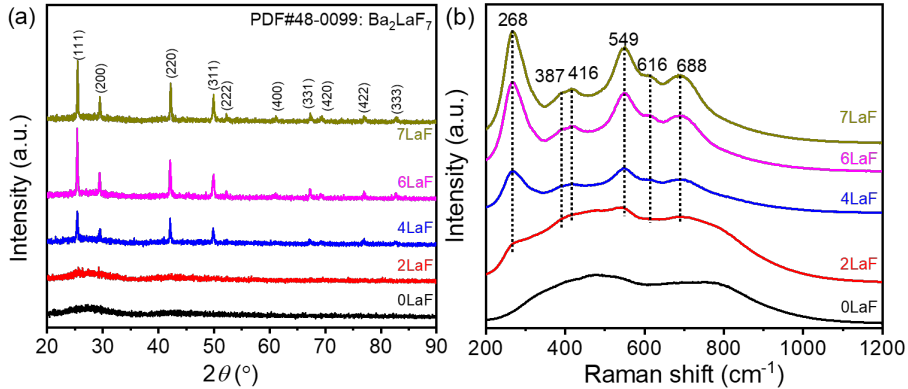


Figure 3-1 (a) XRD patterns and (b) Raman spectra of 0LaF, 2LaF, 4LaF, 6LaF and 7LaF samples, respectively. Figure adapted from Paper IV.

To obtain the structural information on medium-range order inside the studied samples, XRD analysis is conducted and the XRD patterns of 0LaF, 2LaF, 4LaF, 6LaF and 7LaF samples are shown in Figure 3-1a. For the XRD patterns of 0LaF and 2LaF samples, no distinct diffraction peak appears instead of two weak and broad humps, which belongs to the characteristic diffraction peak of oxyfluoride glasses reported in the previous study (36). This means both 0LaF and 2LaF samples are melt-quenching oxyfluoride glasses. With increasing LaF_3 content from around 4% to 7%, ten obvious diffraction peaks located at 25.5, 29.5, 42.2, 49.9, 52.3, 61.1, 67.3, 69.4, 77, and 82.7° are observed in the XRD patterns. In addition, both the peak positions and relative intensities match well with the standard face-centered cubic (FCC) Ba_2LaF_7 crystal (Powder Diffraction File (PDF)#48-0099) (25)(36), which indicates that Ba_2LaF_7 crystals take place during the quenching process. Thus, it is confirmed that melt-quenching derived oxyfluoride GCs form with increasing the content of LaF_3 by the XRD results. Noting that, owing to the substitution of the smaller sized Er^{3+} and Yb^{3+} ions for larger La^{3+} ions via entering Ba_2LaF_7 crystals, it leads to the shrinkage of the Ba_2LaF_7 unit cell (36) and the peak position slightly shifts to the larger angle compared with the standard PDF card of Ba_2LaF_7 crystal. Furthermore, it is seen from the full width at half maximum (FWHM) of XRD peaks that the average size of Ba_2LaF_7 crystals in studied samples increases with increasing the content of LaF_3 , which also can be calculated by the Debye-Scherrer equation (37)(38).

Figure 3-1b shows the Raman spectra of the studied samples. It is found that the Raman spectrum of 0LaF sample shows two broad Raman bands, which are attributed to oxyfluoride glasses (39). For other studied samples, the Raman peak at 268 cm^{-1} occurs in their Raman spectra, whose peak intensities increase with increasing the content of LaF_3 . This also verifies that Ba_2LaF_7 crystals are formed during melt-quenching and the fraction of Ba_2LaF_7 crystals increases with increasing the content of LaF_3 from 2% to 7% (36). The remaining Raman peaks at 387, 416, 549 cm^{-1} , 616 and 688 cm^{-1} are attributed to the Si-O-Si (Al) symmetrical stretching vibrations connecting inter-tetrahedral, respectively (40). Thus, the microstructural information of the Raman spectra agrees well with that of the XRD patterns, which indicates that melt-quenching derived GCs containing Ba_2LaF_7 crystals can be formed via increasing the content of LaF_3 .

3.1.2. LOCAL STRUCTURAL ANALYSIS

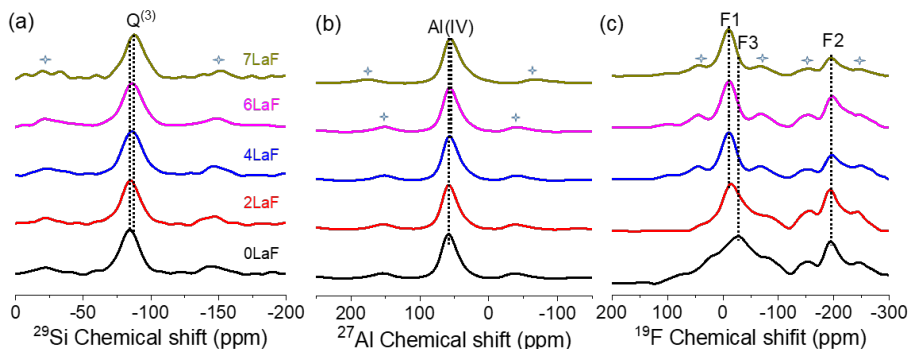


Figure 3-2 Structure characterizations by MAS NMR. ^{29}Si (a), ^{27}Al (b), and ^{19}F (c) spectra of 0LaF, 2LaF, 4LaF, 6LaF and 7LaF samples, respectively. \star : spinning sidebands. Figure adapted from Paper IV.

^{29}Si MAS NMR spectra for the studied samples are shown in Figure 3-2a. It is noticed that the resonance band shifts from -84 to -88 ppm with the samples obtained by the replacement of LaF_3 to La_2O_3 . This means that the coordination of Si^{4+} does not undergo an obvious change and this shifted band can be also ascribed to $\text{Q}^{(3)}$ species (41), where $^{(3)}$ donates the sum of the numbers of Si-O-Si (Al) linkages per unit. However, it is hard to distinguish the $\text{Q}^{(3)}$ units from the Si-O-Si or from Si-O-Al linkages. With increasing the content of LaF_3 , La^{3+} and F^- play the role of network modifiers, which further lowers glass network connectivity, thereby facilitating phase separation.

As shown in Figure 3-2b, ^{27}Al MAS NMR spectrum of 0LaF sample features the main resonance at about 58 ppm, which is attributed to four-coordinated aluminum (Al(IV)). With increasing the content of LaF_3 , the Al(IV) main resonance peaks shifted a little from 58 to 55 ppm, which suggests that the coordination number of Al has no significant change. It is reported that Al^{3+} ions primarily exist in $[\text{AlO}_4]$ tetrahedra besides a minor amount of $[\text{Al}(\text{O},\text{F})_4]$ in this system (29). However, owing to the field strength difference between Al^{3+} and La^{3+} ions and the increase of the fraction of Ba_2LaF_7 crystals, some Al-O linkages in the interface regions could be replaced by the Al-F linkages when increasing the content of LaF_3 . This means that the coordination environment of Al could be altered.

Figure 3-2c demonstrates the ^{19}F MAS NMR spectra of the studied samples. All the spectra exhibit two main broad signals at around -12 and -194 ppm, which are denoted as F1 and F2, respectively (32). In addition, a much broader resonance signal F3 with a smaller amplitude is observed at around -27 ppm in 0LaF sample, which gradually shifts to the position of F1 resonance with increasing the content of LaF_3 owing to the formation of Ba_2LaF_7 crystals. Thus, this resonance of F3 signal can be attributed to

F with different local environments in Ba_2LaF_7 clusters (42). This large width of this resonance suggests that Ba_2LaF_7 clusters have already presented in the oxyfluoride glass though still with a high degree of disorder (43). The resonance F1 is assigned to the F in La-F-Ba linkage of Ba_2LaF_7 crystals (29). F2 signals are related to F species involved in the F-Al linkages of Ba-F-Al or Na-F-Al (44).

3.1.3. THERMODYNAMIC ANALYSIS

Figure 3-3 shows the DSC output curves of the 0LaF, 2LaF, 4LaF, 6LaF and 7LaF samples, respectively, which are as a function of temperature. The onset temperatures of T_g , T_{c1} , T_{c2} , T_c , T_{m1} and T_{m2} are determined by the method described elsewhere (45) for each DSC curve and their values are shown in Table 3-1, respectively. It is seen that both T_g and T_{c1} values vary with increasing the content of LaF_3 , which means the glass network connectivity changes with the concentration of LaF_3 since the glass structure determines T_g and T_{c1} (46). In addition, the area of the first crystallization peak gradually increases and that of the second one slowly disappears with the increase of LaF_3 , implying that crystallization ability in the first crystallization regions increased with increasing the content of LaF_3 . The values of T_c , T_{m1} and T_{m2} also exhibit variation in the DSC curves of the studied samples.

Table 3-1 The onset temperatures of T_g , T_{c1} , T_{c2} , T_c and T_{m1} and T_{m2} of the 0LaF, 2LaF, 4LaF, 6LaF and 7LaF samples, respectively. Table adapted from Paper IV.

<i>Sample</i>	T_g	T_{c1}	T_{c2}	T_c	T_{m1}	T_{m2}
0LaF	561	631	692	807	936	958
2LaF	555	614	699	826	947	991
4LaF	583	624	~	820	938	963
6LaF	587	618	~	792	866	961
7LaF	561	605	~	790	871	982

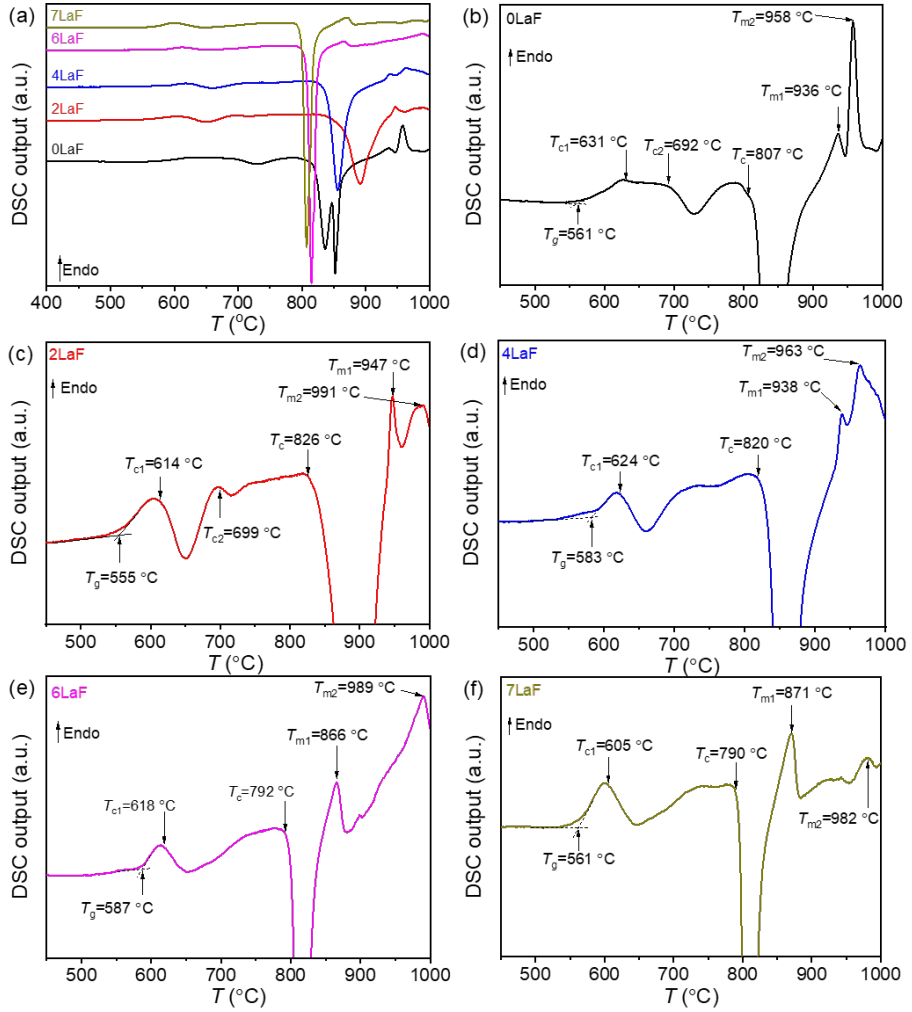


Figure 3-3 (a) Overall DSC curves of all the samples. Each enlarged DSC curve of : (b) 0LaF, (c) 2LaF, (d) 4LaF, (e) 6LaF and (f) 7LaF samples, respectively. The onset temperatures of T_g , T_{c1} , T_{c2} , T_c , T_{m1} and T_{m2} are marked in each figure. Figure adapted from Paper IV.

3.1.4. MD SIMULATION ANALYSIS

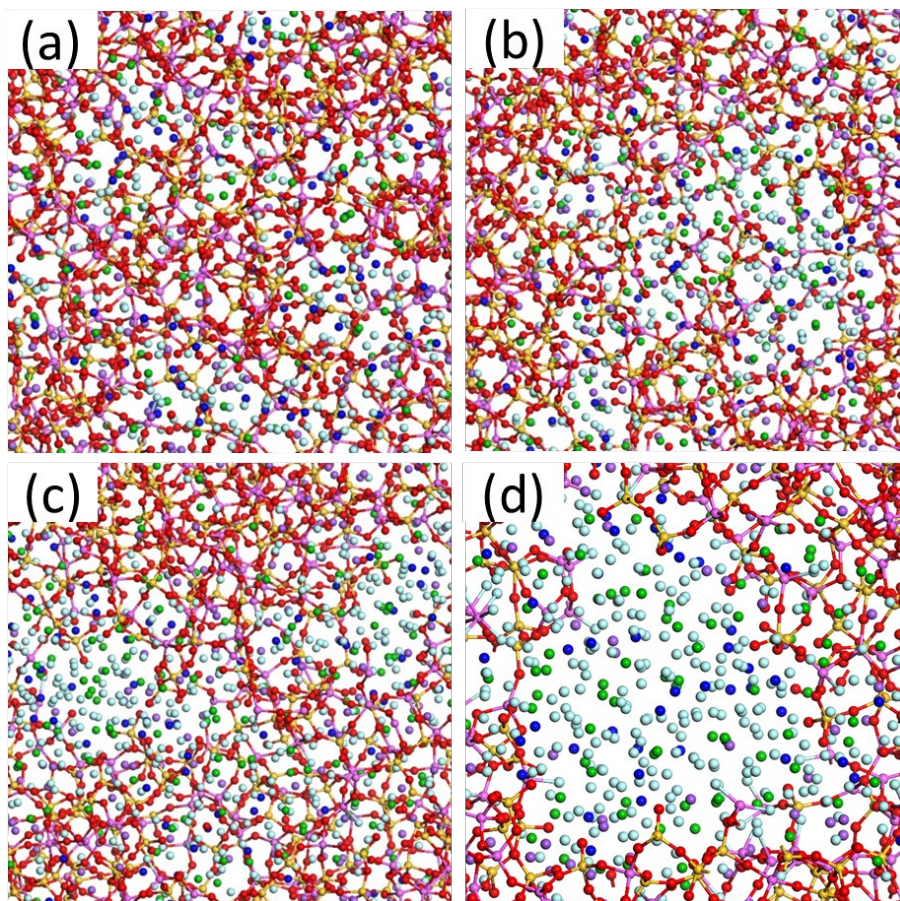


Figure 3-4 MD simulated glass structure of 0LaF (a), 2LaF (b), 4LaF (c) and 7LaF (d) samples composed of network forming SiO_4 and AlO_4 tetrahedra and network modifiers. Note that Er^{3+} and Yb^{3+} are replaced by La^{3+} to perform MD simulations. Figure adapted from Paper IV.

To understand the structure of the studied samples at the atomic level, MD simulations have been extensively applied in studying oxyfluoride glasses (47)(48). Thus, MD simulation is conducted to reveal the studied glass structural features. As shown in Figure 3-4, the simulated glass structure shows the regions of aluminosilicate oxide-rich and fluoride-rich phases, and this is an obvious sign of phase separation (49). Additionally, the fluoride-rich phase domains increase with the content of LaF_3 . It is also seen that the chemical composition of the fluoride-rich region is similar to that of Ba_2LaF_7 crystals. This might mean that the high tendency of phase separation leads to the occurrence of spontaneous crystallization. It is seen that the aluminosilicate oxide-rich phase is composed of a network structure with $[\text{SiO}_4]$ and $[\text{AlO}_4]$ tetrahedral units.

In comparison, most of the network modifier cations such as Ba^{2+} and La^{3+} ions enrich in the fluoride-rich phase, which can be interpreted by Poulain's ionic glass model (50). However, Al^{3+} and Na^+ ions are preferentially distributed at the interface between aluminosilicate oxide-rich and fluoride-rich phases. In addition, these cations not only act as network modifiers in the aluminosilicate oxide-rich phase but also connect with non-bridging $\text{O}_{1/2}^-$ and ionic F^- of the fluoride-rich phase. For the coordination number in the aluminosilicate-rich phase, Si^{4+} ions keep the coordination number being 4 with LaF_3 substituting for La_2O_3 (Figure 3-5), while the coordination number of Al^{3+} decreases from 4 to 3.6. These results indicate that the local structure of $[\text{SiO}_4]$ network remains unchanged and a small amount of the $[\text{AlO}_4]$ species transit into $[\text{Al}(\text{O},\text{F})_4]$ tetrahedra at the interphase regions with increasing the content of LaF_3 . For the fluoride-rich phase, Ba-F and La-F coordination numbers sharply increase with the content of LaF_3 , whereas coordination numbers of Na-F slightly increase. This means that preferential coordination of both Ba^{2+} and La^{3+} in the fluoride-rich phase and Na^+ in the interphase agrees well with the experimental studies that F^- ions prefer to bond with Ba^{2+} and La^{3+} ions rather than with Na^+ ions (51).

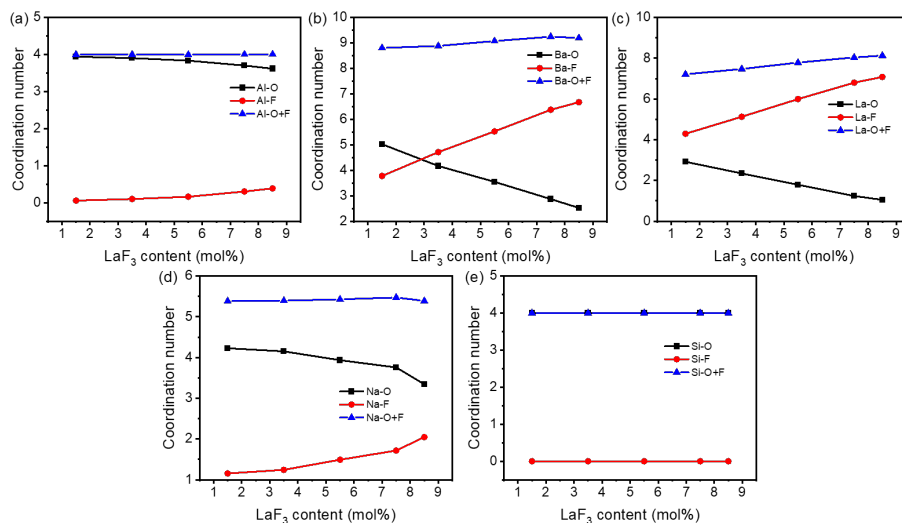


Figure 3-5 Coordination number variation of Al^{3+} (a), Ba^{2+} (b), La^{3+} (c) Na^+ (d) and Si^{4+} (e) with increasing LaF_3 content. Figure adapted from Paper IV.

3.1.5. MORPHOLOGY OF GLASSES AND GLASS-CERAMICS

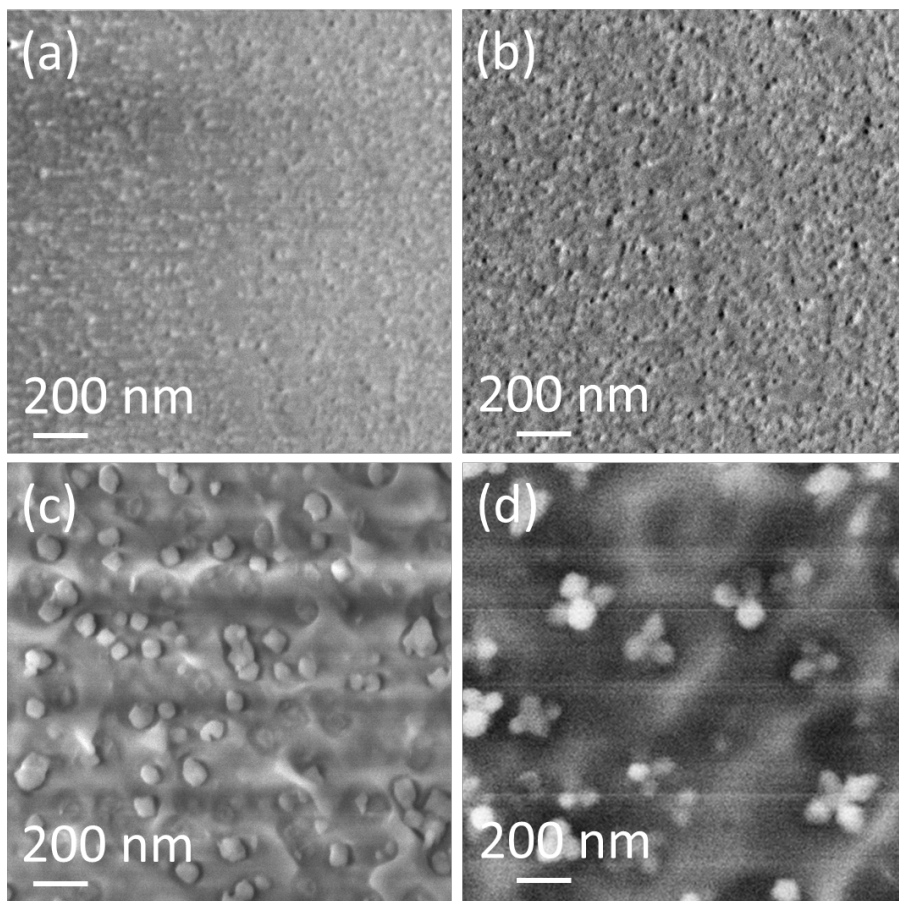


Figure 3-6 SEM images of 0LaF (a), 2LaF (b), 4LaF (c) and 7LaF (d) samples, respectively. Figure adapted from Paper IV.

To further observe the phase separation in the oxyfluoride glasses, we perform SEM measurements for the studied samples etched in 7% HF solution for 20-25 s. It is seen that two distinct regions of both white droplet and black domains are shown in the SEM images of the 0LaF sample (Figure 3-6a), which correspond to fluoride-rich and aluminosilicate oxide-rich phases of glass matrix, respectively (10). Usually, the aluminosilicate oxide-rich phases containing $[\text{SiO}_4]$ and $[\text{AlO}_4]$ tetrahedral are attacked stronger by HF acid than the fluoride-rich phases (52). The etched reactions are expressed by the following equations:



Thus, the fluoride-rich phases become visible in glass matrix and are shown by white droplet domains. It is reported that La₂O₃ can be regarded as the network intermediate (53) in the oxyfluoride glasses, the role of which is similar to that of Al₂O₃. Therefore, a few La³⁺ ions might enter the aluminosilicate oxide-rich network, forming [Si(La)O₄] tetrahedral units. On the contrary, LaF₃ can disaggregate the glass network. Thus, both area and shape of the fluoride-rich phase vary with increasing the content of LaF₃ and even two types of white domains in both flower-like and interpenetrating shapes occur in 4LaF (c) and 7LaF (d) samples. To further distinguish between the two types of white domains, SEM measurements (backscattered electron mode) are conducted for 0LaF, 4LaF and 7LaF samples without etching by HF acid. The corresponding images are shown in Figure 3-7. It is seen that only some flower-like shaped domains are observed in the glass matrix, their size increases with the increasing content of LaF₃. Thus, this domain can be attributed to Ba₂LaF₇ crystals. Another one is assigned to the interpenetrating fluoride-rich phase.

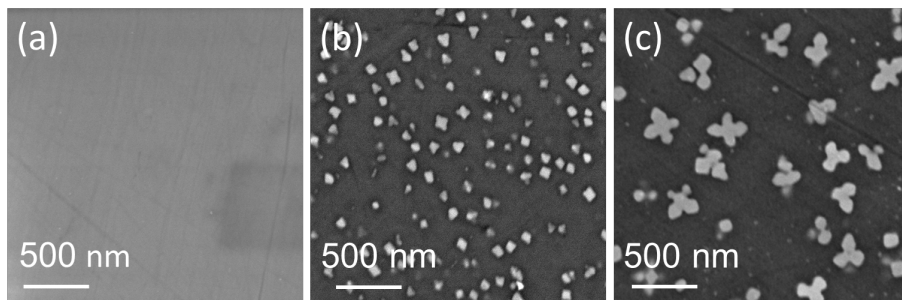


Figure 3-7 SEM images obtained from backscattered electron mode of 0LaF (a), 4LaF (b) and 7LaF (c) samples without etching by HF acid, respectively. Figure adapted from Paper IV.

3.2. OPTICAL PROPERTIES MELT-QUENCHING DERIVED OXYFLUORIDE GLASSES AND GLASS-CERAMICS

3.2.1. ABSORPTION AND TRANSMITTANCE SPECTRA

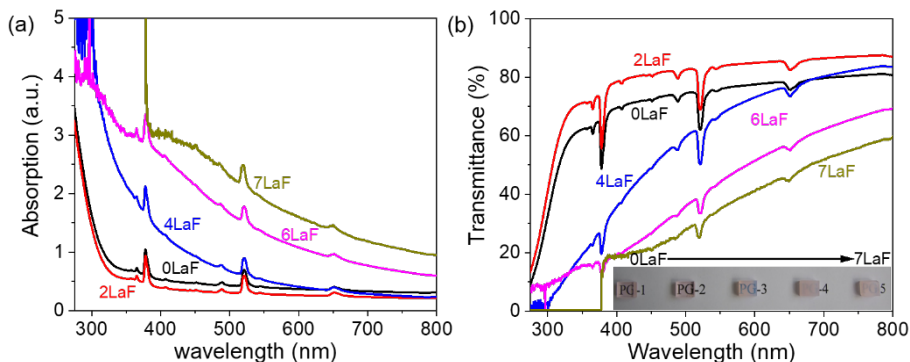


Figure 3-8 Absorption spectra (a) and light transmittance spectra (b) with insert photo images (from left to right) of 0LaF, 2LaF, 4LaF, 6LaF and 7LaF samples, respectively. Figure adapted from Paper IV.

Figure 3-8a shows the absorption spectra of the studied samples. Five main absorption peaks at about 362, 376, 486, 521, and 651 nm, respectively, are observed in all the spectra, which correspond to the transitions from the ground state $^4I_{15/2}$ to the excited states: $^2G_{7/2}$, $^4G_{11/2}$, $^2H_{9/2}$, $^2H_{11/2}$, and $^4F_{9/2}$ of Er^{3+} ions, respectively (24). It is seen that the absorption intensities first decrease then increase with the increasing content of LaF_3 . To investigate the variation of optical transmittance in the studied samples, the light transmittance for 1 mm in thickness is obtained from the above absorption spectra by using the below equation (24):

$$T = 10^{(2 - \frac{I}{THK})} \quad (3-3)$$

Where T is optical transmittance (%), I is the absorption intensity, THK is the sample thickness (mm).

The corresponding transmittance spectra are shown in Figure 3-8b, their values first increase then decrease with the increasing content of LaF_3 . This trend can also be reflected by the inserted optical images of the studied samples (from left to right, respectively). The decrease in the optical transmittance can be clarified as follows. First, the size of the Ba_2LaF_7 crystals increases with the increasing content of LaF_3 , which is gradually close to the wavelength of the incident light, resulting in strong light scattering. Second, the area of the fluoride-rich phase increases with increasing the concentration of LaF_3 . The refractive index (n) differences between fluoride-rich

and aluminosilicate oxide-rich phases also increase with the increasing LaF_3 , causing an increase in light scattering (54).

3.2.2. UCL AND FLUORESCENCE DECAY LIFETIME

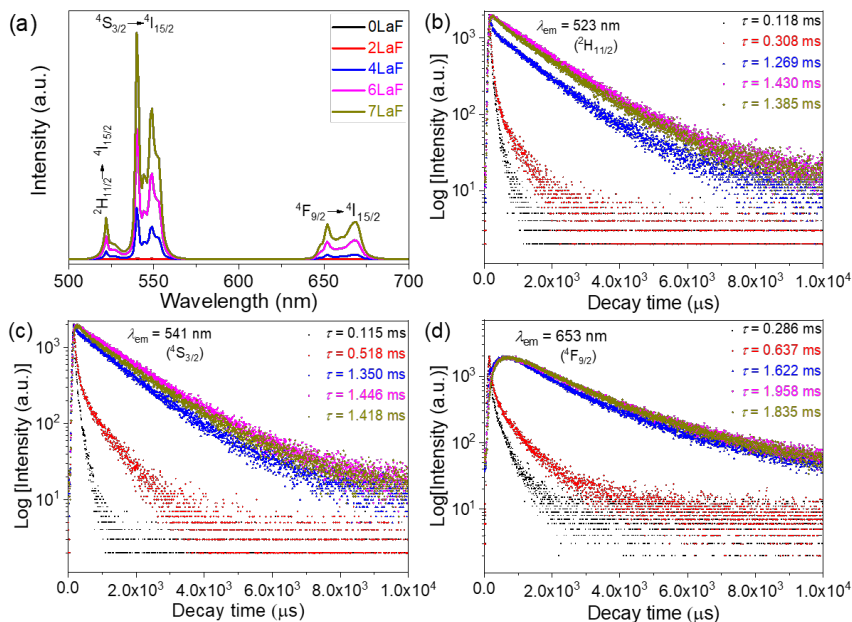


Figure 3-9 UCL spectra (a) and decay lifetime of Er^{3+} in $^2\text{H}_{11/2}$ (b), $^4\text{S}_{3/2}$ (c) and $^4\text{F}_{9/2}$ (d) states of 0LaF, 2LaF, 4LaF, 6LaF and 7LaF samples, respectively. Figure adapted from Paper IV.

As shown in Figure 3-9a, compared with 0LaF sample, other samples exhibit much stronger UCL and the intensities of which gradually increase with the high LaF_3 content samples. Note that the UCL arises from the transitions $^2\text{H}_{11/2} \rightarrow ^4\text{I}_{15/2}$ (523 nm), $^4\text{S}_{3/2} \rightarrow ^4\text{I}_{15/2}$ (541 nm), and $^4\text{F}_{9/2} \rightarrow ^4\text{I}_{15/2}$ (653 nm) of Er^{3+} ions (55). It is seen that the UCL of 7LaF sample is about 2700 times higher than that of 0LaF sample. This enhancement can be explained by the following two aspects. First, for 0LaF sample, Er^{3+} and Yb^{3+} ions are present in glass matrix rather than Ba_2LaF_7 crystals. Since glass matrix possesses higher phonon energy ($1200\text{--}1300\text{ cm}^{-1}$) than the crystals (270 cm^{-1}), the non-radiative relaxation rate of Er^{3+} and Yb^{3+} in the former is higher than that in the latter (36). Hence, the UCL of 0LaF sample is weaker than that of the samples doped with LaF_3 . Second, as the fraction of Ba_2LaF_7 crystals increases with increasing the content of LaF_3 , some Er^{3+} and Yb^{3+} ions can exist in Ba_2LaF_7 crystals and their distance in Ba_2LaF_7 crystals becomes short, both of which increase the energy transfer possibility from Yb^{3+} and Er^{3+} ions, and thus enhancing the UCL. The energy level scheme of Er^{3+} and Yb^{3+} ions in the studied samples are described in Paper I, which indicates the UCL mechanism (56). To further demonstrate the energy transfer from Yb^{3+} to Er^{3+} ions, the UCL decay curves of the studied samples for $^2\text{H}_{11/2}$

$\rightarrow {}^4I_{15/2}$ (523 nm), ${}^4S_{3/2} \rightarrow {}^4I_{15/2}$ (541 nm), and ${}^4F_{9/2} \rightarrow {}^4I_{15/2}$ (653 nm) transitions of Er^{3+} ions are shown in Figure 3-9b-d. The corresponding decay curves can be well fitted by the second-order exponential decay mode as the equation below (57).

$$I = A_1 e^{(-t/\tau_1)} + A_2 e^{(-t/\tau_2)} \quad (3-5)$$

Where I is the UCL intensity, A_1 and A_2 are the fitting parameters, t is the time, τ_1 and τ_2 are the slow and fast decay components (long and short lifetime), respectively. Using these above parameters, the average lifetime τ can be calculated by the following equation:

$$\tau = (A_1 \tau_1^2 + A_2 \tau_2^2) / (A_1 \tau_1 + A_2 \tau_2) \quad (3-6)$$

The values (see Figure 3-9b-d) of the average lifetime for ${}^2H_{11/2}$, ${}^4S_{3/2}$, and ${}^4F_{9/2}$ states increase with increasing the content of LaF_3 , respectively. These results imply that the samples with higher concentrations of LaF_3 exhibit higher probabilities of energy transfer between Er^{3+} and Yb^{3+} ions.

3.3. SUMMARY

In this Chapter, the preparations and characterizations of composition-dependent oxyfluoride glasses are presented, detailed information could be found in Paper IV. We investigate the impact of different chemical compositions on the glass structure of melt-quenching derived oxyfluoride glasses or GCs. The experimental results show that fluoride-rich domains increase with the content of LaF_3 , which agrees well with the results of MD simulations, leading to the decrease of crystallization activation energy for precipitating fluoride crystals. Interestingly, Ba_2LaF_7 crystals take place from the glass matrix during the quenching process by replacing La_2O_3 with LaF_3 in the composition. Additionally, the transmittance of the studied samples decreases with increasing the fraction and the size of crystals, which results from the strong light scattering. However, the intensities of UCL gradually enhance with the variation of compositions. This can be attributed to the increasing probabilities of energy transfer between Er^{3+} and Yb^{3+} ions. In summary, this composition-dependent strategy can provide us with a new perspective to enhance the UCL, though this strategy leads to a decrease in optical transmittance. Thus, these derived composition-dependent GCs are novel materials for enhancing optical properties.

CHAPTER 4. IMPACT OF HEAT TREATMENT ON PROPERTIES OF OXYFLUORIDE GLASS-CERAMICS

Based on Chapter 3, we have found that glass structure, phase separation, crystallization behavior and optical properties vary with modifying the ratio between La_2O_3 and LaF_3 in the chemical compositions. In this Chapter (see Paper II), we mainly studied the impact of HT on 7LaF samples to further understand the structural evolution and to investigate the origin of the transformation from translucent to transparent. All the detailed information about the characterization and optical performances of these samples is also conducted. To investigate the effect of HT on both the T_g and T_{C1} of 7LaF sample, 7LaF samples are heat-treated at 600, 640 and 680 °C for 4 hours, respectively.

4.1. OPTICAL, THERMAL AND MICROSTRUCTURAL ANALYSES

4.1.1. OPTICAL TRANSPARENCY ANALYSIS

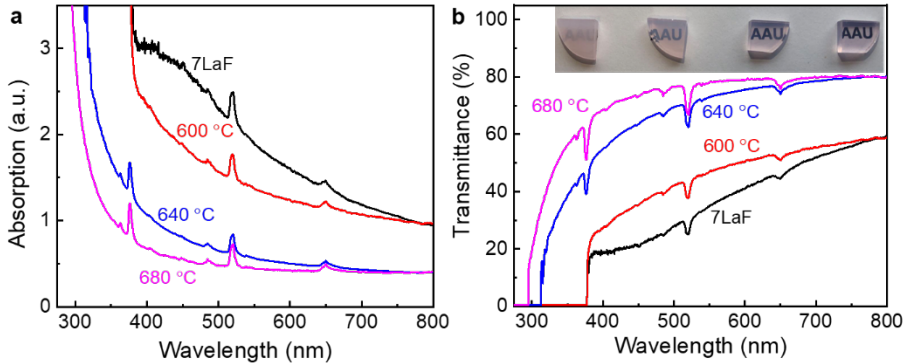


Figure 4-1 (a) Absorption spectra of 7LaF samples before and after HT at 600, 640, and 680 °C for 4 hours. (b) Transmittance spectra of the above-mentioned samples. Inset: Photo images of 7LaF sample and three 7LaF samples heat-treated at 600, 640, and 680 °C for 4 hours, respectively (from left to right). Figure adapted from Paper II.

The absorption spectra (Figure 4-1a) of the studied samples contain five main absorption peaks at about 362, 376, 486, 521, and 651 nm, respectively. These absorption peaks correspond to the transitions from the ground state $^4\text{I}_{15/2}$ to the excited states: $^2\text{G}_{7/2}$, $^4\text{G}_{11/2}$, $^2\text{H}_{9/2}$, $^2\text{H}_{11/2}$, and $^4\text{F}_{9/2}$ of Er^{3+} ions, respectively (see Chapter 3). Strikingly, the absorption intensities for the three heat-treated samples decrease with increasing the HT temperature, and this tendency is opposite to that for traditional

GCs (27)(36)(46)(58). Figure 4-1b shows the transmittance spectra converted from the absorption spectra (equation see Chapter 3), revealing that their transmittance increases from 59% to 80% (for the thickness of 1 mm) upon the increasing HT temperature. The corresponding inset shows the optical images of 7LaF and three 7LaF samples heat-treated at 600, 640, and 680 °C (from left to right, respectively) for 4 hours, where it is seen that the transmittance increases with HT temperature. This trend can be clarified as follows. First, the size of the Ba_2LaF_7 crystals might decrease with the increasing HT temperature, leading to a reduction of light scattering. Second, if they are large-sized crystals (e.g., up to micrometer scale), HT might change the chemical composition of glass matrix and then adjust the n of glass matrix to match that of Ba_2LaF_7 crystals. Thus, light scattering can be attenuated and exhibit high transmittance (54).

4.1.2. THERMODYNAMIC ANALYSIS

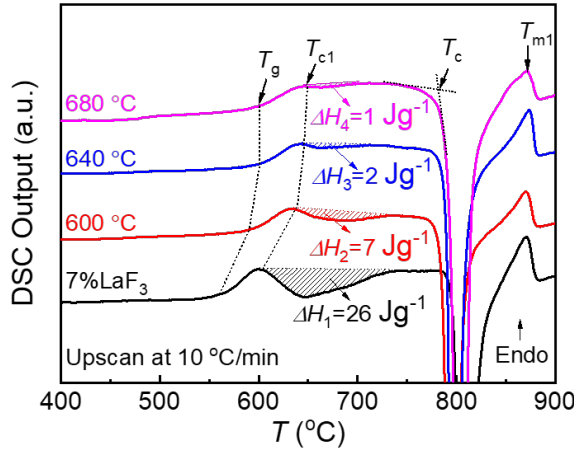


Figure 4-2 DSC output of 7LaF sample and three 7LaF samples heat-treated at 600, 640 and 680 °C, respectively, for 4 hours. T_g , T_{c1} , T_c and T_{m1} are marked in the Figure. The area of the first exothermic peak (i.e., the hatched area) represents ΔH determined by the extent of the crystal formation in each sample. Figure adapted from Paper II.

The DSC curves of the studied samples show that T_g and T_{c1} first increase and then gradually remain unchanged with increasing HT temperature. However, the values T_c decrease from 792 to 782 °C upon HT at 600 °C for 4 hours, and then remain stable with further increasing HT temperature, while the T_m values remain constant with increasing HT temperature (Figure 4-2). To further show the dynamic change of these characteristic temperatures, we also conduct HT at the duration of 1 and 2 hours for each HT temperature. The values of T_g and T_{c1} are shown in Table 4-1, which increase with the increasing HT temperature and duration. Moreover, the varied trend of their values in the heat-treated samples for 1 and 2 hours is similar to that in the studied samples heat-treated for 4 hours. The maximum T_g and T_{c1} values indicate that the

crystallinity has reached maximum values at the sufficiently high extent of HT temperature and duration. In other words, the composition of the glass matrix phase cannot vary with further HT, i.e., the glass structure does not change since the glass structure determines T_g and T_{c1} (59). To study the first crystallization event of 7LaF sample and three 7LaF samples heat-treated at 600, 640 and 680 °C, respectively, for 4 hours, the crystallization enthalpy (ΔH) of each sample was calculated by integrating the exothermic peak (Figure 4-2). It is evident that ΔH values gradually decrease with increasing HT temperature, implying that the crystallization already takes place during HT. This means that 7LaF sample has a strong tendency to crystallize before the main crystallization occurs around 800 °C (60).

Table 4-1 The onset temperatures of T_g and T_{c1} of both 7LaF and 7LaF samples subjected to HT at 600, 640, and 680 °C for 1, 2 and 4 hours, respectively. Table adapted from Paper II.

T_{HT} (hours)		1		2		4	
		T_g	T_{c1}	T_g	T_{c1}	T_g	T_{c1}
T_{HT} (°C)	7LaF	558	607	558	607	558	607
	600	582	630	591	635	594	638
	640	588	634	592	637	602	647
	680	587	638	594	640	601	651

4.1.3. MICROSTRUCTURAL ANALYSIS

Figure 4-3a illustrates the XRD patterns of the studied samples. The diffraction peaks of 7LaF sample are identified to be the FCC Ba_2LaF_7 crystal (See Chapter 3). It is seen that the diffraction peaks become more intense and no new diffraction peak appears upon HT, which means that the crystal is pure Ba_2LaF_7 crystals. Additionally, the purity of the cubic Ba_2LaF_7 crystals is also verified via performing XRD Rietveld refinement for 7LaF sample heat-treated at 640 °C for 4 hours (see Paper II). It is estimated that the crystallinity increases from around 42 to 65% with increasing HT temperature at 680 °C for 4 hours (Table 4-2), which is obtained by calculating the area ratio between all the crystalline peaks and all the crystalline and amorphous peaks via the software of Jade. This implies that HT causes the formation of Ba_2LaF_7 crystals compared with the fraction of Ba_2LaF_7 crystals in 7LaF sample.

Figure 4-3b illustrates the Raman spectra of the studied samples, which are normalized by the intensity of the peak at 550 cm^{-1} on Raman curves. It is found that the sharp Raman peak at 269 cm^{-1} (low-frequency region) enhances with increasing HT temperature, which should be the combined vibration peaks of both Ba-F and La-F bonds in Ba_2LaF_7 crystals (36)(61). However, other Raman peaks of tetrahedral units at 386, 416, 550, 616 and 689 cm^{-1} , respectively, become weaker with the increasing HT temperature. This verifies that the crystallinity increases upon HT, which agrees with that of the DSC and XRD results. Specifically, for the Raman peaks of tetrahedral units, the mid-frequency bands at 350-700 cm^{-1} are associated with the Si-O-Si (Al) symmetric stretching vibration in the glass matrix (62)(63). The peak at 418 cm^{-1} is ascribed to the symmetric stretch of five-fold ring structure, while the peaks at 550, and 610 cm^{-1} are attributed to the symmetric stretch of three-fold ring structures, respectively (64).

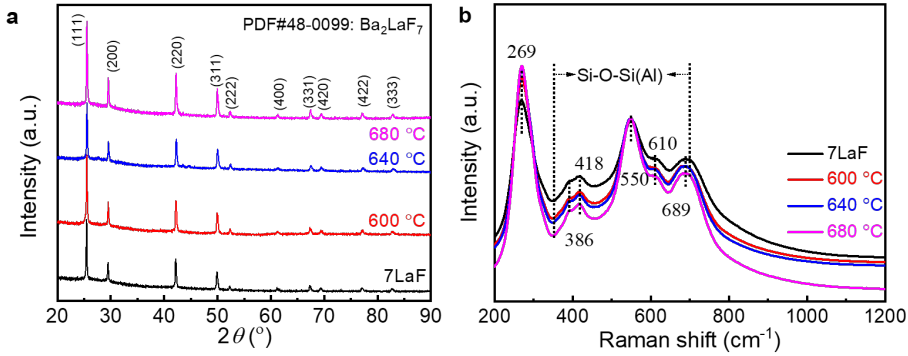


Figure 4-3 (a) XRD patterns and (b) Normalized Raman spectra of 7LaF sample and three 7LaF samples heat-treated at 600, 640 and 680 $^{\circ}\text{C}$, respectively, for 4 hours, where the vibrational modes and the peak positions are indicated. Figure adapted from Paper II.

Table 4-2 Crystallinity in both 7LaF and three 7LaF samples heat-treated at 600, 640, and 680 $^{\circ}\text{C}$ for 4 hours, respectively. Table adapted from Paper II.

	7LaF	600 $^{\circ}\text{C}$	640 $^{\circ}\text{C}$	680 $^{\circ}\text{C}$
Crystallinity	42%	44%	57%	64%

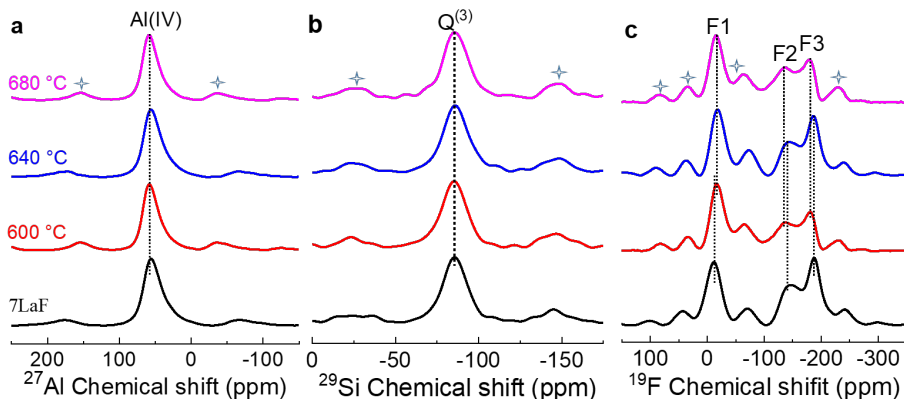


Figure 4-4 MAS NMR spectra of ^{27}Al (a), ^{29}Si (b) and ^{19}F (c) spectra of 7LaF sample and three 7LaF samples heat-treated at 600, 640 and 680 °C, respectively. \star : spinning sidebands. Figure adapted from Paper II.

To further reveal the local structural evolution during HT, we performed the ^{27}Al , ^{29}Si , and ^{19}F NMR measurements on the studied samples. The main resonance signal in all the ^{27}Al MAS NMR spectra (Figure 4-4a) is still located at about 60 ppm before and after HT, indicating that Al(IV) has no significant change upon HT. Note that Al^{3+} ions primarily exist in $[\text{AlO}_4]$ tetrahedra besides a minor amount of $[\text{Al}(\text{O},\text{F})_4]$. Some Al-F linkages in the interface regions could be replaced by the Al-O linkages upon HT owing to the increasing fraction of Ba_2LaF_7 crystals. This means that the coordination environment of Al(IV) could be altered slightly (see Chapter 3). For the MAS NMR spectra (Figure 4-4b) of ^{29}Si , the resonance band at about -86 ppm is ascribed to $\text{Q}^{(3)}$ species. Thus, the coordination of Si^{4+} does not undergo an obvious change after HT and remains as $\text{Q}^{(3)}$. All the ^{19}F MAS NMR spectra in Figure 4-4c exhibit two broad signals at around -12, and -188 ppm, which are denoted as F1 and F2, respectively. The broad signal of F1 is assigned to the F in La-F and Ba-F linkages, while the F2 signal belongs to the Al-F-Al and Na-F-Al linkages, respectively. Upon HT, owing to the increasing fraction of Ba_2LaF_7 crystals, the F1 resonance shifts from -12 to -18 ppm, indicating that some F^- ions participate in the Ba_2LaF_7 crystals rather than stay in the glass matrix.

4.1.4. STRUCTURAL ORIGIN AND EVOLUTION OF CRYSTALS

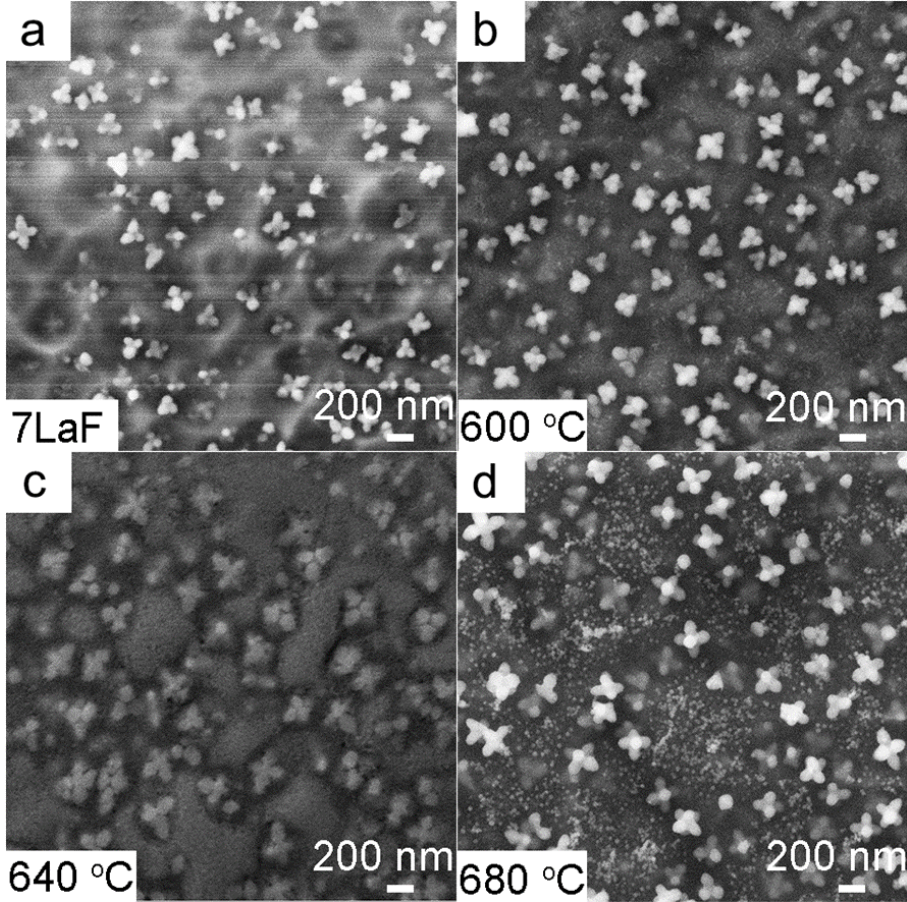


Figure 4-5 SEM images of 7LaF sample (a) and three 7LaF samples (b-d) heat-treated at 600, 640, 680 °C for 4 hours, respectively. Figure adapted from Paper II.

To reveal the impact of HT on the crystal evolution of the studied samples, we conduct SEM measurements. The corresponding SEM images are illustrated in Figure 4-5, respectively. We have clarified that the three distinct regions are in Chapter 3. For the SEM image (Figure 4-5a) of 7LaF sample, it is observed that the Flower-like Ba_2LaF_7 crystals (around 180~190 nm) are distributed in the fluoride-rich phases. Ba_2LaF_7 crystals grow to about 220 nm and the tiny spherical Ba_2LaF_7 nanocrystals (about 5 nm) precipitate from the fluoride-rich phase upon HT at 600 °C (Figure 4-5b). This implies that the formation of the fluoride-rich phase assists the growth of the existing crystals and the formation of Ba_2LaF_7 nanocrystals. Upon HT at 640 °C, both the flower-like crystals and the nanocrystals grow to about 260 nm and 15 nm, respectively (Figure 4-5c). At 680 °C, two types of Ba_2LaF_7 crystals further grow to

300 nm and 25 nm, respectively (Figure 4-5d). This implies the rise of both the crystallinity and the size of the flower-like Ba_2LaF_7 crystals with increasing HT temperature.

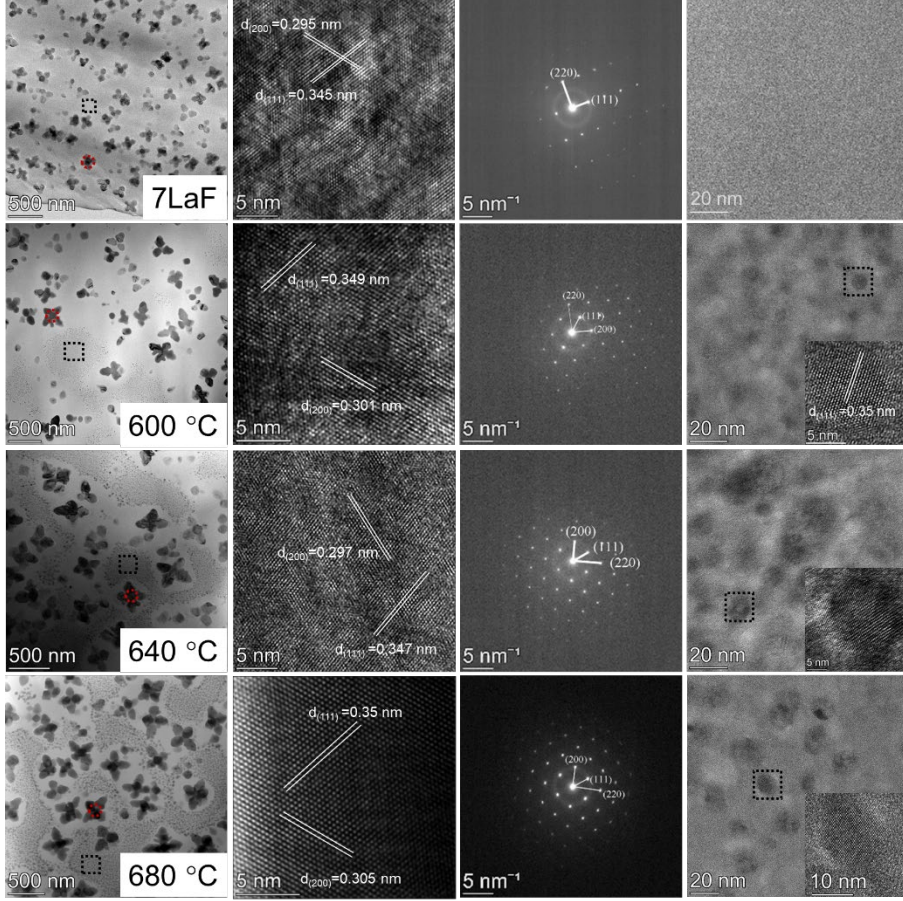


Figure 4-6 ACTEM images of 7LaF sample (the first row) and three 7LaF samples heat-treated at 600, 640, 680 °C for 4 hours, respectively (See the second, third and fourth row). The first column: Overview images; The second column: Lattice structure of the flower-like Ba_2LaF_7 crystals; The third column: Electron diffraction of the domains (see inset) selected from red dashed circles in their overview images. The fourth column: Formation of the tiny spherical crystals and their evolution with HT temperature (see the black dashed squares in the overview images). Insets: Lattice structure of the tiny spherical crystals selected from black dashed squares. Figure adapted from Paper II.

ACTEM and HRTEM micrographs for the studied samples are shown in Figure 4-6. For 7LaF sample, flower-like Ba_2LaF_7 crystals (about 190 nm) precipitate from the glass matrix. It is found that the crystal lattice fringes with the spacings 0.345 nm and 0.295 nm are shown in HRTEM image, which are indexed as the (111) and (220)

planes of Ba_2LaF_7 crystals, respectively. The SAED photograph reveals that Ba_2LaF_7 crystals are single-crystal. The HRTEM images exhibit the amorphous nature of the glass matrix phase. This means that only flower-like Ba_2LaF_7 single crystals exist in glass matrix of 7LaF sample.

Upon HT at 600 °C, 640 °C and 680 °C, it is seen from the overview images that two kinds of crystals are separately precipitated in the glass matrix. the flower-like Ba_2LaF_7 crystals grow to approximately 220, 260, 300 nm, respectively. Meanwhile, some spherical Ba_2LaF_7 crystals with sizes of around 6, 15 and 25 nm, respectively, uniformly precipitate and grow in some regions from glass matrix. These Ba_2LaF_7 crystals grow through the migration of Ba^{2+} , La^{3+} , and F^- ions to the nucleation sites. Thus, the composition of glass matrix (see the regions around the flower-like crystals) is changed by the depletion of Ba^{2+} and La^{3+} , and consequently, the network connectivity of the oxide glass matrix increases with the increasing HT. These results of crystals size agree with the above-mentioned SEM results. For the HRTEM images of the heat-treated samples, their crystal lattice spacings are determined, which match the corresponding planes of Ba_2LaF_7 crystals. It is inferred that Ba^{2+} and La^{3+} ions are arranged in an ordered manner, being a typical feature of a single crystal. This confirms that the flower-like Ba_2LaF_7 are indeed single crystals in the SAED pattern photograph. The inset lattice structure of spherical Ba_2LaF_7 crystals (fourth column) indicates that the spherical domains are still Ba_2LaF_7 single nanocrystals (see Paper II).

4.2. ORIGIN OF THE INCREASE OF TRANSMITTANCE

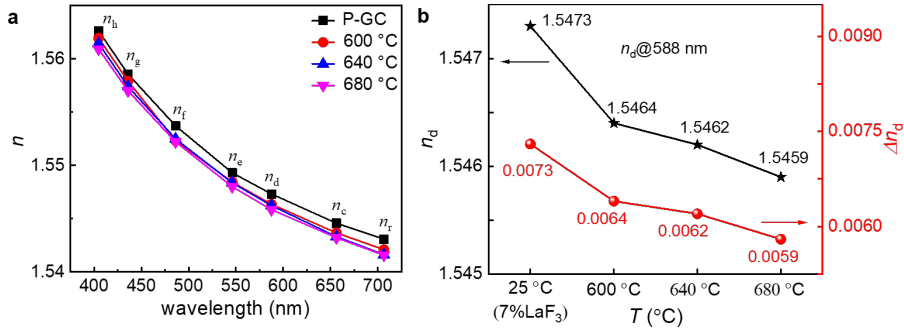


Figure 4-7 (a) n as a function of the light wavelength for 7LaF sample and three heat-treated samples. (b) n_d at the wavelength of 588 nm (black star symbols) and Δn_d between the studied samples and the Ba_2LaF_7 crystallites (red sphere symbols). The error range of n : ± 0.0001 . Figure adapted from Paper II.

To explore the origin of the increase of transmittance with increasing HT temperature, we measure n of the studied samples at different wavelengths. It is found that n values decrease with increasing HT temperature (Figure 4-7a and Table 4-3), indicating that the n values of the remaining glass matrix are lowered since that of Ba_2LaF_7 crystal is

constant. It is reported that n is proportional to the density of the studied samples (65)(66)(67), and hence the density exhibits the same variation trend with HT temperature as the n trend (Table 4-3). To compare the difference of n between the studied samples and the pure Ba_2LaF_7 crystals, n_d and Δn_d are shown in Figure 4-7b and decreases with increasing HT temperature (68). It is seen that the n_d of the heat-treated 7LaF sample gradually approaches that of Ba_2LaF_7 crystals ($\sim 1.54@588$ nm), and consequently, the light scattering is greatly suppressed (39)(69)(70). Hence, the heat-treated 7LaF sample at 680 °C for 4 hours displays the highest transmittance. This is opposite to the trend for traditional GCs, where Δn_d increases with increasing HT temperature.

Table 4-3 n and Density of the investigated 7LaF sample and three heat-treated samples. Table adapted from Paper II.

Sample name	7LaF	600 °C	640 °C	680 °C
n_h (404.66 nm)	1.56264	1.56196	1.56146	1.56093
n_g (435.84 nm)	1.55858	1.54792	1.55742	1.55701
n_f (486.13 nm)	1.55372	1.55233	1.55249	1.55222
n_e (546.07 nm)	1.54931	1.54844	1.54837	1.54801
n_d (587.56 nm)	1.54732	1.54636	1.54623	1.54585
n_c (656.27 nm)	1.54458	1.54367	1.54332	1.54322
n_r (706.52 nm)	1.54308	1.54210	1.54163	1.54158
Density (g/cm ³)	3.457	3.455	3.453	3.452

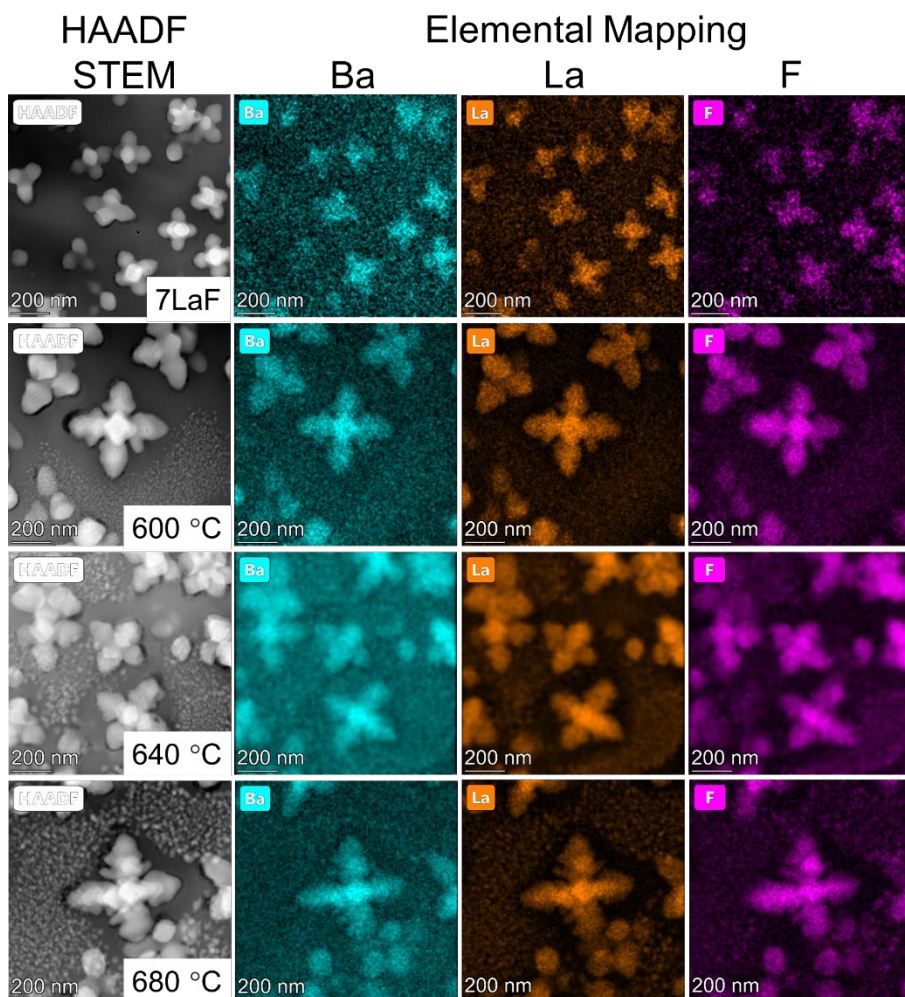


Figure 4-8 HAADF-STEM and EDS-mapping micrographs of 7LaF sample (the first row) and three 7LaF samples heat-treated at 600, 640, 680 °C for 4 hours, respectively (the second, third and fourth row). The third column: HAADF-STEM images; EDS-mapping elements: Ba, La and F (see the second, third and fourth columns, respectively). Figure adapted from Paper II.

To clarify the origin of the n trend with HT temperature, we perform HAADF-STEM and EDS-elemental mapping analyses on both Ba_2LaF_7 crystals and the remaining glass matrix. HAADF-STEM images and the EDS-element mapping images of Ba, La, and F atoms are shown in Figure 4-8. The EDS-element mapping images for other types of atoms are displayed in Paper II. It is seen that the sizes of two types of crystal and the concentrations of Ba, La, and F increase with increasing HT temperature. Some Ba^{2+} and nearly all the La^{3+} and F^- diffuse from the glass matrix to both the

existing flower-like Ba_2LaF_7 single-crystals and the small spherical Ba_2LaF_7 nanocrystals with increasing HT temperature. Owing to the escape of La^{3+} ions from the glass phase, the n values of the studied sample become lower, since La^{3+} ions are the main contributor to the n of glass (71).

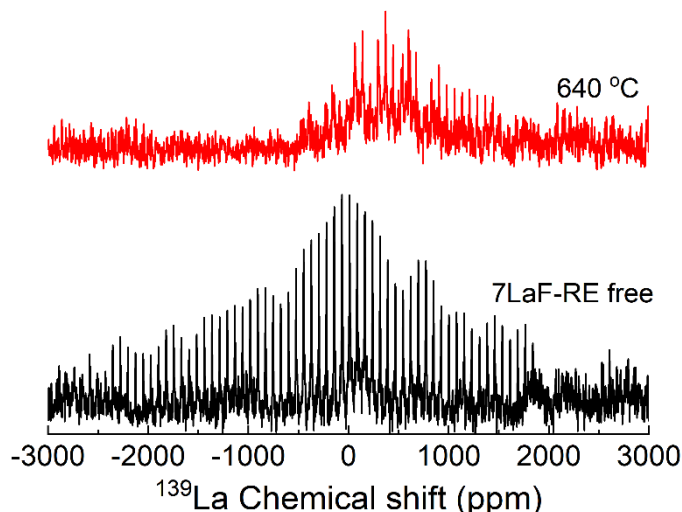


Figure 4-9 ^{139}La WURST-QCPMG NMR spectra of both 7LaF-RE free sample with the molar composition of $45\text{SiO}_2\text{-}15\text{Al}_2\text{O}_3\text{-}12\text{Na}_2\text{O-}21\text{BaF}_2\text{-}7\text{LaF}_3$ and 7LaF-RE free sample heat-treated at 640°C for 4 hours, respectively.

We perform the ^{139}La NMR measurements for 7LaF-RE free sample and the heat-treated one to probe the distribution of the La^{3+} ions, thus verifying the diffusion of La^{3+} ions from glass phase to Ba_2LaF_7 phase after HT. Figure 4-9 illustrates the ^{139}La NMR spectra, obtained by using the scheme of the WURST-QCPMG pulse, of both 7LaF-RE free sample and the heat-treated one. It can be noticed that some broad ^{139}La NMR signals dominated by magnetic shielding anisotropy and quadrupole interaction are observed from ^{139}La NMR spectra of 7LaF-RE free sample (65)(72). After HT at 640°C for 4 hours, it can be noticed the ^{139}La spectrum is narrowed with some new Ba_2LaF_7 crystals precipitated from glass matrix. This can be assigned to the diffusion of La^{3+} ions from glass phase to Ba_2LaF_7 crystal phase after HT (34).

4.3. UCL PERFORMANCES

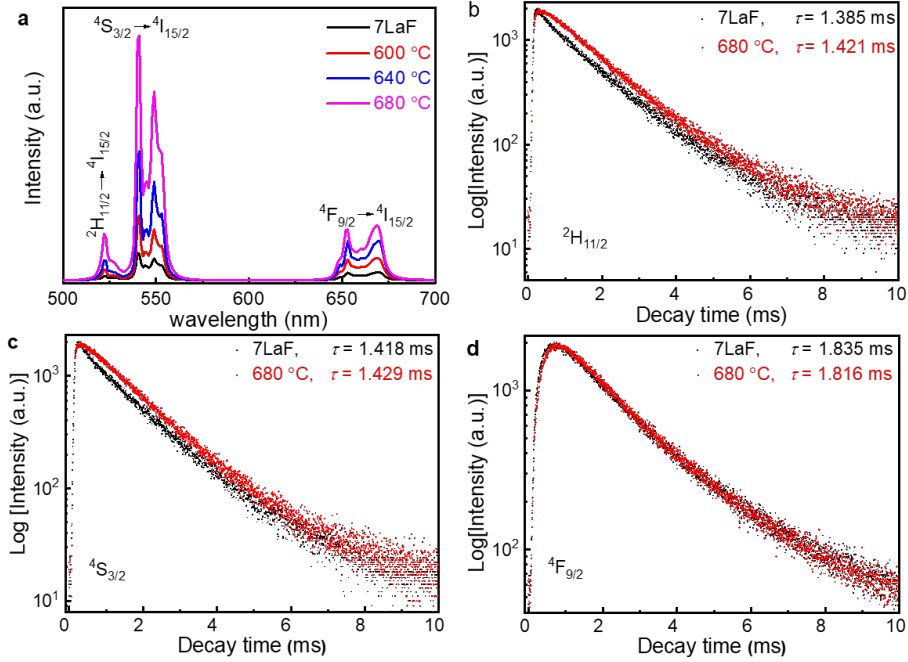


Figure 4-10 UCL spectra (a) of 7LaF sample and three 7LaF samples heat-treated at 600, 640, 680 °C for 4 hours, respectively, and decay lifetime of Er^{3+} in $2\text{H}_{11/2}$ (b), $4\text{S}_{3/2}$ (c) and $4\text{F}_{9/2}$ (d) states 7LaF sample and 7LaF samples heat-treated at 680 °C for 4 hours. Figure adapted from Paper II.

Figure 4-10a shows the UCL spectra of the four studied samples. The heat-treated samples exhibit the stronger UCL of Er^{3+} compared with 7LaF sample. This enhancement is described in three aspects. First, some Er^{3+} and Yb^{3+} ions in glass matrix can enter Ba_2LaF_7 crystals upon HT. Thus, the non-radiative relaxation rate of both Er^{3+} and Yb^{3+} ions decreases with increasing HT temperature, leading to the enhancement of UCL (36). Second, both the content of Ba_2LaF_7 crystals and the transmittance of the studied samples increase with the HT temperature, and thus, the UCL is enhanced by lowering light scattering. Third, as the concentrations of Er^{3+} and Yb^{3+} ions in Ba_2LaF_7 crystals increase with HT temperature, the distance between them in Ba_2LaF_7 crystals becomes shorter, resulting in an increased probability of energy transfer, and thereby enhancing the UCL. Furthermore, the increased energy transfer probability is verified by the UCL decay time of the studied samples (Figure 4-10b-d). The corresponding decay curves are well fitted by the second-order exponential decay mode and all the equations are described in Chapter 3. Thus, the values of the average lifetime τ for $2\text{H}_{11/2}$, $4\text{S}_{3/2}$, and $4\text{F}_{9/2}$ states increase with increasing HT temperature, implying higher energy transfer probabilities. For comparison, the

UCL of 7LaF sample is four times higher than that of the traditional GC (heat-treated 0LaF sample, details see Paper II). In addition, the UCL intensity of 7LaF sample heat-treated at 680 °C for 4 hours is increased by about 23 times compared with the traditional GC. Thus, the studied 7LaF sample is an excellent starting candidate for enhancing the UCL by proper HT.

4.4. SUMMARY

In this Chapter, we conduct HT above T_g for the translucent 7LaF samples at 600, 640 and 680 °C for 4 hours. Normally, HT leads to the increase of the fraction of Ba_2LaF_7 crystals with the growth and the formation of Ba_2LaF_7 crystals, thereby lowering the transmittance of GCs. Interestingly, the light transmittance of 7LaF samples increases with the increasing HT temperature, which contrasts with common sense. This anomalous phenomenon is attributed to the variation of the composition of the residual glass phases upon HT, that is, the depletion of La^{3+} , Ba^{2+} and F^- from the residual glass matrix. This leads to the fact that the n of the residual glass matrix approaches that of Ba_2LaF_7 crystals, thereby causing the low light scattering. In addition, as confirmed via the HRTEM images, the flower-like Ba_2LaF_7 crystals are single-crystals, which also contributes to the suppression of light scattering. Furthermore, the mechanism of both crystal formation and growth has been revealed by performing XRD, TEM and SEM analyses. The relationship between amorphous phase separation and crystallization of fluoride crystals of Ba_2LaF_7 has been clarified by HT. The glass connectivity and thermal stability increase with the increase of HT temperature. The structural evolutions and atom distribution of the studied samples after HT have been probed by NMR and TEM mapping, respectively. Finally, we found that the highly transparent oxyfluoride GC tailored by optimum HT can greatly enhance UC luminescence. Thus, compared with the melt-quenching derived 7LaF sample, the heat-treated one exhibits superior optical performances, which might inspire other host materials.

CHAPTER 5. MELTING

TEMPERATURE-DEPENDENT

OXYFLUORIDE GLASSES AND

GLASS-CERAMICS

In this Chapter, to investigate the structural origin of the formation of the Ba_2LaF_7 crystals during quenching, we are going to discuss the structural homogeneity of the samples prepared by quenching four glass melts from different melting temperatures of 1450, 1500, 1550 and 1590 °C, respectively. The melt-quenching derived oxyfluoride glasses and GCs are denominated as PG1450 (7LaF), PG1500, PG1550 and PG1590, respectively. To further study the crystallization behavior, the melt-quenching derived samples were heat-treated at their proper T_c values, which are named GC1450, GC1500, GC1550, and GC1590, respectively. The thermodynamic, structural and optical properties of both the melt-quenching derived and the heat-treated samples are detailed studied in Paper III.

5.1. CHARACTERIZATION OF MELT-QUENCHING DERIVED OXYFLUORIDE GLASSES AND GLASS-CERAMICS

5.1.1. THERMODYNAMIC ANALYSIS

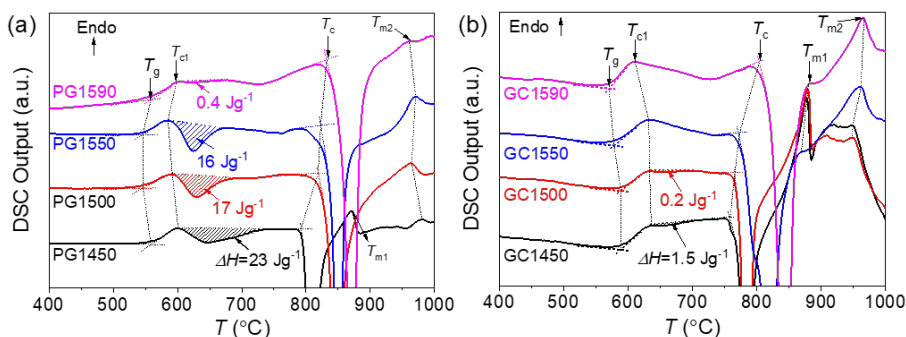


Figure 5-1 (a and b) DSC output curves of both the melt-quenching derived (PG1450, PG1500, PG1550 and PG1590) and the corresponding heat-treated samples (GC1450, GC1500, GC1550 and GC1590), respectively. The onset temperatures of T_g , T_{c1} , T_c , T_{m1} and T_{m2} are marked in Figure 5-1, respectively. The area of the first exothermic peak (i.e., the hatched area) represents ΔH determined by the extent of the crystal formation in each sample. Figure adapted from Paper III.

The DSC output curves of the melt-quenching derived samples are shown in Figure 5-1a. The onset temperatures of T_g , T_{c1} , T_c , T_{m1} and T_{m2} are determined from the DSC curves and their values are shown in Table 1, respectively. Both T_g and T_{c1} values exhibit a gradual decrease in PG1450, PG1500 and PG1550 and then a slightly increase in PG1590. This implies that glass network connectivity first decreases and then increases owing to both the tetrahedral depolymerizations damaged by fluoride and the volatilization of fluorides (SiF_4 and NaF) at higher melting temperatures. In addition, T_c gradually increases with increasing melting temperature, indicating that the main crystallization becomes more difficult owing to the more homogeneous melt at higher melting temperature. As T_{m1} in each of PG1500, PG1550 and PG1590 samples might be overlapped by its second crystallization peak, T_{m1} is only presented in the curve of PG1450 sample. The values of T_{m2} exhibit slight variation between the range of 961 and 981 °C in all curves of melt-quenching derived samples.

Table 5-1 The onset temperatures of T_g , T_{c1} , T_c , T_{m1} and T_{m2} of the melt-quenching derived and the heat-treated samples, respectively. Table adapted from Paper III.

T (°C)		T_g	T_{c1}	T_c	T_{m1}	T_{m2}
<i>samples</i>	PG1450	559	601	793	872	981
	PG1500	547	593	819	~	965
	PG1550	546	587	824	~	970
	PG1590	558	600	831	~	961
	GC1450	591	637	758	877	950
	GC1500	590	635	765	879	951
	GC1550	578	633	772	870	963
	GC1590	571	612	803	881	967

For the DCS curves of the corresponding heat-treated samples (Figure 5-1b), both T_g and T_{c1} values of the corresponding heat-treated samples increase upon HT compared with those of the melt-quenching derived samples, respectively. This means the concentration of $[\text{SiO}_4]$ and $[\text{AlO}_4]$ tetrahedral units increases upon HT, thus strengthening the glass network connectivity (73). However, the values of both T_g and T_{c1} in the heat-treated samples show a dropping tendency due to the volatilization of fluorides (SiF_4 and NaF) during melting at the higher temperature. The T_c value in each heat-treated sample decreases with HT compared with that in each melt-quenching derived sample, implying that the main crystallization in the remaining glass matrix becomes easier. However, the T_{m1} values in the heat-treated samples are similar to those in PG1450 sample. This indicates that these values are ascribed to the melting point of Ba_2LaF_7 crystals as these melting peaks appear in GC1500, GC1550 and GC1590 samples after HT. Meanwhile, each T_{m2} value of the heat-treated samples is lower than that of the melt-quenching derived samples (74).

To study the first crystallization event of the studied samples, ΔH calculated by integrating the first crystallization peak are shown in Figure 5-1, respectively. The values of ΔH for the melt-quenching derived samples (Figure 5-1a) gradually decrease with increasing the melting temperature, indicating that the first crystallization ability and the degree of structural heterogeneity decrease with increasing the melting temperature (75). For the heat-treated samples in Figure 5-1b, their values of ΔH become very small even close to zero. This implies that the first crystallization ability decreases even disappears after HT. Therefore, each heat-treated sample owns higher crystallinity than its melt-quenching derived sample.

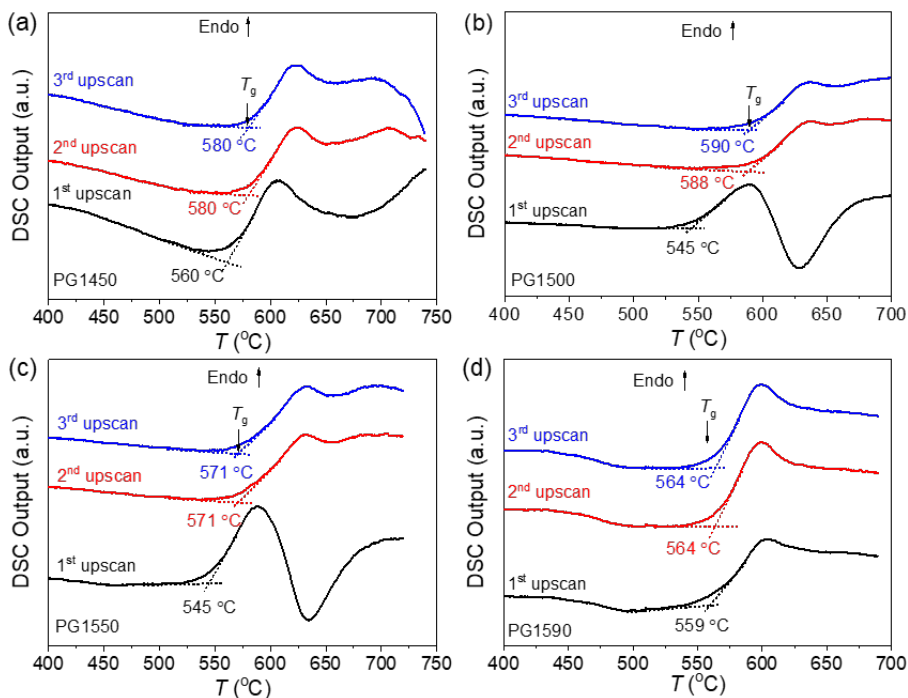


Figure 5-2 DSC output curves of PG1450 (a), PG1500 (b), PG1550 (c) and PG1590 (d) samples by repeated scan to $T_{\text{scan-max}}$ of 740, 700, 720, 690 °C, respectively, for three times at the same up-scan and down-scan rate of 10 °C/min. Figure adapted from Paper III.

The varied T_g values in each sample are determined from their corresponding DSC curves (Figure 5-2). Compared to the first (1st) up-scan, T_g values first sharply increase upon the second (2nd) up-scan and then increase slowly even unchangeable at the third (3rd) up-scan. Significantly, the area of the first crystallization peak in each DSC curve decreases with the number of cycles and then remains nearly constant. This could be explained by the formation of diffusion barrier at the interfaces between crystal and glass matrix after the 1st up-scan, which hinders the diffusion of F⁻, La³⁺, and Ba²⁺

ions to both the regions of existing Ba_2LaF_7 crystals and new nucleation sites (10). Thus, the glass network structure remains unchangeable.

5.1.2. GLASS STRUCTURAL ANALYSES

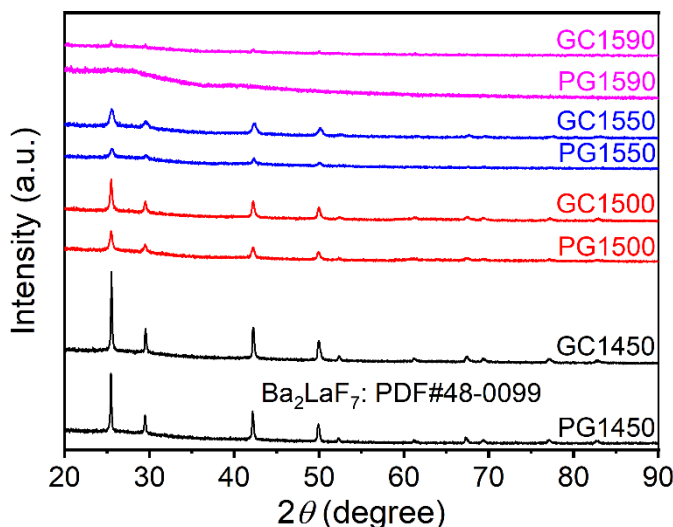


Figure 5-3 XRD patterns of PG1450, PG1500, PG1550, PG1590, GC1450, GC1500, GC1550 and GC1590 samples, respectively. Figure adapted from Paper III.

Figure 5-3 illustrates XRD patterns of the eight studied samples. It is seen that some obvious diffraction peaks are also found in PG1500 and PG1550 samples although their intensities become weaker with increasing the melting temperature. These peaks are also well attributed to the FCC Ba_2LaF_7 crystal (PDF#48-0099) (25). With further increasing the melting temperature, two weak and broad humps become evident in the XRD pattern of PG1590 sample, which belong to the characteristic diffraction peak of oxyfluoride glasses. This suggests that increasing the melting temperature can weaken the formation of Ba_2LaF_7 crystals in the melt-quenching derived samples due to the increase of structural homogeneity of the glass melt. Upon HT, the diffraction peaks in the XRD patterns of GC1450, GC1500 and GC1550 samples become more intensive. More importantly, several weak diffraction peaks corresponding to Ba_2LaF_7 crystal occur in the XRD pattern of GC1590 sample, which is similar to the crystallization behavior in traditional oxyfluoride glasses. In short, the content of Ba_2LaF_7 crystals in melt-quenching derived samples increases upon HT (76), which is consistent with the DSC results.

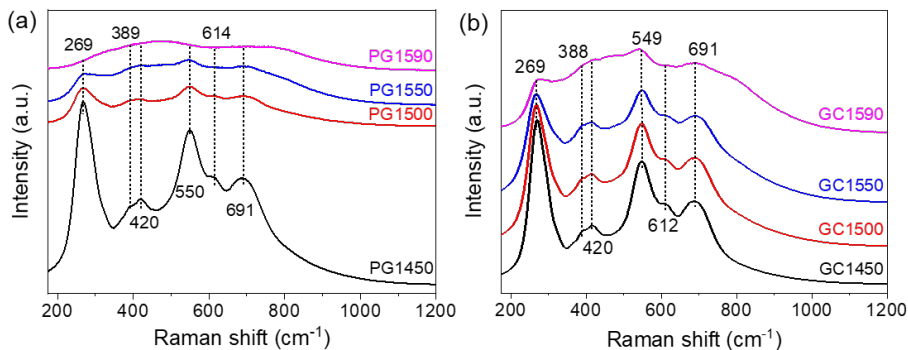


Figure 5-4 Raman spectra of the melt-quenching derived (a) and the heat-treated samples (b), respectively. Figure adapted from Paper III.

In Figure 5-4a, the Raman peak of Ba_2LaF_7 crystals (269 cm^{-1} , see Chapter 3) in PG1450, PG1500 and PG1550 samples becomes weaker and disappears with increasing the melting temperature, while appears two broad Raman peaks in the spectrum of PG1590. This also confirms the formation of Ba_2LaF_7 crystals in PG1450, PG1500 and PG1550 samples during the quenching process. In addition, the characteristic broad peaks verify the amorphous nature of PG1590 sample (39). The assignments for other Raman peaks are described in Paper IV and Paper III. Thus, the above results mean that the content of Ba_2LaF_7 crystals and the structural heterogeneity of the melt-quenching derived samples decrease with increasing the melting temperature (36)(77). To study the impact of HT on the microstructure of melt-quenching derived samples, we also conduct the Raman spectroscopy characterization for the heat-treated samples. The Raman spectra are illustrated in Figure 5-4b. Compared to the Raman spectra of PG1450, PG1500, and PG1550 in Figure 5-4a, the Raman peak corresponding to Ba_2LaF_7 crystal becomes stronger upon HT, consisting with the DSC and XRD results. Additionally, the weak Raman peaks of both Ba_2LaF_7 crystals at 269 cm^{-1} and tetrahedral units appear in GC1590 sample, implying that the crystallization takes place upon HT and lets the peaks of tetrahedral units observable.

To investigate the local coordination environment around Al^{3+} ions of the melt-quenching derived samples, we performed ^{27}Al MAS NMR measurements. ^{27}Al MAS NMR spectra (Figure 5-5) feature the main resonance of Al(IV) at about 60 ppm, indicating that the coordination environment of Al has no obvious change with increasing melting temperature. We have found that Al^{3+} ions can form $[\text{Al}(\text{O},\text{F})_4]$ and $[\text{Al}(\text{O})_4]$ tetrahedra, respectively, in both the interface regions and the glass network in PG1450 sample. However, due to the volatilization of F ions and the decrease of the area of fluoride-rich regions with increasing melting temperature, some Al-F linkages in the interface regions could be replaced by the Al-O linkages. This means that the coordination environment of Al could be slightly altered, while this variation cannot be detected.

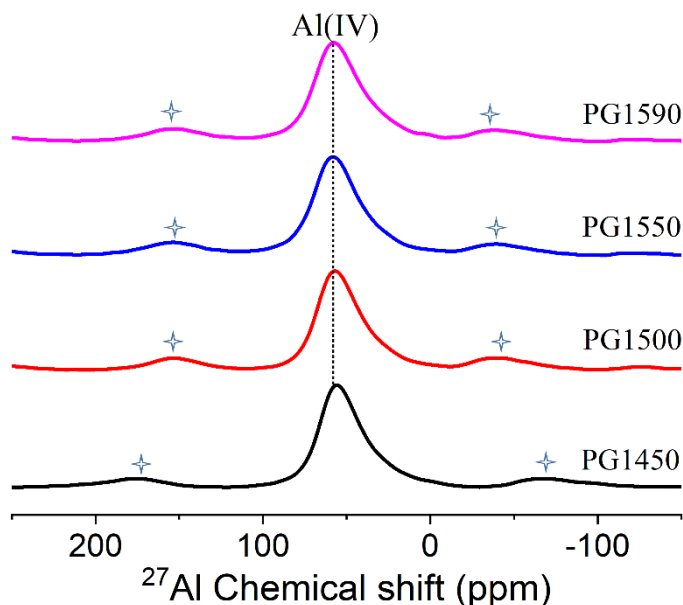


Figure 5-5 ^{27}Al MAS NMR spectra of PG1450, PG1500, PG1550 and the PG1590 samples, respectively. (★) denotes spinning sidebands. Figure adapted from Paper III.

5.1.3. MORPHOLOGY OF GLASSES AND GLASS-CERAMICS

Figure 5-6 shows the TEM images of PG1450, PG1590, GC1450 and GC1590 samples, respectively. As shown in Figure 5-6a, flower-like Ba_2LaF_7 crystals are present in the glass matrix of PG1450 (see Paper III), which size increases with the HT. Furthermore, some additional spherical Ba_2LaF_7 nanocrystals appear in glass matrix of GC1450 sample (Figure 5-6c, see Paper III). Figure 5-6b verifies the glassy nature of PG1590 sample as no distinct lattice fringes are observed. After HT, some ordered domains (about 10 nm) with regular lattice fringe denoted by the black dashed circles are present in the glass matrix (Figure 5-6d), which are also conformed to be Ba_2LaF_7 crystals by measuring the distance (0.35 nm) between (111) planes (Inset of Figure 5-6d).

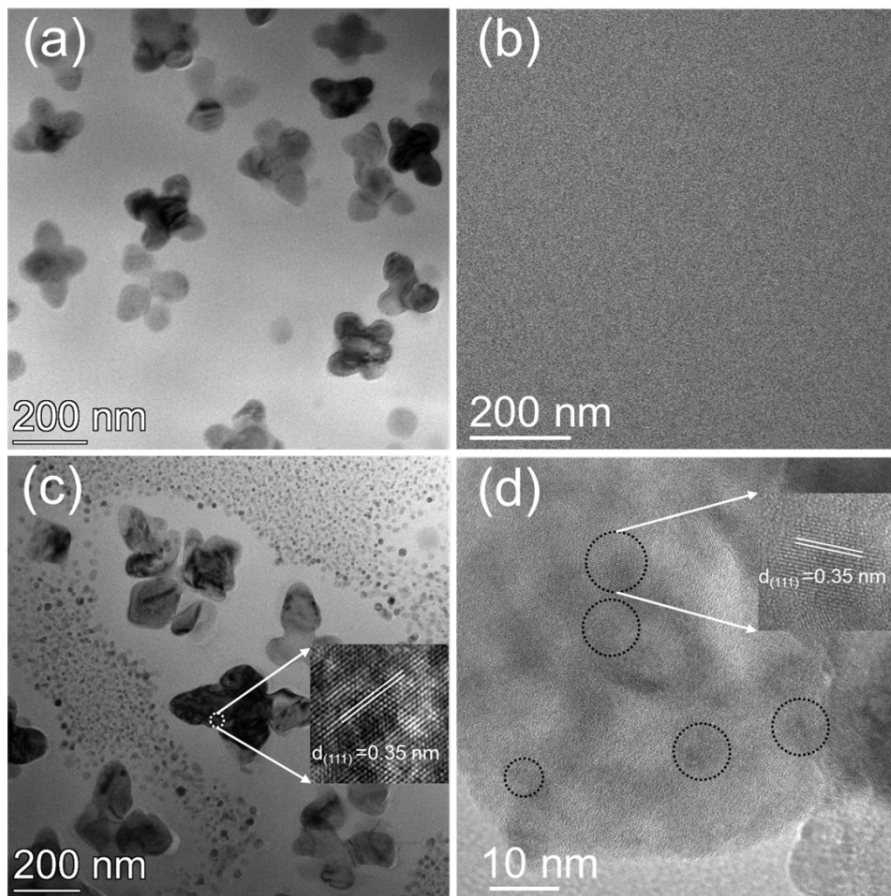


Figure 5-6 ACTEM images of PG1450 (a), PG1590 (b), GC1450 (c), and GC1590 (d) samples, respectively. Figure adapted from Paper III.

Figure 5-7 shows SEM graphs of the studied samples. It is seen that some flower-like Ba_2LaF_7 crystals (Figure 5-7a) are distributed uniformly in the parent glass matrix, which grows to a larger size, i.e., around 300 nm, upon HT along with some new-formed tiny spherical Ba_2LaF_7 crystals around 20 nm in glass matrix (Figure 5-7c). No crystals are observed in glass matrix of PG1590 (Figure 5-7b), which suggests that PG1590 is oxyfluoride glass. After HT, some tiny spherical nanocrystals approximate 20 nm precipitate from glass matrix (Fig. 5-7d) (78). The results agree well with those in TEM images.

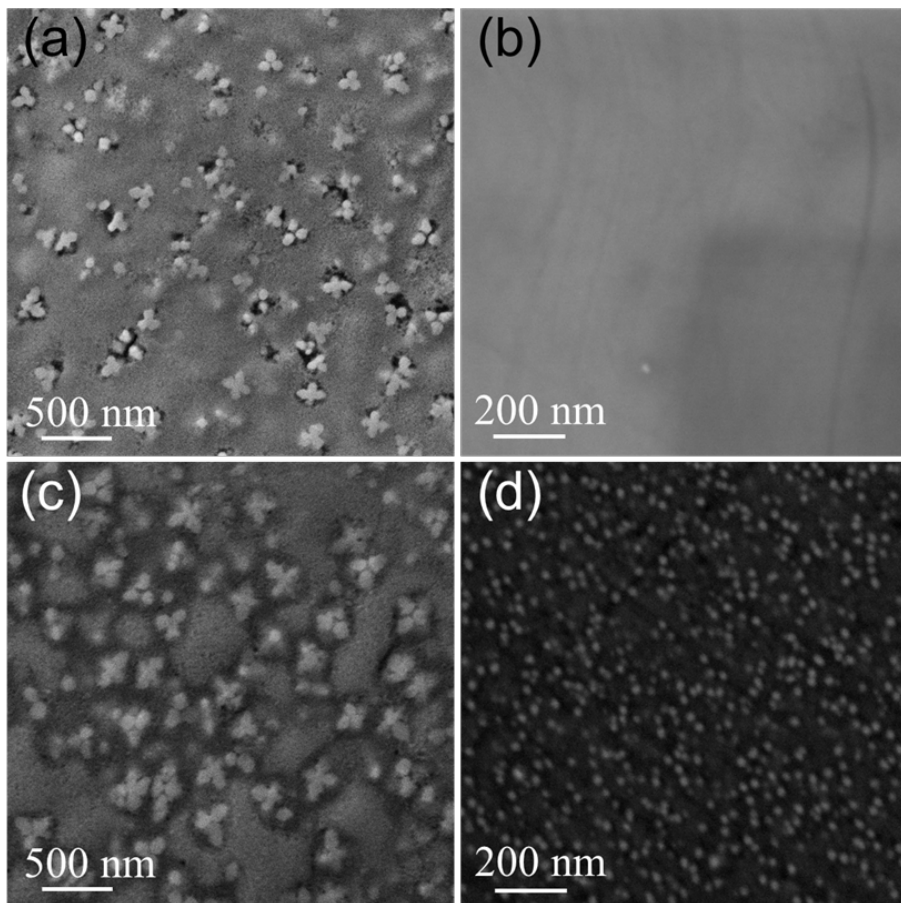


Figure 5-7 SEM graphs of PG1450 (a), PG1590 (b), GC1450 (c), and GC1590 (d) samples, respectively. For GC1450, white flower-like domains and grey regions are Ba_2LaF_7 crystals and tiny spherical Ba_2LaF_7 nanocrystals, respectively. For GC1590, small white dot regions are new-formed Ba_2LaF_7 nanocrystals embedded in glass matrix (large black areas). Figure adapted from Paper III.

5.2. OPTICAL PROPERTIES

5.2.1. TRANSMITTANCE SPECTRA

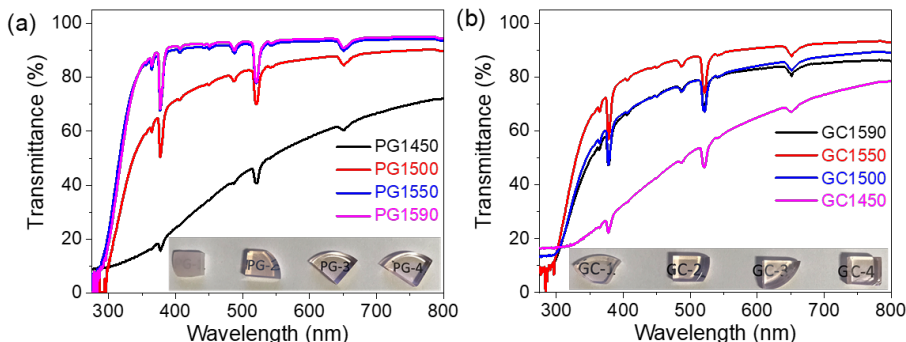


Figure 5-8 Transmittance spectra of the melt-quenching derived samples (a) and the corresponding heat-treated samples (b), respectively. Figure adapted from Paper III.

Figure 5-8 shows the transmittance spectra and the optical images (inset Figure 5-8) of the melt-quenching derived (a) and the heat-treated samples (b). Four main absorption peaks of Er^{3+} ions at around 378, 488, 522, and 653 nm are observed in the spectra, the attribution of which is described in Chapter 3. The light transmittance in Figure 5-8a gradually increases with increasing the melting temperature, illustrated by the highest light transmittance around 94% (per 1 mm) of PG1590 sample. The origin of the increase of light transmittance should be that the light scattering from both the size of Ba_2LaF_7 crystals and n differences between the Ba_2LaF_7 crystals and the remaining glass matrix decreases with increasing the melting temperature.

After HT, the optical transmittance of GC1500 sample is higher compared with that of PG1500 sample, which is similar to that of GC1450 samples (see Chapter 4). This is also an anomalous phenomenon that light transmittance increases with the increase of both size and fraction of Ba_2LaF_7 crystals (7). This implies that the HT can adjust the n of glass matrix to match that of Ba_2LaF_7 crystals, resulting in a decrease in light scattering. However, the light transmittance of PG1550 and PG1590 samples decreases upon HT, which means that the n differences between Ba_2LaF_7 crystals and glass matrix are smaller than those in GC1550 and GC1590 samples.

5.2.2. UCL SPECTRA

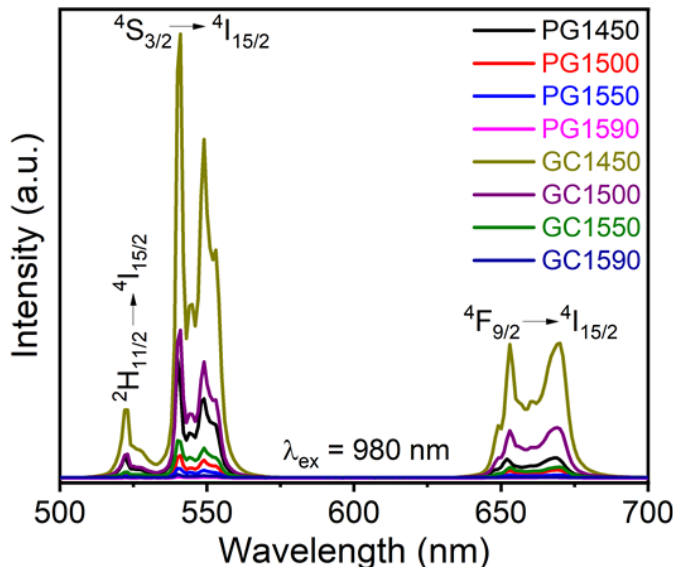


Figure 5-9 UCL spectra of $\text{Er}^{3+}\text{-Yb}^{3+}$ co-doped melt-quenching derived samples and the heat-treated samples, respectively. Figure adapted from Paper III.

Figure 5-9 shows the UCL spectra of the studied samples obtained by excitation of the 980 nm LD. The characteristic UCL peaks at 523, 541, and 653 nm were described in Chapter 3. The UCL intensity of the melt-quenching derived samples decreases with the increasing melting temperatures. In addition, the heat-treated samples exhibit higher UCL intensity and more pronounced Stark splitting of the energy levels compared with the corresponding melt-quenching derived samples (55). This can be attributed to the incorporation of more Er^{3+} ions into Ba_2LaF_7 nanocrystals with low phonon energy, which can reduce the probability of nonradiative relaxation and increase the possibilities of energy transfer between Er^{3+} and Yb^{3+} ions (79).

5.3. SUMMARY

In this Chapter, $\text{Er}^{3+}\text{-Yb}^{3+}$ co-doped melt-quenching derived oxyfluoride GCs and glass are prepared by adjusting the melting temperature. The effect of melting temperature on crystallization behavior, structural evolution and optical properties of the studied samples is investigated. The results show that the studied samples become more homogeneous with increasing melting temperature, and this lowers the formation of Ba_2LaF_7 crystals and decreases the crystallization capability determined by the enthalpy of the first crystallization peak. Interestingly, the transmittance of melt-quenching derived samples increases with increasing melting temperature, whereas the UCL decreases. The decreasing transmittance can be attributed to the fact

that the differences of n between oxide glass matrix and Ba_2LaF_7 crystals (fluoride-rich regions) get smaller. Upon HT, the heat-treated samples exhibit higher crystallinity and UCL compared with the corresponding melt-quenching derived samples. Thus, in this Chapter, we investigate a new path via controlling the melting temperature to design oxyfluoride glasses or GCs and clarify the impact of melting temperature on the structural origins of the melt-quenching derived samples. Importantly, this study also investigates the effect of HT on tailoring optical properties.

CHAPTER 6. OXYFLUORIDE GLASS-CERAMICS WITH VARYING LaF_3/YF_3 RATIO

We further investigate the impact of the ratio of LaF_3/YF_3 on the properties of melt-quenching derived oxyfluoride GCs. The derived samples are denominated as 7LaF, 5La2Y, 3La4Y, 1La6Y and 7YF, respectively. This content is mainly based on Paper V, which is in preparation for submission. In addition, the temperature sensing performances of the heat-treated 7YF sample are evaluated. All the detailed information about the preparation, characterization and optical performances of the melt-quenching derived oxyfluoride GCs could be found in Paper V and Paper I.

6.1. THERMODYNAMIC ANALYSIS

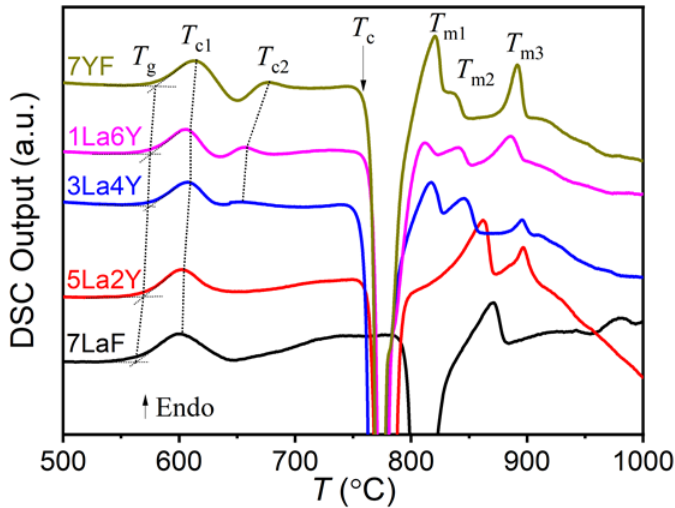


Figure 6-1 DSC curves of 7LaF, 5La2Y, 3La4Y, 1La6Y and 7YF samples, respectively. The onset temperatures of T_g , T_{c1} , T_{c2} , T_c , T_{m1} , T_{m2} and T_{m3} are marked in Figure, respectively. Figure adapted from Paper V.

DSC output curves of the studied samples are shown in Figure 6-1 which are a function of temperature ($^{\circ}\text{C}$). The onset temperatures of T_g , T_{c1} , T_{c2} , T_c , T_{m1} , T_{m2} and T_{m3} are determined by the method mentioned in Chapter 3, the values of which are shown in Table 6-1. It is seen that the values of both T_g and T_{c1} varied with increasing the content of YF_3 , which means the glass network connectivity becomes higher since the glass structure determines T_g and T_{c1} (46). Moreover, the area of the first

crystallization peak gradually decreases and the second one slowly appeared with increasing content of YF₃, implying that crystallization ability for the first crystallization peak decreases with increasing the content of YF₃, while that for the second one increases. The values of T_c , T_{m1} , T_{m2} and T_{m3} also exhibit variation in the curves of the studied samples.

Table 6-1 The onset temperatures of T_g , T_{c1} , T_{c2} , T_c , T_{m1} , T_{m2} and T_{m3} of 7LaF, 5La2Y, 3La4Y, 1La6Y and 7YF samples, respectively. Figure adapted from Paper V.

<i>Sample</i>	T_g	T_{c1}	T_{c2}	T_c	T_{m1}	T_{m2}	T_{m3}
7LaF	561	602	~	790	872	958	~
5La2Y	569	606	~	758	862	897	~
3La4Y	574	609	652	752	818	846	897
1La6Y	576	610	659	759	812	841	886
7YF	580	617	678	760	821	982	891

6.2. GLASS STRUCTURAL ANALYSES

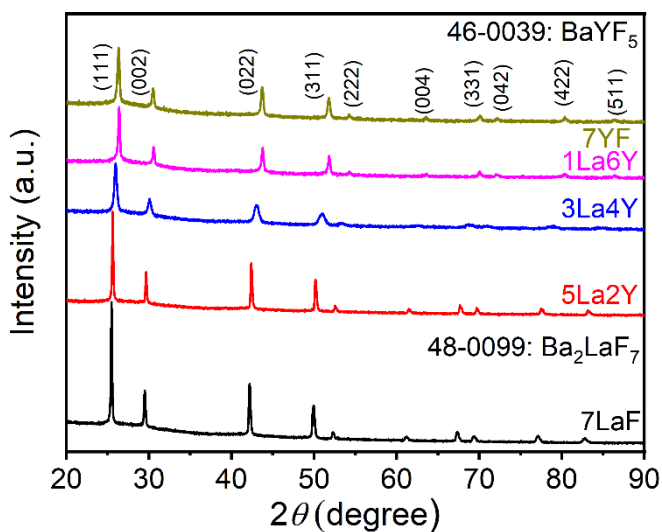


Figure 6-2 XRD patterns of 7LaF, 5La2Y, 3La4Y, 1La6Y and 7YF samples, respectively. Figure adapted from Paper V.

The XRD patterns in Figure 6-2 shift gradually from cubic Ba₂LaF₇ crystals in 7LaF sample to BaYF₅ crystals (PDF#46-0039) in the 7YF sample with increasing the dopant ratio of YF₃/LaF₃. It can be seen that BaYF₅ crystals also take place during quenching and show ten characteristic diffraction peaks in the 2θ range from 20° to

90°, the peak positions of which slightly shift to larger angles compared with that of Ba_2LaF_7 crystals (see Paper II). In addition, the crystals formed in the 3La4Y sample can be deduced to complex fluorite crystals rather than mixed crystals of Ba_2LaF_7 and BaYF_5 (80).

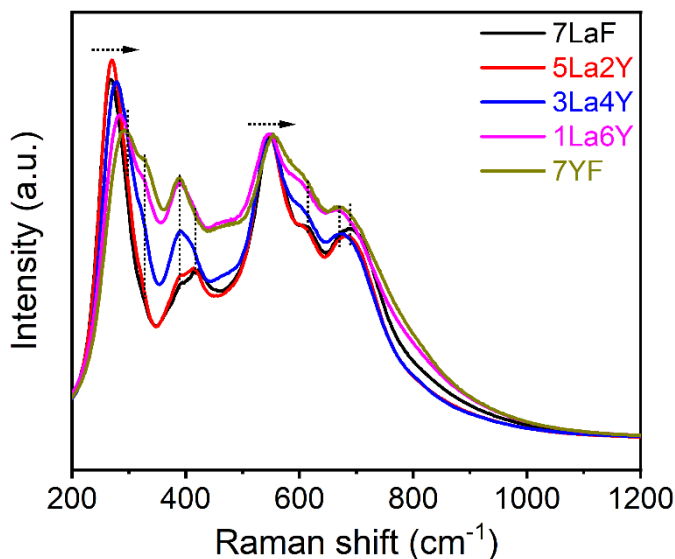


Figure 6-3 Normalized Raman spectra of 7LaF, 5La₂Y, 3La₄Y, 1La₆Y and 7YF samples, respectively. Figure adapted from Paper V.

Figure 6-3 shows the Raman spectra of the studied samples, which are normalized by the intensity of the peak at around 548 cm^{-1} . It is found that the intensity ratios between the crystalline peaks at 270 cm^{-1} and the tetrahedral peaks at 548 cm^{-1} first slightly increase and then decrease with substituting YF_3 for LaF_3 . This means that the crystallinity in the studied samples exhibits the same tendency as intensity ratios. In addition, the sharp Raman peak at 268 cm^{-1} gradually shifts to 294 cm^{-1} and a new weak Raman peak at around 327 cm^{-1} appears by substituting LaF_3 with YF_3 . Thus, the Raman peaks of 294 and 328 cm^{-1} can be ascribed to the vibrations of the Ba-F and Y-F bonds, respectively, in BaYF_5 crystals (61). Thus, based on the results in Chapter 3, we assume that the Raman peak at 268 cm^{-1} can be attributed to a combined vibrational Raman peak of the La-F and Ba-F bonds in Ba_2LaF_7 crystals, which needs to be approved in further study. For the Raman peaks of tetrahedral units, the Raman peak at 387 cm^{-1} increases with the variation of the composition, while the Raman peak at 417 cm^{-1} gradually disappears. Other main Raman peaks of 689, 616 and 548 cm^{-1} progressively move to 667, 604 and 554 cm^{-1} , respectively, with replacing LaF_3 to YF_3 in the compositions. Specifically, the mid-frequency bands at 350-700 cm^{-1} are associated with the Si-O-Si (Al) symmetric stretching vibration in the glass matrix (62)(63). The peak of 387 cm^{-1} is assigned to a symmetric stretch of five-fold ring

structures while the peaks at 550 and 604 cm^{-1} are attributed to the symmetric stretch of four- and three-fold ring structures, respectively (64) (see Chapter 4).

6.3. MORPHOLOGY FEATURES

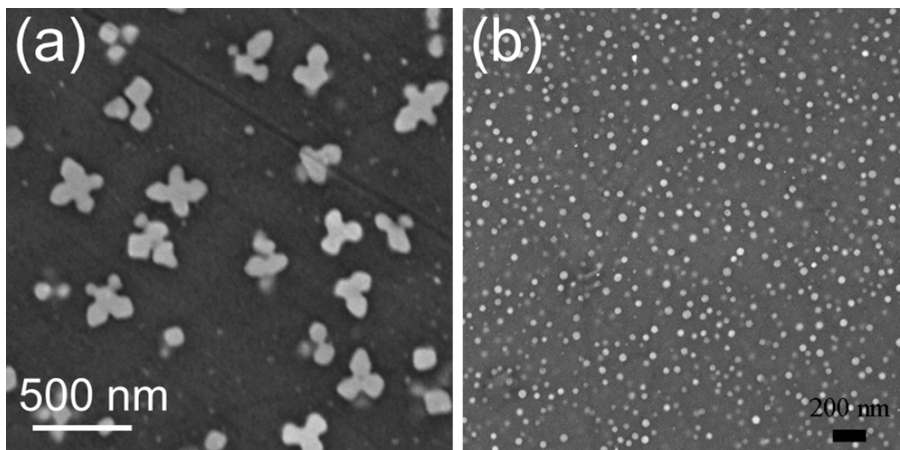


Figure 6-4 SEM images obtained from backscattered electron mode of 7LaF (a) and 7YF (b) samples without etching by HF acid, respectively. Figure adapted from Paper IV and Paper I.

Figure 6-4 shows SEM micrographs of the studied samples. It is seen that some flower-like Ba_2LaF_7 crystals (light regions, Figure 6-4a) are distributed uniformly in glass matrix (black region), which is described in chapter 3. By substituting LaF_3 with YF_3 , some nanosized sphere-shaped crystals (represented by light domains) with an average size of around 30 nm are observed in glass matrix (Figure 6-4b), which means that the size and fraction of crystals decrease. These results agree well with those in the XRD and Raman spectra. This also shows that the variation of composition may alter the microstructure in the studied samples, that is, the area and shape of fluoride-rich regions in the phase-separated oxyfluoride glass, which needs to be further investigated.

6.4. OPTICAL PERFORMANCES

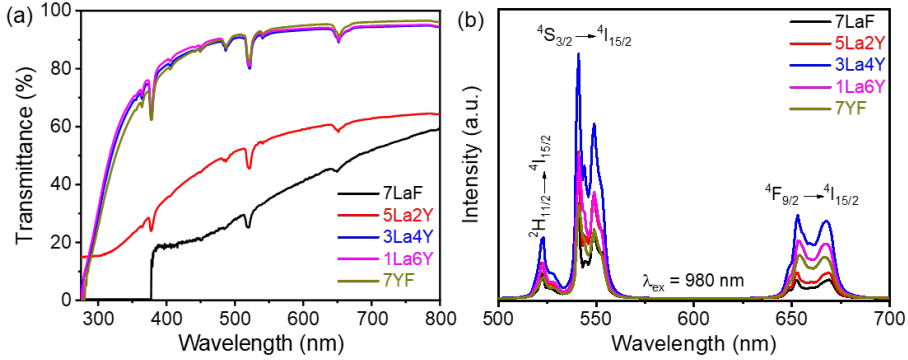


Figure 6-5 Transmittance spectra (a) and UCL spectra (b) of Er³⁺-Yb³⁺ co-doped 7LaF, 5La2Y, 3La4Y, 1La6Y and 7YF samples, respectively. Figure adapted from Paper V.

The light transmittance (Figure 6-5a) of the studied samples increases with substituting LaF₃ to YF₃, thereby resulting in low light scattering, which benefits to enhance optical performance. The reason for the increase in light transmittance is similar to that mentioned in Chapter 4. The UCL spectra of the studied samples are shown in Figure 6-5b, their intensity of 3La4Y sample is about 2.5 times higher than that of 7LaF sample, while 7YF sample possesses the weakest UCL. The detailed descriptions of UCL are mentioned in Chapter 3. The origin of the UCL intensity first increases and then decreases with substituting LaF₃ to YF₃ can be assigned to the following two factors. First, the UCL intensity is dependent on the light scattering. Although the fraction of complex fluorite crystals in the 3La4Y sample is slightly lower than that in 7LaF sample, the optical transmittance of 7LaF sample leads to relatively weak UCL due to the strongest light scattering. Second, the crystallinity main affects the UCL intensity of the 7YF sample. The fraction of BaYF₅ crystals is lower compared with that of complex fluorite crystals, which decreases the concentration of Er³⁺ and Yb³⁺ ions in the crystals and results in a decrease in energy transfer possibilities, thereby lowering the UCL intensity (see chapter 3).

6.5. APPLICATION OF NON-CONTACT OPTICAL TEMPERATURE SENSING

It is known that Er³⁺ ions doped oxyfluoride GCs can be used in various potential applications. However, the application of non-contact optical temperature sensing will be significant because it can precisely and conveniently measure the environment temperature. The principle for measuring temperature is via calculating the fluorescence intensity ratio (FIR) between $^2H_{11/2}$ and $^4S_{3/2}$ states, the thermally coupled energy levels (TCEs), of Er³⁺ ions to evaluate the environment temperature

(81)(82)(83). Thus, we assess the temperature sensing ability of the heat-treated 7YF sample. Detailed information could be found in paper V.

To investigate the effect of temperature variation between 313 and 473 K on the peak intensity at 523 nm ($^2H_{11/2}$), their peak intensities are normalized by the peak intensities at 541 nm ($^4S_{3/2}$) (Figure 6-6). It is obvious that the corresponding FIR values increase with increasing the environment temperature owing to the population inversion through the transition from $^4S_{3/2}$ to $^2H_{11/2}$ state via the annihilation of phonons.

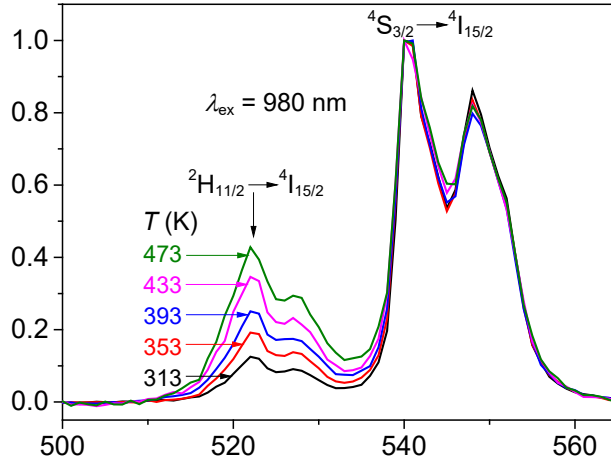


Figure 6-6 Normalized UCL spectra of the heat-treated 7YF sample at the temperature range from 313 to 473 K. Figure adapted from Paper I.

The FIR between I_H and I_S , that is the UCL intensities from $^2H_{11/2}$ and $^4S_{3/2}$ levels, respectively, can be related to the absolute temperature (T) based on the Boltzmann distribution theory, this relation is shown below:

$$FIR = \frac{I_H}{I_S} = C e^{-\frac{\Delta E}{K_B T}} \quad (6-1)$$

For the equation 6-1, ΔE is the effective energy gap between the two levels of Er^{3+} ions, C is a temperature-independent constant, and K_B is the Boltzmann constant (27)(84). Thus, the fitting curve (black) is shown in Figure 6-7a, which exhibits the strong temperature dependence of the FIR between the corresponding transitions of Er^{3+} ions in the heat-treated 7YF sample. The monolog plot of $\ln(FIR)$ versus inverse absolute temperature ($1/T$) was illustrated in Figure 6-7b. This curve can be fitted by the following equation (79):

$$\ln(FIR) = 1.54 - 1134 \frac{1}{T} \quad (6-2)$$

It gives the slope ($\Delta E/k_B$) of -1134 and the ΔE is determined to be 787 cm^{-1} , being close to ΔE (812 cm^{-1}) calculated from transmittance spectra. The relative temperature sensitivity (S_R) is an important parameter, which is defined as the relative change of the FIR value concerning temperature variation. Thus, high S_R can be expected in the heat-treated 7YF sample, which can be defined as the following equation:

$$S_R = \left| \frac{1}{FIR} \frac{d(FIR)}{dT} \right| = \frac{\Delta E}{K_B T^2} \quad (6-3)$$

As shown in Figure 6-7a (red fitting curve), The S_R value ($1134/T^2$) of the heat-treated 7YF sample can be obtained from the equation 6-3 by fitting the experimental data. To compare S_R values of the studied sample and that of other materials reported previously, the corresponding S_R values are listed in Table 6-2. It can be found that the S_R values of the studied sample are larger than those of other materials. Additionally, the S_R values are in the range of 0.51-1.15% K^{-1} for the experimental temperature range of 473-313 K. This means that the studied sample exhibits high sensitivity to measure environment temperature. Moreover, 10 cycles of the heating-cooling process in the sample temperature range for the heat-treated 7YF sample are conducted in order to evaluate the thermal stability of the UCL. The FIR values derived from 10 cycles are very similar to those in this study (Figure 6-8), which indicates that the temperature-dependent UCL behavior of the heat-treated 7YF sample is repeatable for the cycling experiments. Moreover, the reversible properties of the heat-treated 7YF sample should result from the protecting role of the oxide glass matrix for the fluoride crystals. Thus, the heat-treated 7YF sample is an excellent candidate for measuring environment temperature.

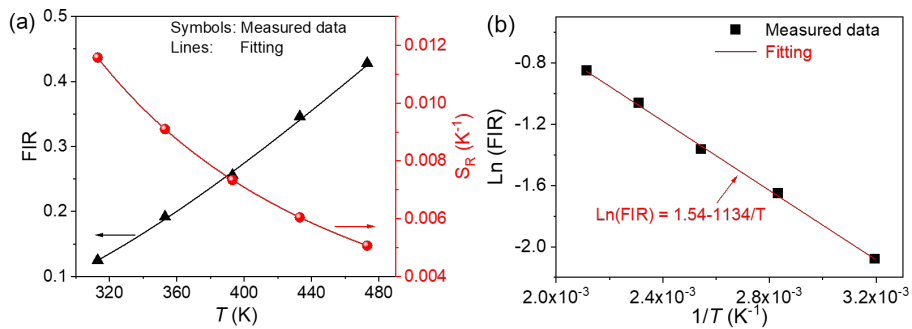


Figure 6-7 (a) Black fitting curve: Temperature dependence of FIR between ${}^2\text{H}_{11/2} \rightarrow {}^4\text{I}_{15/2}$ and ${}^4\text{S}_{3/2} \rightarrow {}^4\text{I}_{15/2}$ transitions of Er^{3+} of the 7YF sample. (b) Red fitting curve: The sensitivity S_R of the heat-treated 7YF sample. Figure adapted from Paper I.

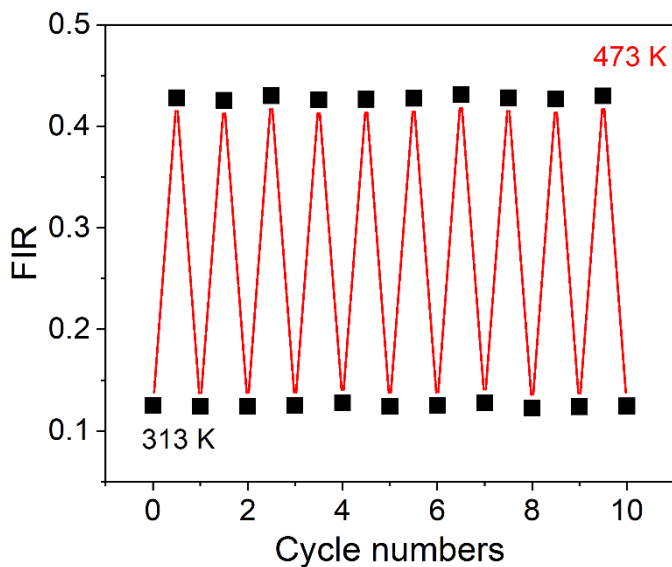


Figure 6-8. Temperature-induced switching of FIR of the heat-treated 7YF sample (alternating between 313 and 473 K). Figure adapted from Paper I.

Table 6-2 ΔE and S_R of several typical FIR-based optical temperature sensors based on UC luminescence from $^2H_{11/2}$ and $^4S_{3/2}$ levels of Er^{3+} ions. Table adapted from Paper I.

Sensing materials	T range (K)	ΔE (cm^{-1})	S_R ($\%K^{-1}$)	Ref.
BaYF ₅ : heat-treated 7YF	313-473	787	1134/ T^2	This work
Mn ²⁺ : ZnGa ₂ O ₄ NG	323-523	-	2.51	(85)
Sr ₂ YbF ₇ : GC	300-500	786	1129.8/ T^2	(86)
NaYF ₄ : GC	298-693	774	1117.4/ T^2	(87)
NaYF ₄ : phosphors	290-320	715	1028/ T^2	(88)
TeO ₂ -WO ₃ : glasses	300-690	679	976.8/ T^2	(89)
silicate glass	296-723	413	593/ T^2	(90)
Fluorophosphate glass	77-500	390	559/ T^2	(91)

6.6. SUMMARY

In this Chapter, we further investigate the impact of the ratio of LaF_3/YF_3 in the chemical composition on the properties of melt-quenching derived oxyfluoride GCs. By increasing the ratio of YF_3/LaF_3 in the chemical composition, we found that a series of fluoride crystals such as complex fluoride crystals and BaYF_5 crystals can be formed during quenching via adjusting the composition. This led to the decrease of the fraction of fluoride crystals, which was verified by the results of XRD and Raman spectra. In addition, the derived samples become gradually transparent and the UCL first increases and then decreases with the variation of the composition. Thus, 3La4Y sample containing complex fluorite crystals exhibits the highest UCL intensity, indicating that it can be a promising host material. Furthermore, glass network connectivity increases with increasing the content of YF_3 , which is determined by the increase of both T_g and T_{c1} values.

For the optical application, we evaluate the temperature sensing ability of the heat-treated 7YF sample. The maximum S_R is determined to be $1.15\% \text{ K}^{-1}$ at 313 K, which is higher than those of the Er^{3+} doped glasses and GCs reported previously. during 10 cycles of the heating-cooling process in the temperature range of 473-313 K, the heat-treated 7YF sample exhibits stable UCL intensity and FIR ratios, thus showing superior sensing capacity. This should be assigned to the protecting role of the oxide glass matrix for the fluoride crystals. Thus, the heat-treated 7YF sample is an excellent candidate for measuring environment temperature.

CHAPTER 7. CONCLUSIONS AND PERSPECTIVE

7.1. CONCLUSIONS

Traditional oxyfluoride glass-ceramics (GCs) have been regarded as promising host materials due to their excellent mechanical, thermal and optical properties, however, the low luminescent efficiency cannot meet their requirements for optical applications. Thus, this needs to be enhanced by forming large-sized fluoride crystals in the oxide glass matrix. Therefore, to achieve this goal, the chemical composition was altered in our project by using two strategies, i) substituting lanthanum oxide (La_2O_3) with lanthanum fluoride (LaF_3) in the composition of traditional oxyfluoride GCs, ii) adjusting the melting temperature of the composition of the translucent sample. These tailor glass microstructure, crystallization behavior and optical properties of the Er^{3+} - Yb^{3+} ions codoped melt-quenching derived oxyfluoride GCs.

By varying the chemical composition via substituting La_2O_3 with LaF_3 , the results show that fluoride-rich domains increase with increasing the content of LaF_3 , which agrees well with the results of Molecular Dynamic (MD) simulations. This led to the decrease of crystallization activation energy for precipitating fluoride crystals and the formation of Ba_2LaF_7 crystals during the quenching process. In addition, the optical transmittance of the studied samples decreases with the variation of chemical composition, which results from the strong light scattering via increasing the fraction and the size of crystals, whereas the up-conversion luminescence (UCL) intensities increased. Thus, this composition-dependent strategy can provide us with a new perspective to enhance the UCL, though this strategy leads to a decrease in light transmittance. To investigate the structural evolution and enhance the optical properties of the translucent 7LaF samples, heat treatment (HT) was conducted at different temperatures. It is anomalous that the light transmittance of 7LaF samples increases with the increasing HT temperature. It is observed that the melt-quenching derived Ba_2LaF_7 single-crystals increase with increasing HT temperature. Moreover, some new Ba_2LaF_7 single crystals precipitate from the fluoride-rich regions, which supports that phase separation would assist the formation of fluoride crystals. Furthermore, HT resulted in the compositional variation in the residual glass matrix, causing the fact that the refractive index (n) of the residual glass matrix approaches that of the Ba_2LaF_7 crystals. Consequently, 7LaF sample heat-treated at 680 °C exhibits the highest light transmittance. Therefore, the optimum HT can not only increase the light transmittance but also further enhance the UCL.

The impact of the ratio of LaF_3/YF_3 on the properties of melt-quenching derived oxyfluoride GCs was also investigated. By adjusting the composition, a series of

fluoride crystals can be formed during quenching, which leads to a decrease in crystallinity. Additionally, the derived samples become transparent with the variation of the composition. The 3La4Y sample exhibits the highest UCL intensity, indicating that it can be a promising host material compared with 7LaF sample. For the optical application, the temperature sensing performance of the heat-treated 7YF sample was evaluated. The relative temperature sensitivity (S_R) of the studied sample is higher than that of the Er^{3+} doped glasses and GCs reported previously. In addition, the heat-treated 7YF sample exhibits stable sensing capacity during 10 heating-cooling cycles in the temperature range of 473-313 K owing to the protecting role of the oxide glass matrix for the fluoride crystals. This means the heat-treated 7YF sample is an excellent candidate for measuring environment temperature.

In addition to the composition strategy, the melting temperature strategy for the compositions of 7LaF sample was investigated. We discovered that the crystallization capability of the studied samples decreases with increasing the melting temperature, whereas the light transmittance increases and the UCL weakens. The lowered light transmittance is attributed to the fact that the studied samples become more heterogeneous than those prepared at higher melting temperatures. Thus, this strategy offers a new path to design melt-quenching derived glass and GCs. Moreover, HT can be used for tailoring the properties of the melt-quenching derived oxyfluoride glass and GCs.

7.2. PERSPECTIVE

In this thesis, we have discussed glass microstructure, crystallization behavior and optical properties of different melt-quenching derived oxyfluoride glass and GCs and also investigated the impact of HT on the properties of the studied samples. However, the following research still need to be further investigated.

Through the variation of chemical composition by varying the ratio of network modifiers, we have successfully synthesized some melt-quenching derived oxyfluoride GCs. The studied samples are a new kind of host material for enhancing optical properties. Such research is at the beginning and needs to be further explored. In addition, the formation mechanism of the fluoride crystals during quenching is still clear, which needs to be investigated in the future. Some characterizations such as High-temperature viscosity, liquid-liquid immiscibility and heterogeneity of glass melts will be helpful to understand this mechanism. We also should verify the strategy of HT leading to the translucence-transparency transformation that could be used for other translucent GCs. We will design the optimum chemical composition, melting temperature and subsequent HT temperature to tailor the oxyfluoride GCs with specific optical properties, thus achieving micro-cavity or random laser outputs based on high transmittance and crystallization of the heat-treated samples.

BIOGRAPHY

1. Gonçalves MC, Santos LF, Almeida RM. Rare-earth-doped transparent glass ceramics. *Comptes Rendus Chim.* 2002;5(12):845–54.
2. Deng R, Qin F, Chen R, Huang W, Hong M, Liu X. Temporal full-colour tuning through non-steady-state upconversion. *Nat Nanotechnol.* 2015;10(3):237–42.
3. Lv S, Cao M, Li C, Li J, Qiu J, Zhou S. In-Situ Phase Transition Control in the Supercooled State for Robust Active Glass Fiber. *ACS Appl Mater Interfaces.* 2017;9(24):20664–70.
4. Xu X, Zhang W, Yang D, Lu W, Qiu J, Yu SF. Phonon-Assisted Population Inversion in Lanthanide-Doped Upconversion Ba_2LaF_7 Nanocrystals in Glass-Ceramics. *Adv Mater.* 2016;28(36):8045–50.
5. Zhao Z, Hu F, Cao Z, Chi F, Wei X, Chen Y, et al. Self-crystallized Ba_2LaF_7 : $\text{Nd}^{3+}/\text{Eu}^{3+}$ glass ceramics for optical thermometry. *Ceram Int.* 2017;43(17):14951–5.
6. Wang Y, Ohwaki J. New transparent vitroceramics codoped with Er^{3+} and Yb^{3+} for efficient frequency upconversion. *Appl Phys Lett.* 1993;63(24):3268–70.
7. Liu X, Zhou J, Zhou S, Yue Y, Qiu J. Transparent glass-ceramics functionalized by dispersed crystals. *Prog Mater Sci.* 2018;97:38–96.
8. Qiao A, Bennett TD, Tao H, Krajnc A, Mali G, Doherty CM, et al. A metal-organic framework with ultrahigh glass-forming ability. *Sci Adv.* 2018;4(3):1–8.
9. Krieke G, Sarakovskis A. Crystallization and upconversion luminescence of distorted fluorite nanocrystals in Ba^{2+} containing oxyfluoride glass ceramics. *J Eur Ceram Soc.* 2016;36(7):1715–22.
10. Lin C, Bocker C, Rüssel C. Nanocrystallization in Oxyfluoride Glasses Controlled by Amorphous Phase Separation. *Nano Lett.* 2015;15(10):6764–9.
11. Bocker C, Wiemert J, Rüssel C. The formation of strontium fluoride nano crystals from a phase separated silicate glass. *J Eur Ceram Soc.* 2013;33(10):1737–45.

12. Bocker C, Rüssel C, Avramov I. Transparent nano crystalline glass-ceramics by interface controlled crystallization. *Int J Appl Glas Sci*. 2013;4(3):174–81.
13. Stoica M, Brehl M, Bocker C, Herrmann A, Rüssel C. Microstructure and luminescence of erbiumdoped $\text{Na}_2\text{O}/\text{K}_2\text{O}/\text{CaO}/\text{CaF}_2/\text{Al}_2\text{O}_3/\text{SiO}_2$ nano glass-ceramics. *Mater Chem Phys*. 2018;207:36–43.
14. Lin C, Rüssel C, Dai S. Chalcogenide glass-ceramics: Functional design and crystallization mechanism. *Prog Mater Sci*. 2018;93:1–44.
15. Sun K, Tan D, Fang X, Xia X, Lin D, Song J, et al. Three-dimensional direct lithography of stable perovskite nanocrystals in glass. *Science*. 2022;375(6578):307–10.
16. Bhattacharyya S, Boeker C, Heil T, Jinschek JR, Höche T, Rüssel C, et al. Experimental evidence of self-limited growth of nanocrystals in glass. *Nano Lett*. 2009;9(6):2493–6.
17. Hoell A, Varga Z, Raghuwanshi VS, Krumrey M, Bocker C, Rüssel C. ASAXS study of CaF_2 nanoparticles embedded in a silicate glass matrix. *J Appl Crystallogr*. 2014;47(1):60–6.
18. Bocker C, Rüssel C. Self-organized nano-crystallisation of BaF_2 from $\text{Na}_2\text{O}/\text{K}_2\text{O}/\text{BaF}_2/\text{Al}_2\text{O}_3/\text{SiO}_2$ glasses. *J Eur Ceram Soc*. 2009;29(7):1221–5.
19. Rüssel C. Nanocrystallization of CaF_2 from $\text{Na}_2\text{O}/\text{K}_2\text{O}/\text{CaO}/\text{CaF}_2/\text{Al}_2\text{O}_3/\text{SiO}_2$ glasses. *Chem Mater*. 2005;17(23):5843–7.
20. Bohren CF, Huffman DR. Rayleigh-Gans Theory. In: *Absorption and Scattering of Light by Small Particles*. 2007.
21. Zheng G, Xiao W, Wu J, Liu X, Masai H, Qiu J. Glass-Crystallized Luminescence Translucent Ceramics toward High-Performance Broadband NIR LEDs. *Adv Sci*. 2022;2105713:1–8.
22. Jiang T, Qin W, Zhao D. Size-dependent upconversion luminescence in CaF_2 : Yb^{3+} , Tm^{3+} nanocrystals. *Mater Lett*. 2012;74:54–7.
23. Wang F, Wang J, Liu X. Direct evidence of a surface quenching effect on size-dependent luminescence of upconversion nanoparticles. *Angew Chemie - Int Ed*. 2010;49(41):7456–60.
24. Gao Y, Hu Y, Zhou D, Qiu J. Effect of crystalline fraction on upconversion luminescence in $\text{Er}^{3+}/\text{Yb}^{3+}$ Co-doped NaYF_4 oxyfluoride glass-ceramics. *J*

- Eur Ceram Soc. 2017;37(2):763–70.
25. Shen W, Yang Y, Li Z, Khan MI, Cao E, Zhou D, et al. Effect of melting temperature on the structure of self-crystallized Ba₂LaF₇ glass-ceramics. *J Non Cryst Solids*. 2019;523:119579(1-4).
 26. Chen D, Wan Z, Zhou Y, Huang P, Ji Z. Ce³⁺ dopants-induced spectral conversion from green to red in the Yb/Ho: NaLuF₄ self-crystallized nano glass-ceramics. *J Alloys Compd*. 2016;654:151–6.
 27. Cao J, Li X, Wang Z, Wei Y, Chen L, Guo H. Optical thermometry based on up-conversion luminescence behavior of self-crystallized K₃YF₆:Er³⁺ glass ceramics. Vol., *Sensors and Actuators, B: Chemical*. 2016;224:507–13.
 28. Fedorov PP, Luginina AA, Popov AI. Transparent oxyfluoride glass ceramics. *J Fluor Chem*. 2015;172:22–50.
 29. Zhao J, Ma R, Chen X, Kang B, Qiao X, Du J, et al. From Phase Separation to Nanocrystallization in Fluorosilicate Glasses: Structural Design of Highly Luminescent Glass-Ceramics. *J Phys Chem C*. 2016;120(31):17726–32.
 30. Fang Z, Chen Z, Peng W, Shao C, Zheng S, Hu L, et al. Phase-Separation Engineering of Glass for Drastic Enhancement of Upconversion Luminescence. *Adv Opt Mater*. 2019;7(8):1–8.
 31. Zhao J, Xu X, Chen X, Xu Q, Luo Z, Qiao X, et al. A structure model for phase separated fluoroaluminosilicate glass system by molecular dynamic simulations. *J Eur Ceram Soc*. 2019;39(15):5018–29.
 32. Zhao J, Xu X, Ren K, Luo Z, Qiao X, Du J, et al. Structural Origins of BaF₂/Ba_{1-x}RxF_{2+x}/RF₃ Nanocrystals Formation from Phase Separated Fluoroaluminosilicate Glass: A Molecular Dynamic Simulation Study. *Adv Theory Simulations*. 2019;2(10):1–11.
 33. O'Dell LA, Schurko RW. QCPMG using adiabatic pulses for faster acquisition of ultra-wideline NMR spectra. *Chem Phys Lett*. 2008;464(1–3):97–102.
 34. Zhao T, Hu L, Ren J. Fluorophosphate Upconversion-Luminescent Glass-Ceramics Containing Ba₂LaF₇:Er³⁺ Nanocrystals: An Advanced Solid-State Nuclear Magnetic Resonance Study. *J Phys Chem C*. 2021;125(48):26901–15.
 35. Wang R, Zhou D, Qiu J, Yang Y, Wang C. Color-tunable luminescence in

- Eu³⁺/Tb³⁺ co-doped oxyfluoride glass and transparent glass-ceramics. *J Alloys Compd.* 2015;629:310–4.
36. Fan X, Wang J, Qiao X, Wang M, Adam JL, Zhang X. Preparation process and upconversion luminescence of Er³⁺-doped glass ceramics containing Ba₂LaF₇ nanocrystals. *J Phys Chem B.* 2006;110(12):5950–4.
 37. Wang XF, Yan XH, Kan CX, Ma KL, Xiao Y, Xiao SG. Enhancement of blue emission in β -NaYbF₄:Tm³⁺/Nd³⁺ nanophosphors synthesized by nonclosed hydrothermal synthesis method. *Appl Phys B Lasers Opt.* 2010;101(3):623–9.
 38. Xu X, Wu Y, Bian W, Yu X, Zhang B, Li Q, et al. Improved near-infrared up-conversion emission of Tm³⁺ sensitized by Yb³⁺ and Ho³⁺ in LuF₃ nanocrystals. *J Nanosci Nanotechnol.* 2016;16(4):3664–8.
 39. Kang S, Huang Z, Lin W, Yang D, Zhao J, Qiao X, et al. Enhanced single-mode fiber laser emission by nano-crystallization of oxyfluoride glass-ceramic cores. *J Mater Chem C.* 2019;7(17):5155–62.
 40. Peng Y, Zhong J, Li X, Chen J, Zhao J, Qiao X, et al. Controllable competitive nanocrystallization of La³⁺-based fluorides in aluminosilicate glasses and optical spectroscopy. *J Eur Ceram Soc.* 2019;39(4):1420–7.
 41. Smedskjaer MM, Mauro JC, Sen S, Yue Y. Quantitative design of glassy materials using temperature-dependent constraint theory. *Chem Mater.* 2010;22(18):5358–65.
 42. Kiczenski TJ, Du LS, Stebbins JF. F-19 NMR study of the ordering of high field strength cations at fluoride sites in silicate and aluminosilicate glasses. *J Non Cryst Solids.* 2004;337(2):142–9.
 43. Muñoz F, De Pablos-Martín A, Hémono N, Pascual MJ, Durán A, Delevoye L, et al. NMR investigation of the crystallization mechanism of LaF₃ and NaLaF₄ phases in aluminosilicate glasses. *J Non Cryst Solids.* 2011;357(5):1463–8.
 44. Kiczenski TJ, Stebbins JF. Fluorine sites in calcium and barium oxyfluorides : F-19 NMR on crystalline model compounds and glasses. 2002;306:160–8.
 45. Zheng Q, Zhang Y, Montazerian M, Gulbitten O, Mauro JC, Zanutto ED, et al. Understanding Glass through Differential Scanning Calorimetry. *Chem Rev.* 2019;119(13):7848–939.

46. Li Z, Zhou D, Jensen LR, Qiu J, Zhang Y, Yue Y. Er³⁺-Yb³⁺ ions doped fluoro-aluminosilicate glass-ceramics as a temperature-sensing material. *J Am Ceram Soc.* 2021;104:4471–8.
47. Lusvardi G, Malavasi G, Cortada M, Menabue L, Menziani MC, Pedone A, et al. Elucidation of the structural role of fluorine in potentially bioactive glasses by experimental and computational investigation. *J Phys Chem B.* 2008;112(40):12730–9.
48. Swansbury LA, Mountjoy G, Chen X, Karpukhina N, Hill R. Modeling the Onset of Phase Separation in CaO-SiO₂-CaCl₂ Chlorine-Containing Silicate Glasses. *J Phys Chem B.* 2017;121(22):5647–53.
49. Du J. Molecular Dynamics Simulations of Disordered Materials. 2015;215:157–80.
50. Poulain M. Glass formation in ionic systems. *Nature.* 1981;293:279–80.
51. Środa M, Olejniczak Z. Effect of alkaline earth oxides on ceramization of LaF₃ in aluminosilicate glass: ¹⁹F MAS-NMR study. *J Non Cryst Solids.* 2011;357(7):1696–700.
52. Lin C, Li L, Bocker C, Rüssel C. Preparation and Structure of New Oxyfluoride Glass-Ceramics Containing BaLiF₃ Nanocrystal. *J Am Ceram Soc.* 2016;99(9):2878–81.
53. Park B, Li H, Corrales LR. Molecular dynamics simulation of La₂O₃-Na₂O-SiO₂ glasses. I. The structural role of La³⁺ cations. *J Non Cryst Solids.* 2002;297(2–3):220–38.
54. Berthier T, Fokin VM, Zanotto ED. New large grain, highly crystalline, transparent glass-ceramics. *J Non Cryst Solids.* 2008;354(15–16):1721–30.
55. Qiu J, Jiao Q, Zhou D, Yang Z. Recent progress on upconversion luminescence enhancement in rare-earth doped transparent glass-ceramics. *J Rare Earths.* 2016;34(4):341–67.
56. Shi Y, Yuan M, Li J, Li F, Cui W, Jiao X, et al. Upconversion Properties and Temperature-Sensing Behaviors of Alkaline-Earth-Metal Scandate Nanocrystals Doped with Er³⁺/Yb³⁺ Ions in the Presence of Alkali Ions (Li⁺, Na⁺, and K⁺). *Inorg Chem.* 2022;
57. Wang R, Liu J, Zhang Z. Luminescence and energy transfer progress in Bi-Yb co-doped germanate glass. *J Alloys Compd.* 2016;688:332–6.

58. Chen WP, Hu FF, Wei RF, Zeng QG, Chen LP, Guo H. Optical thermometry based on up-conversion luminescence of Tm^{3+} doped transparent Sr_2YF_7 glass ceramics. *J Lumin.* 2017;192(June):303–9.
59. Yue Y, Von der Ohe R, Jensen SL. Fictive temperature, cooling rate, and viscosity of glasses. *J Chem Phys.* 2004;120(17):8053–9.
60. Zhang J, Longley L, Liu H, Ashling CW, Chater PA, Beyer KA, et al. Structural evolution in a melt-quenched zeolitic imidazolate framework glass during heat-treatment. *Chem Commun.* 2019;55(17):2521–4.
61. Liu Q, Tian Y, Wang C, Huang F, Jing X, Zhang J, et al. Different dominant transitions in holmium and ytterbium codoped oxyfluoride glass and glass ceramics originating from varying phonon energy environments. *Phys Chem Chem Phys.* 2017;19(44):29833–9.
62. Chen D, Peng Y, Li X, Zhong J, Huang H, Chen J. Simultaneous Tailoring of Dual-Phase Fluoride Precipitation and Dopant Distribution in Glass to Control Upconverting Luminescence. *ACS Appl Mater Interfaces.* 2019;11(33):30053–64.
63. Aguiar H, Serra J, González P, León B. Structural study of sol-gel silicate glasses by IR and Raman spectroscopies. *J Non Cryst Solids.* 2009;355(8):475–80.
64. González P, Serra J, Liste S, Chiussi S, León B, Pérez-Amor M. Raman spectroscopic study of bioactive silica based glasses. *J Non Cryst Solids.* 2003;320(1–3):92–9.
65. Zhang X, Hu L, Ren J. Transparent Aluminosilicate Oxyfluoride Glass Ceramics Containing Upconversion Luminescent CaF_2 Nanocrystals: Glass-to-Crystal Structural Evolution Studied by the Advanced Solid-State NMR Spectroscopy. *J Phys Chem C.* 2020;124(2):1594–608.
66. Huang YY, Sarkar A, Schultz PC. Relationship between composition, density and refractive index for germania silica glasses. *J Non Cryst Solids.* 1978;27(1):29–37.
67. RITLAND HN. Relation Between Refractive Index and Density of a Glass at Constant Temperature. *J Am Ceram Soc.* 1955;38(2):86–8.
68. Sun T, Li Y, Ho WL, Zhu Q, Chen X, Jin L, et al. Integrating temporal and spatial control of electronic transitions for bright multiphoton upconversion. *Nat Commun.* 2019;10(1):1–7.

69. UVC lasing at 263 nm from Ba₂LaF₇ Yb³⁺,Tm³⁺ upconversion nanocrystals microcavities. *Opt Lett*. 2020;45(21):5986–9.
70. Ouyang T, Kang S, Zhang Z, Yang D, Huang X, Pan Q, et al. Microlaser Output from Rare-Earth Ion-Doped Nanocrystal-in-Glass Microcavities. *Adv Opt Mater*. 2019;7(21):1–7.
71. Masuno A, Inoue H, Yoshimoto K, Watanabe Y. Thermal and optical properties of La₂O₃-Nb₂O₅ high refractive index glasses. *Opt Mater Express*. 2014;4(4):710.
72. Herreros B, Manoli J, Fraissarda J. Solid-state ¹³⁹La NMR Investigation of Lanthanum-exchanged Y Zeolites. (464):464–6.
73. Zheng Q, Zhang Y, Montazerian M, Gulbitten O, Mauro JC, Zanotto ED, et al. Understanding Glass through Differential Scanning Calorimetry. *Chem Rev*. 2019;119(13):7848–7939.
74. Liu H, Qiao A, Gao Y, Tao H, Zhao X, Hu Y, et al. Reversible formation-melting of nano-crystals in supercooled oxyfluoride germanate liquids. *J Eur Ceram Soc*. 2019;39(16):5373–9.
75. Liu S, Kong Y, Tao H, Sang Y. Crystallization of a highly viscous multicomponent silicate glass: Rigidity percolation and evidence of structural heterogeneity. *J Eur Ceram Soc*. 2017;37(2):715–20.
76. Zhao J, Xu X, Li P, Li X, Chen D, Qiao X, et al. Structural Origins of RF₃/NaRF₄ Nanocrystal Precipitation from Phase-Separated SiO₂-Al₂O₃-RF₃-NaF Glasses: A Molecular Dynamics Simulation Study. *J Phys Chem B*. 2019;123(13):3024–32.
77. Li Z, Chen C, Shen W, Zhou D, Jensen LR, Qiao X, et al. Transformation from Translucent into Transparent Rare Earth Ions Doped Oxyfluoride Glass-Ceramics with Enhanced Luminescence. *Adv Opt mater*. 2022;DOI: 10.1002/adom.202102713
78. Astruc A, Célérier S, Pavon E, Mamede AS, Delevoye L, Brunet S. Mixed Ba_{1-x}La_xF_{2+x} fluoride materials as catalyst for the gas phase fluorination of 2-chloropyridine by HF. *Appl Catal B Environ*. 2017;204:107–18.
79. Cai J, Wei X, Hu F, Cao Z, Zhao L, Chen Y, et al. Up-conversion luminescence and optical thermometry properties of transparent glass ceramics containing CaF₂: Yb³⁺/Er³⁺ nanocrystals. *Ceram Int*. 2016;42:13990–5.

80. Li Z, Zhou D, Yang Y, Ren P, Zhu R, Han T, et al. Effects of crystal structure transformation on cooperative up-conversion luminescence in the Tb³⁺-Yb³⁺ co-doped oxyfluoride glass-ceramics. *J Alloys Compd.* 2018;731:1044–52.
81. Li X, Yuan S, Hu F, Lu S, Chen D, Yin M. Near-infrared to short-wavelength upconversion temperature sensing in transparent bulk glass ceramics containing hexagonal NaGdF₄: Yb³⁺/Ho³⁺ nanocrystals. *Opt Mater Express.* 2017;7(8):3023.
82. Gong HL, Peng XS, Ashraf GA, Hu FF, Wei RF, Guo H. Dual-mode optical thermometry based on transparent NaY₂F₇:Er³⁺,Yb³⁺ glass-ceramics. *Ceram Int.* 2022;48(3):4023–30.
83. Bao YN, Xu XS, Wu JL, Liu KC, Zhang ZY, Cao BS, et al. Thermal-induced local phase transfer on Ln³⁺-doped NaYF₄ nanoparticles in electrospun ZnO nanofibers: Enhanced upconversion luminescence for temperature sensing. *Ceram Int.* 2016;42(10):12525–30.
84. Min Q, Bian W, Qi Y, Lu W, Yu X, Xu X, et al. Temperature sensing based on the up-conversion emission of Tm³⁺ in a single KLuF₄ microcrystal. *J Alloys Compd.* 2017;728:1037–42.
85. Lv S, Shanmugavelu B, Wang Y, Mao Q, Zhao Y, Yu Y, et al. Transition Metal Doped Smart Glass with Pressure and Temperature Sensitive Luminescence. *Adv Opt Mater.* 2018;6(21):1–11.
86. Li X, Cao J, Wei Y, Yang Z, Guo H. Optical Thermometry Based on Up-Conversion Luminescence Behavior of Er³⁺ -Doped Transparent Sr₂YbF₇ Glass-Ceramics. *J Am Ceram Soc.* 2015;98(12):3824–30.
87. Jiang S, Zeng P, Liao L, Tian S, Guo H, Chen Y, et al. Optical thermometry based on upconverted luminescence in transparent glass ceramics containing NaYF₄:Yb³⁺/Er³⁺ nanocrystals. *J Alloys Compd.* 2014;617:538–41.
88. Vetrone F, Naccache R, Zamarrón A, De La Fuente AJ, Sanz-Rodríguez F, Maestro LM, et al. Temperature sensing using fluorescent nanothermometers. *ACS Nano.* 2010;4(6):3254–8.
89. Pandey A, Som S, Kumar V, Kumar V, Kumar K, Rai VK, et al. Enhanced upconversion and temperature sensing study of Er³⁺-Yb³⁺ codoped tungsten-tellurite glass. *Sensors Actuators, B Chem.* 2014;202:1305–12.
90. Li C, Dong B, Li S, Song C. Er³⁺-Yb³⁺ co-doped silicate glass for optical temperature sensor. *Chem Phys Lett.* 2007;443:426–9.

91. Lai B, Feng L, Wang J, Su Q. Optical transition and upconversion luminescence in Er^{3+} doped and Er^{3+} - Yb^{3+} co-doped fluorophosphate glasses. *Opt Mater.* 2010;32:1154–60.

LIST OF PUBLICATIONS

PUBLICATIONS IN PEER-REVIEW JOURNALS

Contributed as first author or main co-author:

- (1) **Li Z**, Zhou D, Jensen LR, Qiu J, Zhang Y, Yue Y. Er³⁺-Yb³⁺ ions doped fluoro-aluminosilicate glass-ceramics as a temperature-sensing material. *Journal of the American Ceramic Society*, 104, 4471-4478 (2021).
- (2) **Li Z**, Chen C, Shen W, Zhou D, Jensen LR, Qiao X, Ren J, Du J, Zhang Y, Qiu J, Yue Y. Transformation from Translucent into Transparent Rare Earth Ions Doped Oxyfluoride Glass-Ceramics with Enhanced Luminescence. *Advanced Optical Materials*, DOI: 10.1002/adom.202102713 (In press).
- (3) **Li Z**, Tan L, Chen C, Zhou D, Jensen LR, Ren J, Zhang Y, Qiu J, Yue Y. The impact of melting temperature on the properties of rare earth doped oxyfluoride glass/glass-ceramics. *Journal of the European Ceramic Society*, (submitted).
- (4) **Li Z**, Chen C, Zhou D, Jensen LR, Qiao X, Du J, Zhang Y, Ren J, Qiu J, Yue Y. Impact of network modifiers on the formation of rare earth ions doped melt-quenching derived oxyfluoride glass-ceramics (to be submitted).
- (5) **Li Z**, Zhang K, Zhou D, Jensen LR, Zhang Y, Ren J, Qiu J, & Yue Y. Impact of the LaF₃/YF₃ ratio on the properties of rare earth ions doped melt-quenching derived oxyfluoride glass-ceramics (in preparation).
- (6) Shen W, Yang Y, **Li Z**, Khan IM, Cao E, Zhou D, Qiu J. Effect of melting temperature on the structure of self-crystallized Ba₂LaF₇ glass-ceramics. *Journal of Non-Crystalline Solids*, 523, 1-4 (2019).
- (7) Shen W, Lai J, Yang Y, Zhou D, Qiu J, Khan IM, **Li Z**, Wang Qi, Zhang K. Effect of TiO₂ on glass structure control of self-crystallized Ba₂LaF₇ glass-ceramics. *Ceramics International*, 46, 114173-14177 (2020).
- (8) Zhang K, Zhou D, Qiu J, Wang Q, Lai J, Wang D, **Li Z**, Shen W. Effect of topological structure on photoluminescence of CsPbBr₃ quantum dot doped glasses. *Journal of Alloys and Compounds*, 826, 154111(2020).

ORIGINAL ARTICLE

Er³⁺-Yb³⁺ ions doped fluoro-aluminosilicate glass-ceramics as a temperature-sensing material

Zhencai Li^{1,2} | Dacheng Zhou² | Lars R. Jensen³ | Jianbei Qiu²  | Yanfei Zhang⁴  | Yuanzheng Yue^{1,4} 

¹Department of Chemistry and Bioscience, Aalborg University, Aalborg, Denmark

²School of Material Science and Engineering, Kunming University of Science and Technology, Kunming, China

³Department of Materials and Production, Aalborg University, Aalborg, Denmark

⁴School of Materials Science and Engineering, Qilu University of Technology (Shandong Academy of Sciences), Jinan, China

Correspondence

Yanfei Zhang, School of Materials Science and Engineering, Qilu University of Technology (Shandong Academy of Sciences), Jinan, China.
Email: zhang-yanfei@hotmail.com

Yuanzheng Yue, Department of Chemistry and Bioscience, Aalborg University, 9220 Aalborg, Denmark.
Email: yy@bio.aau.dk

Funding information

National Natural Science Foundation of China, Grant/Award Number: 12064021; China Scholarship Council, Grant/Award Number: 201808530502

Abstract

The transparent Er³⁺-Yb³⁺-doped fluoro-aluminosilicate glass-ceramic (GC) was prepared by melt-quenching. The crystal phase, morphology, and up-conversion (UC) luminescence of as-produced GC were characterized by X-ray diffraction, scanning electron microscopy, and fluorescence spectrophotometry, respectively. The results show that BaYF₅ nanocrystals were uniformly distributed in the glass matrix of the as-produced GC. When the as-produced GC was subjected to heat treatment, the crystallinity was increased, but the crystal identity remains unchanged. Such heat-treatment doubled the intensity of the UC luminescence, and this enhancement was ascribed to the increased incorporation of both Er³⁺ and Yb³⁺ ions into the lower phonon energy environment of BaYF₅ nanocrystals. Furthermore, the heat-treated GC was stable against further crystallization, and consequently its UC luminescence was stable at the application temperature. The heat-treated GC was found to possess an outstanding temperature-sensing capability.

KEYWORDS

erbium ion, fluoro-aluminosilicate glass-ceramics, temperature sensing, up-conversion luminescence

1 | INTRODUCTION

Temperature-dependent up-conversion (UC) luminescence materials doped with rare-earth (RE) ions have attracted a lot of attention owing to their various potential applications such as thermal imaging, cancer treatment, optical temperature sensors, optical refrigeration, and optical heater.¹⁻⁴ Among all the applications, the noncontact optical temperature sensing is of particular interest for two reasons. First, such materials exhibit superior sensing performances including high accuracy, high spatial resolution, and fast response. Second, they can be applied in some

special occasions, where the traditional contact methods for detecting temperature cannot be used, for example, building fire detections, electrical transformer temperature in power stations, nanoscopic temperature measurement, and biological imaging systems.^{5,6} Precise measurement of temperature is important in many industrial and scientific applications. For optical temperature sensors, the temperature can be determined based on the fluorescence intensity ratio (FIR) between the thermally coupled energy levels (TCELs) of RE ions. The FIR technique possesses high reliability, improved sensitivity, and wide operating temperature range compared to some other optical-based techniques, for

example, fluorescence lifetime and amplified spontaneous emissions.^{7,8}

In the case of the FIR method of the optical temperature sensor, to obtain a sufficient electron population from the upper energy level of TCELs to its lower energy level, the energy differences of TCELs should usually be controlled between 200 and 2000 cm^{-1} . Several trivalent RE ions such as Ho^{3+} ($^5\text{F}_1/^5\text{G}_6$, $^3\text{F}_{2,3}/^3\text{K}_8$), Er^{3+} ($^2\text{H}_{11/2}$ and $^4\text{S}_{3/2}$), Tm^{3+} ($^3\text{F}_{2,3}$ and $^3\text{H}_4$, $^1\text{G}_{4(a)}$ and $^1\text{G}_{4(b)}$), and Dy^{3+} ($^4\text{I}_{15/2}$ and $^4\text{F}_{9/2}$) can meet the requirement of the above TCELs differences.⁹ These ions have been extensively explored as active centers for noncontact temperature sensing. Among these RE ions, Er^{3+} ion was regarded as a favorable probe in temperature sensing due to its energy level structure that possesses the applicable energy differences ($\Delta E \sim 700 \text{ cm}^{-1}$) of TCELs. In addition to the active centers, the host materials of optical temperature sensors also play a crucial role in obtaining good stability, high UC luminescence, and excellent temperature sensing performance. Many previous studies focused on Er^{3+} -doped fluoride nanocrystals and oxide glasses as optical temperature sensors.¹⁰ Although the fluoride nanocrystals exhibit efficient UC luminescence and higher temperature sensitivity owing to their low phonon energy and large energy gap (ΔE), their chemical stability is poor. Instead, Er^{3+} -doped oxide glasses show excellent optical transparency, considerable chemical, and thermal stability. Although Er^{3+} -doped oxide glasses have some advantages, they could not be applied in optical temperature sensors due to their high phonon energy. To solve the above-mentioned problems, scientists attempt to develop alternative materials, for example, oxyfluoride glass-ceramics (GCs).^{11,12} These GCs have exhibited great potential to be applied as optical temperature sensors since their thermal and chemical stabilities are better than the fluoride nanocrystals, and their optical properties are superior to oxide glasses.

Oxyfluoride GCs are often prepared by melt-quenching followed by subsequent heat treatment. The heat treatment conditions such as the temperature and time are crucial to the nucleation and growth processes, as well as to the diffusion coefficient of Er^{3+} ions into the crystallites. The optical transmittance of GCs decreases with heat treatment temperature since the light scattering increases with the growth of crystallites.^{13,14} However, it is a challenge to precisely control the crystal size within nanoscale and to promote insertion of Er^{3+} ions into nanocrystals and thereby to improve UC luminescent performance. This is why we put effort into the investigation of the nanocrystals-containing GCs.¹⁵

In this work, we prepared a novel Er^{3+} - Yb^{3+} codoped glass-ceramic (GC) containing BaYF_5 nanocrystals by the melt-quenching method. Then, we determined the thermodynamic, structural, and luminescent properties of both as-produced GC and heat-treated GC. We clarified the influence of heat treatment on the morphology of nanocrystals in the

GC samples. Finally, we achieved the accurate temperature-sensing function of Er^{3+} - Yb^{3+} codoped heat-treated GC through the optical thermometry based on the FIR of the green UC luminescence.

2 | EXPERIMENTAL PROCEDURE

The as-produced GC with the molar composition of 45SiO_2 - $15\text{Al}_2\text{O}_3$ - $12\text{Na}_2\text{O}$ - 21BaF_2 - 7YF_3 - 0.5ErF_3 - 1YbF_3 was prepared by the melt-quenching technique. About 10 g raw materials (SiO_2 , Al_2O_3 , Na_2O , BaF_2 , YF_3 , ErF_3 , and YbF_3) was uniformly mixed and melted in a covered alumina crucible in air at 1723 K for 45 min. Then the melt was cast onto a preheated stainless steel plate. After that, the glass samples were immediately transferred to an annealing furnace at 673 K for 8 h and cooled slowly to room temperature to eliminate thermal stress. The as-produced GC sample was subjected to heat treatment at 913 K for 2 h to obtain the heat-treated GC sample.

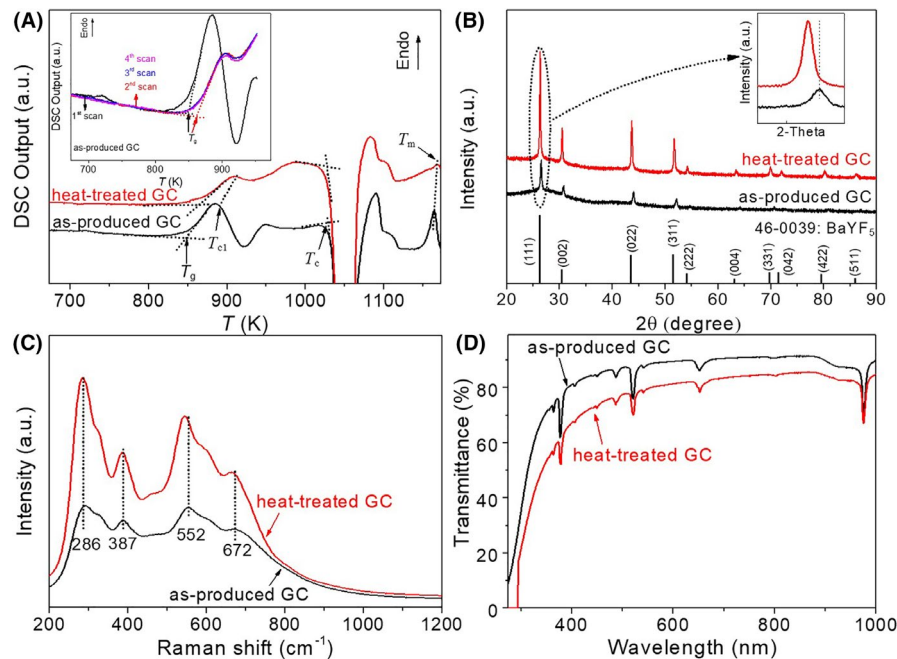
To determine the enthalpic responses to glass transition and phase transitions, and their characteristic temperatures, both as-produced GC and heat-treated GC samples were up-scanned in the differential scanning calorimeter (DSC, STA-449F3) to 1173 K at 10 K/min in nitrogen. X-ray diffraction (XRD) measurements were performed to identify the crystallization phases by a powder diffractometer operated at 40 KV and 40 mA, using $\text{CuK}\alpha$ as the radiation. The 2θ scan range was 20° - 90° with a step size of 0.02° . The XRD data were subjected to the Rietveld refinement of the structure using the software TOPAS to verify the crystal structure and to determine the purity of the crystals (Supporting Information). The Raman spectra were acquired by a micro-Raman spectrometer (inVia, Renishaw) from 200 to 1200 cm^{-1} excited by a 532 nm green HeNe laser for 10 s. The morphology of the samples was analyzed by field-emission scanning electron microscopy (SEM, QUANTA 200) and transmission electron microscope (TEM, JEM-2100) equipped with the selected area electron diffraction (SAED) at a voltage of 30 and 200 KV, respectively. The optical absorption spectra in the wavelength range 275-1000 nm were measured on a Varian Cary 50 spectrophotometer. The UC emission spectra in the wavelength range from 500 to 700 nm were recorded with a HITACHI F-7000 fluorescence spectrophotometer under the 980 nm laser excitation.

3 | RESULTS AND DISCUSSION

3.1 | Phase transitions and crystal identity

Figure 1A shows the comparison of DSC curves of both the as-produced GC and the heat-treated GC samples.

FIGURE 1 (A) Differential scanning calorimetry (DSC) upscan curves of as-produced GC and heat-treated GC. Inset: DSC upscan curves of as-produced GC for repeated four times at the same heating and cooling rate of 10 K/min to 953 K. (B) XRD patterns of as-produced GC and heat-treated GC. Bars represent cubic BaYF₅ crystal data (PDF#46-0039). Inset: the magnified XRD diffraction peaks located at about 26.3°. (C) Raman spectra of as-produced GC and heat-treated GC. (D) Transmittance spectra of as-produced GC and heat-treated GC [Color figure can be viewed at wileyonlinelibrary.com]



The glass transition temperature (T_g) of as-produced GC is determined to be 847 K. With the increasing upscan temperature, the first crystallization peak with the onset temperature (T_{c1}) of about 893 K occurs, which nearly overlaps with the glass transition peak. This indicates that the as-produced GC is unstable toward crystallization. With further increasing the upscan temperature, another sharp and intense crystallization peak occurs at about 1026 K, followed by the melting temperature of about 1165 K. In contrast, the heat-treated GC exhibits an increased T_g (863 K) and T_{c1} (911 K), indicating a stronger network structure and a higher crystallinity than the as-produced GC. The increase in T_g and T_{c1} can be ascribed to the fact that F, Y, and Ba can diffuse from the oxide glass matrix to the new nucleus and the existing nanocrystals during heat treatment, and thus, the concentration of network-forming ions (Si⁴⁺ and Al³⁺) in the glass matrix increases. To study the thermal stability of as-produced GC, the sample was scanned four times at the same heating and cooling rate of 10 K/min to 953 K, as shown in the inset of Figure 1B. It can be seen that the T_g and T_{c1} increases to 862 and 908 K, respectively, after the first scan. The two values remain constant in the following two scans, indicating the increased thermal stability of heat-treated GC. The high thermal stability of heat-treated GC is beneficial to the application of optical thermometry sensors.

The XRD patterns of as-produced GC and heat-treated GC are presented in Figure 1B. Diffraction peaks appear in the XRD pattern of as-produced GC, which are assigned to the cubic BaYF₅ crystals (JCPDS NO. 46-0039). This indicates that self-crystallization takes place during the melt-quenching process.¹⁶ Upon heat treatment, the diffraction peaks of heat-treated GC become more intense and sharper, implying the

formation of more BaYF₅ crystals. To determine both the nanocrystal structure and the purity of the cubic BaYF₅ nanocrystals, we have performed the XRD Rietveld refinement of the heat-treated GC (Supporting Information). The results indicate that the cubic BaYF₅ nanocrystals are pure. The diffraction peaks of heat-treated GC shift to smaller angle slightly compared with those of as-produced GC (the inset of Figure 1B), confirming the substitution of both Er³⁺ ions (0.089 nm) and Yb³⁺ ions (0.099 nm) for Y³⁺ ions (0.09 nm) in the BaYF₅ crystals. The crystal size of BaYF₅ crystals can be estimated by the following Scherrer equation⁵:

$$D = \frac{K\lambda}{\beta \cos \theta} \quad (1)$$

where K is the Scherrer constant (0.89), λ is the wavelength of the incident XRD (for CuK α , $\lambda = 0.154056$ nm), θ is the Bragg angle of X-ray diffraction peak, and β is the corrected half-width of diffraction peak. The grain size of the BaYF₅ crystal in the heat-treated GC sample is calculated to be approximately 60 nm, suggesting that the formed crystals are within nanoscale.

Figure 1C illustrates the Raman spectra of both the as-produced GC and the heat-treated GC samples, which are excited by a 532 nm laser. The Raman spectra of as-produced GC consist of a sharp and enhanced Raman peak at around 293 cm⁻¹, which is ascribed to the BaYF₅ nanocrystals.¹⁷ This further confirms that the nanocrystals can form during the quenching process. Upon heat treatment, the peak of the heat-treated GC shifts to a smaller wavenumber region (286 cm⁻¹) and matches well with the BaYF₅ nanocrystal, and this shift might be attributed to the substitution of more Er³⁺ ions for Y³⁺ ions.¹⁸ Those peaks at 387, 552, and 672 cm⁻¹ can be assigned to the Si(Al)–O–Si(Al) symmetric stretching

and bending modes with inter-tetrahedral vibrations, respectively.¹⁹ In addition, both the narrower full width at half maximum (FWHM) and higher peak intensity at 286 cm^{-1} corresponding to the BaYF_5 nanocrystal implies the higher crystallinity of heat-treated GC than as-produced GC. The transmittance spectra in the range from 275 to 1000 nm of the as-produced GC and the heat-treated GC samples are given in Figure 1D. The characteristic absorption peaks located at about 378, 487, 523, 541, 653, and 976 nm are attributed to the transitions from the ground state $^4\text{I}_{15/2}$ to the excited states $^4\text{G}_{11/2}$, $^4\text{F}_{7/2}$, $^2\text{H}_{11/2}$, $^4\text{S}_{3/2}$, $^4\text{F}_{9/2}$, and $^2\text{F}_{5/2}$ (Yb^{3+} ions) transitions of Er^{3+} ions, respectively.²⁰ It can be observed that both the as-produced GC and the heat-treated GC samples present high transmittance ($>80\%$). This is because the precipitated BaYF_5 nanocrystals are much smaller than the wavelength of visible light, and hence, the light scattering becomes lower.

SEM micrographs of as-produced GC and heat-treated GC are shown in Figure 2A,B. In Figure 2A, some spherical nanocrystals (about 25 nm) (see light domains) are uniformly distributed in the glass matrix, while the nanocrystals grow to around 65 nm upon heat treatment (Figure 2B), and this size is comparable to the diameter estimated by Scherrer equation. In addition to the $\sim 65\text{ nm}$ crystals, the new spherical BaYF_5 nanocrystals (about 10 nm) precipitate in the residual glass matrix, being consistent with the crystal size reported elsewhere.^{16,18}

Figure 2C,D shows the TEM and high-resolution TEM (HRTEM) images of the heat-treated GC sample containing BaYF_5 nanocrystals. The TEM images illustrate that the nanocrystals (dark domains) are randomly distributed in the glass matrix with clear boundaries, in accordance with the SEM results. The polycrystalline feature of heat-treated GC is confirmed by the SAED patterns (inset of Figure 2C). In addition, the HRTEM image and its fast Fourier transform (FFT) pattern (inset of Figure 2D) exhibit a well-defined lattice structure with an interplanar spacing of 0.339 nm, which could be attributed to the (111) lattice planes of cubic BaYF_5 nanocrystal.¹⁶

3.2 | UC luminescent behaviors

Figure 3A shows the UC luminescence spectra in the wavelength range from 500 to 700 nm of the $\text{Er}^{3+}\text{-Yb}^{3+}$ codoped as-produced GC and heat-treated GC excited by 980 nm laser. The characteristic UC luminescence peaks at 523, 541, and 653 nm are attributed to the transitions from the $^2\text{H}_{11/2}$, $^4\text{S}_{3/2}$, and $^4\text{F}_{9/2}$ excited states to the $^4\text{I}_{15/2}$ ground state of Er^{3+} ions, respectively. It is noticeable that both as-produced GC and heat-treated GC show pronounced stark splitting and the UC luminescence intensity of heat-treated GC is greatly enhanced by two times compared with as-produced GC. This

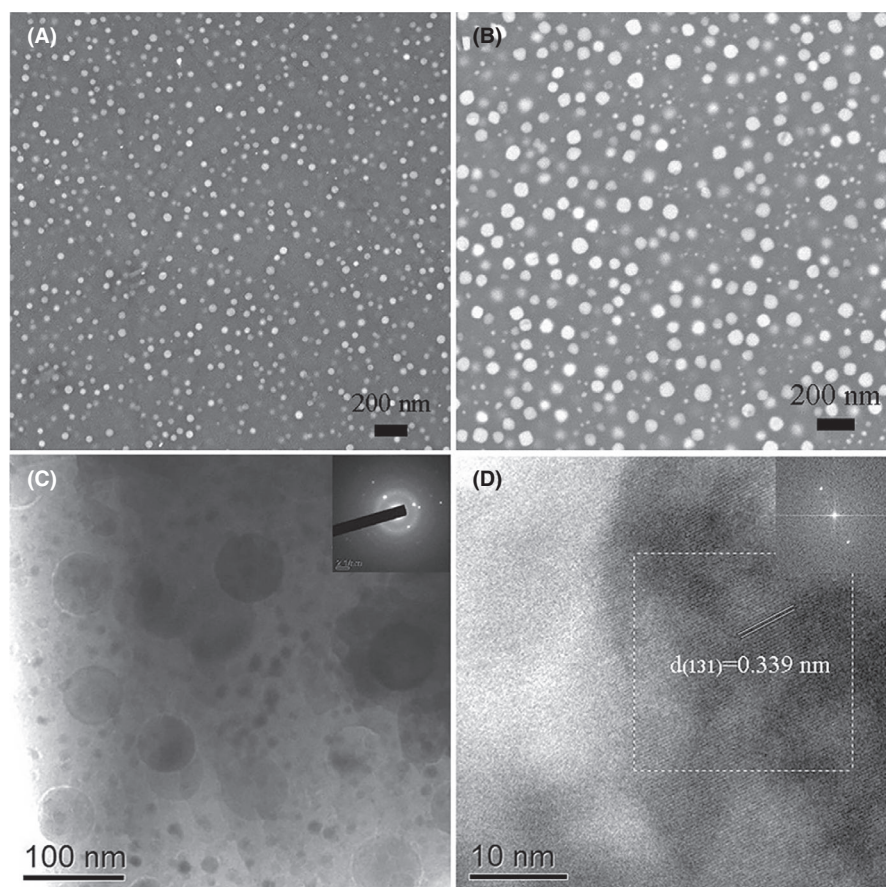


FIGURE 2 SEM micrographs of as-produced GC (A) and heat-treated GC (B). (C and D) Low-resolution and high-resolution TEM micrographs of heat-treated GC. Insets: selected area electron-diffraction (SAED) image of TEM micrographs (C) and fast Fourier transform (FFT) image of the square dash line region of TEM micrographs (D)

FIGURE 3 (A) UC luminescence spectra of the as-produced GC and the heat-treated GC samples. (B) Dependence of UC luminescence intensity on pump power for the heat-treated GC sample. (C) The possible mechanism for both UC emission and energy-transfer processes of Er^{3+} - Yb^{3+} codoped in as-produced GC and heat-treated GC under the 980 nm diode laser excitation [Color figure can be viewed at wileyonlinelibrary.com]

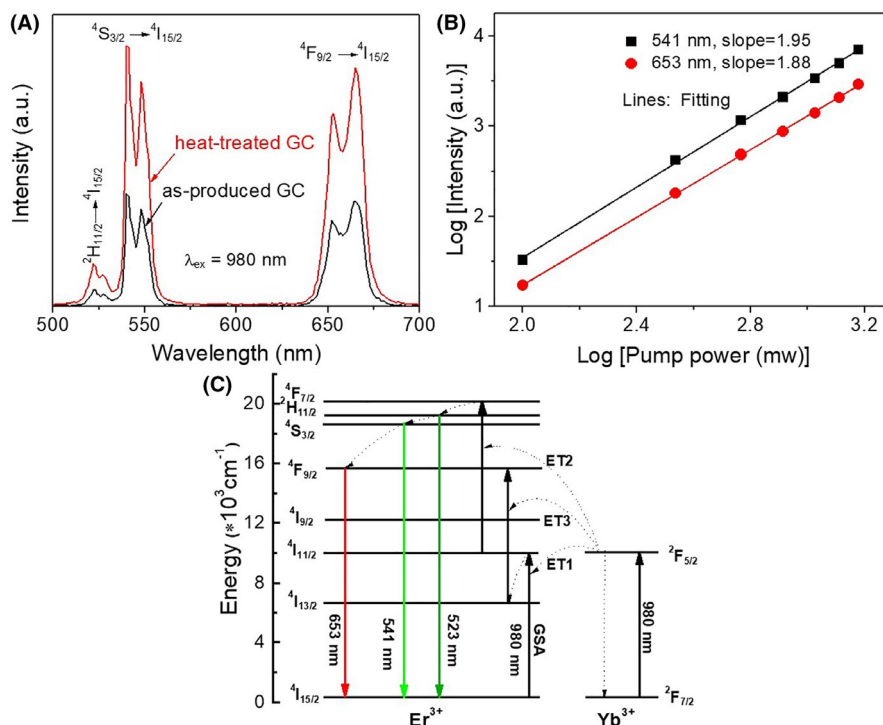
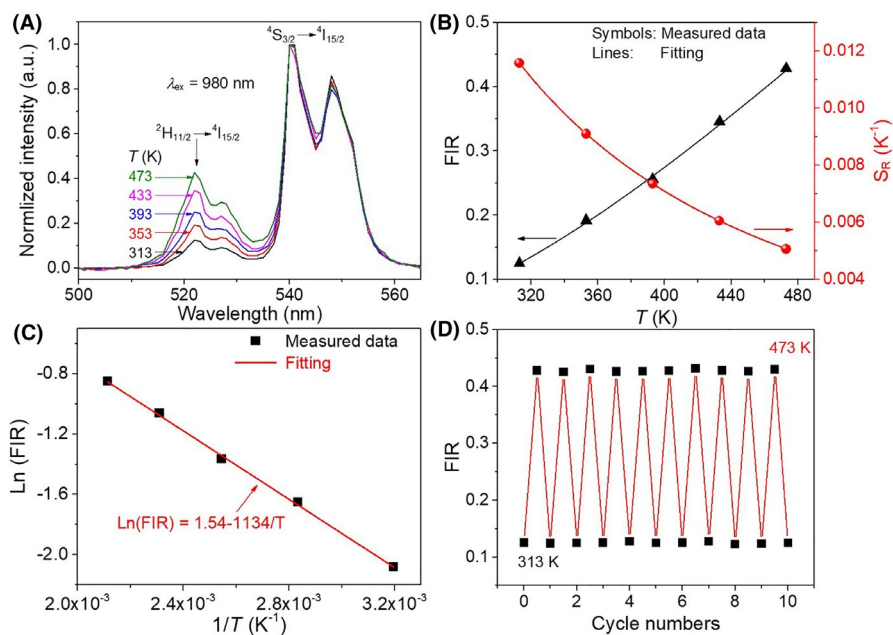


FIGURE 4 (A) Normalized UC luminescence spectra of heat-treated GC under the excitation of the 980 nm diode laser at various temperatures from 313 to 473 K. (B) Black fitting curve: Temperature dependence of FIR between $^2\text{H}_{11/2} \rightarrow ^4\text{I}_{15/2}$ and $^4\text{S}_{3/2} \rightarrow ^4\text{I}_{15/2}$ transitions of Er^{3+} of heat-treated GC. Red fitting curve: The sensitivity S_R of heat-treated GC. (C) Logarithmic plot of the FIR as a function of inverse absolute temperature. (D) Temperature-induced switching of FIR of heat-treated GC (alternating between 313 and 473 K) [Color figure can be viewed at wileyonlinelibrary.com]



enhancement is ascribed to the fact that the incorporation of Er^{3+} ions into the low phonon energy environment of BaYF_5 nanocrystals can reduce the probability of nonradiative relaxation.²¹ In general, the UC emission intensity (I_{UC}) and pumping power (P) of 980 nm laser are correlated by the expression $I_{\text{UC}} \sim P^n$, where n is the photon number needed to pump Er^{3+} ions from the ground state to the excited state, that is, the number of photons required for achieving the up-conversion transition. The logarithmic plots of pumping power-dependent UC emission intensity are presented in Figure 3B. The linear-fitted slopes are 1.95 and 1.88 at 541 nm ($^4\text{S}_{3/2} \rightarrow ^4\text{I}_{15/2}$) and 653 nm ($^4\text{F}_{9/2} \rightarrow ^4\text{I}_{15/2}$), respectively, for

heat-treated GC, indicating that the two-photon process dominates the strong UC luminescence.

Figure 3C describes the energy level scheme of Er^{3+} and Yb^{3+} codoped as-produced GC and heat-treated GC, which implies a UC mechanism. Excited by 980 nm laser, the electrons of Yb^{3+} ions at the ground state of $^2\text{F}_{7/2}$ are first populated to the excited state of $^2\text{F}_{5/2}$ by ground-state absorption (GSA). Then, the excited Yb^{3+} ions nonradiatively relax from $^2\text{F}_{5/2}$ to $^2\text{F}_{7/2}$ level, and this process releases the energy to drive adjacent Er^{3+} ions from $^4\text{I}_{15/2}$ ground state to $^4\text{I}_{11/2}$ excited state. The entire energy transfer can be described as ET1 process: $^4\text{I}_{15/2}(\text{Er}^{3+}) + 2^2\text{F}_{5/2}(\text{Yb}^{3+}) \rightarrow 4^4\text{I}_{11/2}$

Sensing materials	Temperature range (K)	ΔE (cm ⁻¹)	S_R (% K ⁻¹)	Ref.
BaYF ₅ : Er ³⁺ , Yb ³⁺ heat-treated GC	313–473	787	1134/T ²	This work
Mn ²⁺ :ZnGa ₂ O ₄ NG	323–523	-	2.51	25
Sr ₂ YbF ₇ : Er ³⁺ GC	300–500	786	1129.8/T ²	24
NaYF ₄ : Er ³⁺ , Yb ³⁺ GC	298–693	774	1117.4/T ²	26
NaYF ₄ : Er ³⁺ , Yb ³⁺ phosphors	290–320	715	1028/T ²	3
TeO ₂ -WO ₃ : Er ³⁺ , Yb ³⁺ glasses	300–690	679	976.8/T ²	27
silicate glass: Er ³⁺ , Yb ³⁺	296–723	413	593/T ²	28
Fluorophosphate glass: Er ³⁺ , Yb ³⁺	77–500	390	559/T ²	29

TABLE 1 ΔE and S_R of several typical FIR-based optical temperature sensors based on UC luminescence from ²H_{11/2} and ⁴S_{3/2} levels of Er³⁺ ions

(Er³⁺) + 2F_{7/2} (Yb³⁺). Moreover, the 4f electrons of Er³⁺ ions at ⁴I_{15/2} level can be directly excited to ⁴I_{11/2} through the GSA without the aid of the energy from ²F_{5/2} level of Yb³⁺ ions. Subsequently, Er³⁺ ions at ⁴I_{11/2} level are driven to ⁴F_{7/2} level by ET2 process: ⁴I_{11/2} (Er³⁺) + 2F_{5/2} (Yb³⁺) → 4F_{7/2} (Er³⁺) + 2F_{7/2} (Yb³⁺). Afterward, Er³⁺ ions at ⁴F_{7/2} level nonradiatively relax to ²H_{11/2} and ⁴S_{3/2} emitting levels and further radiatively relax down to ⁴I_{15/2} ground state to cause emissions at 523 and 541 nm, respectively. For the red emission (⁴F_{9/2} → ⁴I_{15/2}) at 653 nm, ⁴F_{9/2} emitting level can be pumped by two ways: (1) nonradiative relaxation from ⁴S_{3/2} level; (2) ET3 process (⁴I_{13/2} (Er³⁺) + 2F_{5/2} (Yb³⁺) → 4F_{9/2} (Er³⁺) + 2F_{7/2} (Yb³⁺)) after the nonradiative relaxation from ⁴I_{11/2} level.²²

3.3 | UC luminescence for temperature sensing

The potential for the studied heat-treated GC to be applied in optical temperature sensor has been assessed based on the green UC luminescence spectra in a broad temperature range 313–473 K. The intensity of the spectra should be normalized by that of the peak at 541 nm in order to quantify the impact of temperature variation on the intensity of the characteristic peak at 523 nm (Figure 4A). In Figure 4A, it is obvious that the intensity ratio between the 523 nm peak (²H_{11/2} → ⁴I_{15/2} transition) and the 541 nm peak (⁴S_{2/13} → ⁴I_{15/2} transition) increases monotonously with temperature, resulting from the temperature dependence of the distribution of Er³⁺ ions between ²H_{11/2} and ⁴S_{3/2} levels.

According to the Boltzmann distribution theory, the fluorescence intensity ratio (FIR) between ²H_{11/2} and ⁴S_{3/2} levels for Er³⁺ ions is related to the absolute temperature (T) as follows:

$$\text{FIR} = \frac{I_H}{I_S} = Ce^{-\frac{\Delta E}{k_B T}} \quad (2)$$

where I_H and I_S are the intensities for the luminescence from the upper (²H_{11/2}) and lower (⁴S_{3/2}) levels, respectively, ΔE is the effective energy gap between ²H_{11/2} and ⁴S_{3/2} levels, C is a temperature-independent constant, and k_B is the Boltzmann constant.²¹ The black fitting curve in Figure 4B represents the temperature dependence of the FIR between ²H_{11/2} → ⁴I_{15/2} and ⁴S_{3/2} → ⁴I_{15/2} transitions for Er³⁺ ions in heat-treated GC. The experimental relation between Ln (FIR) and the inverse absolute temperature ($1/T$) is depicted in Figure 4C. This relation can be fitted by the following equation²³:

$$\text{Ln}(\text{FIR}) = 1.54 - 1134 \frac{1}{T} \quad (3)$$

The slope ($\Delta E/k_B$) is determined to be −1134, and thus the ΔE is 787 cm⁻¹, being close to ΔE (812 cm⁻¹) calculated from the transmittance spectra. The relative temperature sensitivity (S_R) is an important parameter reflecting the rate of change in FIR in response to the variation in temperature, which can be expressed by the following equation²⁴:

$$S_R = \left| \frac{1}{\text{FIR}} \frac{d(\text{FIR})}{dT} \right| = \frac{\Delta E}{k_B T^2} \quad (4)$$

As shown in Figure 4B, the dependence of the S_R value of the heat-treated GC sample on temperature can be determined to be 1134/T² by fitting the experimental data to Eq. (4). The comparison in S_R between the present heat-treated GC sample and other materials is shown in Table 1. The S_R value of the heat-treated GC is larger than those of other materials listed in Table 1. Specifically, the S_R values are in the range of 0.51–1.15% K⁻¹, corresponding to the temperature range from 473 to 313 K. To test the thermal stability of the UC luminescence, the heat-treated GC sample is subjected to 10 heating-cooling cycles between 473 and 313 K. The FIR of UC luminescence intensity at 523 and 541 nm recovers to its original state when the heat-treated GC sample is cooled from 473 to 313 K. As

displayed in Figure 4D, the temperature-dependent UC luminescent behavior is reversible during cycling processes. This reversibility could be attributed to the protecting role of the oxide glass matrix. Thus, the transparent heat-treated GC containing BaYF₅ nanocrystals could be used in optical temperature sensors with excellent thermal stability.

4 | CONCLUSIONS

The Er³⁺-Yb³⁺ codoped as-produced GC containing spontaneously crystallized BaYF₅ nanocrystals was prepared by the melt-quenching method. The nanoparticles with an average size of about 25 nm were uniformly distributed in the glass matrix. The nanocrystals with a size of about 65 nm were generated in as-produced GC by performing heat-treatment at 913 K for 2 hours, and Er³⁺ ions entered into the BaYF₅ crystals, and thereby enhancing the UC luminescence intensity. In addition, the application potential of heat-treated GC in optical thermometry was proved by determining the FIR of green UC luminescence from Er³⁺. The maximum relative temperature sensitivity (S_R) was found to be 1.15% K⁻¹ at 313 K, which was higher than those of the Er³⁺-doped glasses and GCs reported previously.

ACKNOWLEDGMENTS

This work was supported by the China scholarship council (CSC, No. 201808530502), the National Natural Science Foundation of China (No. 12064021), and Shandong Province (ZR2020ME025), the Taishan Youth Scholar Project of Shandong Province (tsqn202103098).

ORCID

Jianbei Qiu  <https://orcid.org/0000-0002-3699-3310>

Yanfei Zhang  <https://orcid.org/0000-0001-7811-6597>

Yuanzheng Yue  <https://orcid.org/0000-0002-6048-5236>

REFERENCES

- Chen WP, Hu FF, Wei RF, Zeng QG, Chen LP, Guo H. Optical thermometry based on up-conversion luminescence of Tm³⁺ doped transparent Sr₂YF₇ glass ceramics. *J Lumin*. 2017;192:303–9.
- Zhong JS, Chen DQ, Peng YZ, Lu YD, Chen X, Li XY, et al. A review on nanostructured glass ceramics for promising application in optical thermometry. *J Alloy Compd*. 2018;763:34–48.
- Vetrone F, Naccache R, Zamarrón A, De La Fuente AJ, Sanz-Rodríguez F, Maestro LM, et al. Temperature sensing using fluorescent nanothermometers. *ACS Nano*. 2010;4:3254–8.
- Cao JK, Li XM, Wang ZX, Wei YL, Chen LP, Guo H. Optical thermometry based on up-conversion luminescence behavior of self-crystallized K₃YF₆: Er³⁺ glass ceramics. *Sensor Actuat B-Chem*. 2016;224:507–13.
- Cao JK, Chen LP, Chen WP, Xu DK, Sun XY, Guo H. Enhanced emissions in self-crystallized oxyfluoride scintillating glass ceramics containing KTb₂F₇ nanocrystals. *Opt Mater Express*. 2016;6:2201–6.
- Yang X, Zhang MY, Ma HQ, Xu XH, Yu X. Self-crystallized Ba₂LaF₇ glass ceramics with high thermal-stability for white light-emitting-diodes and field emission displays. *ECS J Solid State Sci Technol*. 2019;8:127–32.
- Chen DQ, Wan ZY, Zhou Y. Dual-phase nano-glass-ceramics for optical thermometry. *Sensor Actuat B-Chem*. 2016;226:14–23.
- Li XY, Yuan S, Hu FF, Lu SQ, Chen DQ, Yin M. Near-infrared to short-wavelength upconversion temperature sensing in transparent bulk glass ceramics containing hexagonal NaGdF₄: Yb³⁺/Ho³⁺ nanocrystals. *Opt Mater Express*. 2017;7:3023–33.
- Chen DQ, Wan ZY, Zhou Y, Huang P, Zhong JS, Ding MY, et al. Bulk glass ceramics containing Yb³⁺/Er³⁺: β-NaGdF₄ nanocrystals: phase-separation-controlled crystallization, optical spectroscopy and upconverted temperature sensing behavior. *J Alloy Compd*. 2015;638:21–8.
- Cai JJ, Wei XT, Hu FF, Cao ZM, Zhao L, Chen YH, et al. Up-conversion luminescence and optical thermometry properties of transparent glass ceramics containing CaF₂: Yb³⁺/Er³⁺ nanocrystals. *Ceram Int*. 2016;42:13990–5.
- Liu XF, Zhou JJ, Zhou SF, Yue YZ, Qiu JR. Transparent glass-ceramics functionalized by dispersed crystals. *Prog Mater Sci*. 2018;97:38–96.
- Zhou SF, Jiang N, Zhu B, Yang HC, Ye S, Lakshminarayana G, et al. Multifunctional bismuth-doped nanoporous silica glass: from blue-green, orange, red, and white light sources to ultra-broadband infrared amplifiers. *Adv Funct Mater*. 2008;18:1407–13.
- Chen Z, Lai SN, Zhang H, Jia H, Wang T, Chen QQ, et al. Nonlinear negative transmittance at a CW 980-nm laser diodes pumping in Yb³⁺: CaF₂ nanocrystals-embedded glass ceramics. *J Am Ceram Soc*. 2017;100:612–9.
- Fang ZJ, Chen Z, Peng WC, Shao CY, Zheng SP, Hu LL, et al. Phase-separation engineering of glass for drastic enhancement of upconversion luminescence. *Adv Opt Mater*. 2019;7:1801572.
- Zhao ZM, Hu FF, Cao ZM, Chi FF, Wei XT, Chen YH, et al. Self-crystallized Ba₂LaF₇: Nd³⁺/Eu³⁺ glass ceramics for optical thermometry. *Ceram Int*. 2017;43:14951–5.
- Vetrone F, Mahalingam V, Capobianco JA. Near-infrared-to-blue upconversion in colloidal BaYF₅: Tm³⁺, Yb³⁺ nanocrystals. *Chem Mater*. 2009;21:1847–51.
- Fan XP, Wang J, Qiao XS, Wang MQ, Adam JL, Zhang XH. Preparation process and upconversion luminescence of Er³⁺-doped glass ceramics containing Ba₂LaF₇ nanocrystals. *J Phys Chem B*. 2006;110:5950–4.
- Huang SM, Gao QC, Gu M. Enhanced luminescence in transparent glass ceramics containing BaYF₅: Ce³⁺ nanocrystals. *J Lumin*. 2012;132:750–4.
- Kang SL, Huang ZP, Lin W, Yang DD, Zhao JJ, Qiao XS, et al. Enhanced single-mode fiber laser emission by nanocrystallization of oxyfluoride glass-ceramic cores. *J Mater Chem C*. 2019;7:5155–62.
- Dan HK, Zhou DC, Wang RF, Jiao Q, Yang ZW, Song ZG, et al. Effect of Mn²⁺ ions on the enhancement red upconversion emission of Mn²⁺/Er³⁺/Yb³⁺ tri-doped in transparent glass-ceramics. *Opt Laser Technol*. 2014;64:264–8.
- Min QH, Bian WJ, Qi YS, Lu W, Yu X, Xu XH, et al. Temperature sensing based on the up-conversion emission of Tm³⁺ in a single KLuF₄ microcrystal. *J Alloy Compd*. 2017;728:1037–42.
- Zhu CF, Chausseid S, Liu SJ, Zhang YF, Monteil A, Gaumer N, et al. Composition dependence of luminescence of Eu and Eu/Tb doped silicate glasses for LED applications. *J Alloy Compd*. 2013;555:232–6.

23. Suo H, Guo CF, Yang Z, Zhou SS, Duan CK, Yin M. Thermometric and optical heating bi-functional properties of up-conversion phosphor $\text{Ba}_5\text{Gd}_8\text{Zn}_4\text{O}_{21}$: $\text{Yb}^{3+}/\text{Tm}^{3+}$. *J Mater Chem C*. 2015;3:7379–85.
24. Li XM, Cao JK, Wei YL, Yang ZR, Guo H. Optical Thermometry Based on Up-Conversion Luminescence Behavior of Er^{3+} -Doped Transparent Sr_2YbF_7 Glass-Ceramics. *J Am Ceram Soc*. 2015;98:3824–30.
25. Lv SC, Shanmugavel B, Wang YP, Mao QN, Zhao YJ, Yu YZ, et al. Transition metal doped smart glass with pressure and temperature sensitive luminescence. *Adv Opt Mater*. 2018;21:1800881.
26. Sha J, Zeng P, Liao LQ, Tian SF, Guo H, Chen YH, et al. Optical thermometry based on upconverted luminescence in transparent glass ceramics containing NaYF_4 : $\text{Yb}^{3+}/\text{Er}^{3+}$ nanocrystals. *J Alloy Compd*. 2014;617:538–41.
27. Pandey A, Som S, Kumar V, Kumar V, Kumar K, Rai VK, et al. Enhanced upconversion and temperature sensing study of Er^{3+} - Yb^{3+} codoped tungsten-tellurite glass. *Sensor Actuat B-Chem*. 2014;202:1305–12.
28. Li CR, Dong B, Li SF, Song CL. Er^{3+} - Yb^{3+} co-doped silicate glass for optical temperature sensor. *Chem Phys Lett*. 2007;443:426–9.
29. Lai BY, Li F, Wang J, Su Q. Optical transition and upconversion luminescence in Er^{3+} doped and Er^{3+} - Yb^{3+} co-doped fluorophosphate glasses. *Opt Mater*. 2010;32:1154–60.

SUPPORTING INFORMATION

Additional supporting information may be found online in the Supporting Information section.

How to cite this article: Li Z, Zhou D, Jensen LR, Qiu J, Zhang Y, Yue Y. Er^{3+} - Yb^{3+} ions doped fluoro-aluminosilicate glass-ceramics as a temperature-sensing material. *J Am Ceram Soc*. 2021;104: 4471–4478. <https://doi.org/10.1111/jace.17867>

Supplemental Materials

Er³⁺-Yb³⁺ ions doped fluoro-aluminosilicate glass-ceramics as a temperature-sensing material

Zhencai Li^{1,2}, Dacheng Zhou², Lars R. Jensen³, Jianbei Qiu², Yanfei Zhang^{4,*}, Yuanzheng Yue^{1,4,*}

¹Department of Chemistry and Bioscience, Aalborg University, 9220 Aalborg, Denmark

²School of Material Science and Engineering, Kunming University of Science and Technology, Kunming 650093, China

³Department of Materials and Production, Aalborg University, 9220 Aalborg, Denmark

⁴School of Materials Science and Engineering, Qilu University of Technology (Shandong Academy of Sciences), Jinan 250353, China

To determine both the nanocrystal structure and the purity of the cubic BaYF₅ nanocrystals, the XRD Rietveld refinement of the heat-treated GC was performed using TOPAS software. The difference between the observed and calculated plots was shown in Figure S1. The cubic BaYF₅ nanocrystal structure and equivalent isotropic parameters are given in Table S1.

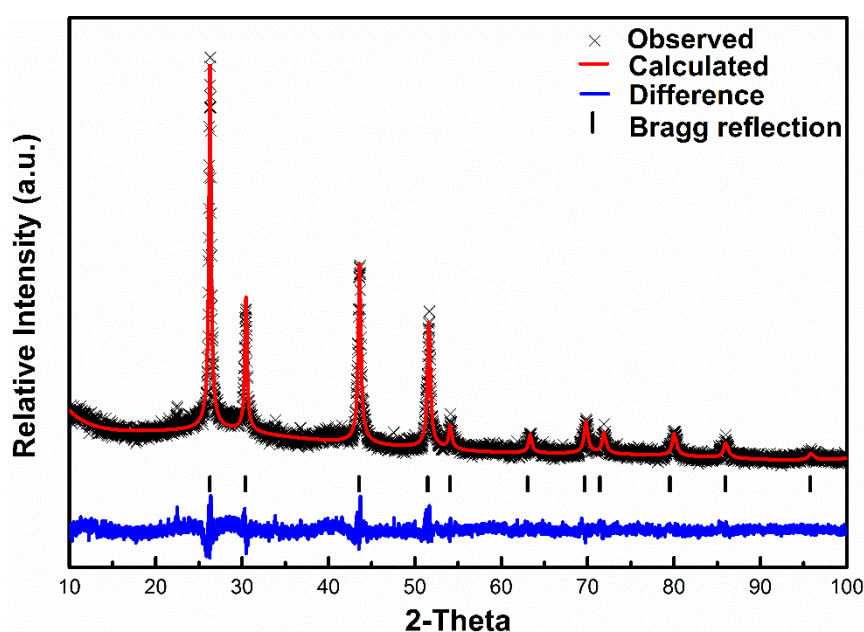


FIGURE S1. Rietveld refinement patterns of the BaYF₅ nanocrystals. x: the observed raw X-ray diffraction data; Red line: the calculated pattern; Black vertical lines: the Bragg peak positions of the allowed reflections for Cu K α_1 and K α_2 . Blue curve: the difference between the observed and calculated intensities on the same scale.

TABLE S1 Details of the BaYF₅ Crystal Structure and Equivalent Isotropic Parameters

Structure		Cubic			
Space group		Fm-3m (225)			
Lattice parameters		$a = b = c = 5.874 \text{ \AA}$, $\alpha = \beta = \gamma = 90^\circ$			
Z		2			
Volume of unit cell		202.63 \AA^3			
Atom	Wyckoff positions	x	y	z	Occupancy
Ba	4a	0	0	0	0.5
Y	4a	0	0	0	0.5
F1	8c	0.25	0.25	0.25	0.5572
F2	48i	0.5	0.1913	0.1913	0.0999
F3	32f	0.4485	0.4485	0.4485	0.0127
F4	4b	0.5	0.5	0.5	0.0218

Transformation from Translucent into Transparent Rare Earth Ions Doped Oxyfluoride Glass-Ceramics with Enhanced Luminescence

*Zhencai Li, Chunying Chen, Weihui Shen, Dacheng Zhou, Lars R. Jensen, Xvsheng Qiao, Jinjun Ren,
Jincheng Du, Yanfei Zhang, Jianbei Qiu, * Yuanzheng Yue**

Z. C. Li, Prof. Y. Z. Yue

Department of Chemistry and Bioscience, Aalborg University, DK-9220 Aalborg, Denmark

E-mail: yy@bio.aau.dk

C. Y. Chen, Dr. J. J. Ren

Shanghai Institute of Optics and Fine Mechanics, Chinese Academy of Sciences, Shanghai 201800, China

W. H. Shen, D. C. Zhou, Prof. J. B. Qiu

School of Material Science and Engineering Kunming University of Science and Technology, Kunming
650093, China

E-mail: qiu@kmust.edu.cn

Dr. L. R. Jensen

Department of Materials and Production, Aalborg University, DK-9220 Aalborg, Denmark

Dr. X. S. Qiao

School of Materials Science and Engineering, Zhejiang University, Hangzhou 310027, China

Prof. J. C. Du

Department of Materials Science and Engineering, University of North Texas, Denton, Texas 76203, U.S

Prof. Y. F. Zhang

School of Materials Science and Engineering, Qilu University of Technology, Jinan 250353, China

Keywords: translucent and transparent glass-ceramic, crystallization, phase separation, refractive index; up-conversion luminescence

Abstract

It is known that the optical transparency of an oxide glass decreases with an increase of the size and fraction of crystals in the glass during heat-treatment (HT). Here we report an opposite scenario, where a translucent Er^{3+} - Yb^{3+} doped oxyfluoride glass-ceramic (GC) becomes transparent with increasing crystal size and crystallinity. Specifically, in the heat-treated GC samples, we observed that the growth of the existing Ba_2LaF_7 crystals and particularly the formation of small spherical Ba_2LaF_7 crystals greatly enhanced the light transmittance. To reveal the origin of this anomalous phenomenon, we performed detailed morphology and structure analyses on both the precursor and the heat-treated samples and Molecular Dynamics (MD) simulations of the precursor glass. The results show that the composition of the residual glass phase was altered (e.g., depletion of La^{3+}) in the way that the differences in refractive index between the glass matrix and the crystals are greatly reduced. As a consequence, the light scattering of the heat-treated GC was suppressed, and hence, the derived GC became transparent. In addition, a proper HT can also enhance the luminescence of the studied GC system.

1. Introduction

Traditional oxyfluoride glass-ceramics (GCs) are a kind of multiphase material that contain fluoride crystallites embedded in the oxide glass matrix.^[1-2] This material bears the advantages of both the fluoride crystallites and the oxide glass matrix.^[3] The crystallites have low phonon energy environment, while the oxide glass matrix possesses both high optical transparency and excellent chemical and thermal stabilities, which are crucial for protecting the fluoride crystallites from reacting with the moisture from the environment. For the oxyfluoride GCs doped with rare earth (RE) ions, the RE ions, which serve as the up-conversion (UC) luminescence centers, preferentially enter the fluoride crystallites, and hence, reduce the rate of non-radiative relaxation, and thereby benefiting the UC luminescence.^[4] Thus, oxyfluoride GCs are a promising candidate for optical applications such as optical amplifiers,^[5] multicolor displays,^[6] UC fibers,^[7] lasers,^[8] and optical thermometry.^[9] However, it is a challenge to achieve the oxyfluoride GCs with both high transparency and superior UC luminescence.

Usually, the optical transmittance of the oxyfluoride GCs is lower than that of their corresponding precursor glass since the former has stronger optical absorption and light scattering than the latter. According to the Rayleigh-Gans theory,^[10] if crystallinity is low (e.g., <40 vol% and the average size of the fluoride crystallites is well below the wavelength of the incident light, the light scattering in the visible range will be low. If the average size of fluoride crystallites is less than 30 nm, most of the oxyfluoride GCs would exhibit ultrahigh transparency owing to less light scattering and absorption.^[11] But on the other hand, if the fluoride crystallites are too small, they will not accommodate a large amount of RE ions required to achieve high UC luminescence efficiency.^[12-14] Therefore, it is important to find a way to realize both high transparency and superior UC luminescence efficiency in the same material. To do so, it is necessary to tailor the chemical composition and size of crystallites in the oxide glass matrix.

By altering the concentration of glass modifiers in the chemical composition, we have found several translucent oxyfluoride GCs obtained via quenching glass melts, which contain large ($>100\ \mu\text{m}$) fluoride crystals. In addition, the strategy of isothermal heat-treatment (HT) can be used to adjust the refractive index (n) of the glass matrix to match that of the fluoride crystals, thereby increasing the transparency of the translucent samples by minimizing the n difference (<0.01) between the fluoride crystallites and the glass matrix. In this work, we investigate one of the above-mentioned translucent oxyfluoride GCs, i.e., $45\text{SiO}_2\text{-}15\text{Al}_2\text{O}_3\text{-}12\text{Na}_2\text{O-}21\text{BaF}_2\text{-}7\text{LaF}_3\text{-}0.5\text{ErF}_3\text{-}1.0\text{YbF}_3$, to demonstrate the translucency-to-transparency transformation caused by a proper HT process.

To determine the structure, size and fraction of the crystals in the oxyfluoride GCs, we performed high-resolution transmission electron microscopy (HRTEM), scanning electron microscopy (SEM) and X-ray diffraction (XRD). To study both the crystal formation and the glass transition of the GCs, we conducted differential scanning calorimetry (DSC) and XRD. In the end, we achieved the match of the refractive index of the glass matrix with that of the crystal phase, and thereby the high transparency of the oxyfluoride GC. The origin of the heat-treatment enhancement of transparency of the oxyfluoride GC was clarified by the solid-state nuclear magnetic resonance (NMR) and the Raman spectroscopy, as well as the molecular dynamics (MD) simulation. Furthermore, the optimized HT condition resulted in superior luminescence efficiency.

2. Results and Discussion

2.1. Optical, thermal and structural analyses

Figure 1a shows the optical transmittance of both P-GC and three heat-treated P-GC samples, which are derived from their absorption spectra in the wavelength range of 275 to 800 nm (Figure S2a).^[14] It is seen that the transmittance increases with the heat-treatment (HT) temperature. The trend can also be reflected by the optical images of P-GC and the three P-GC samples heat-treated

at 600, 640, and 680 °C (from left to right, respectively) for 4 h (Inset of Figure 1a). The increase of the transmittance can be clarified as follows. First, the average size of the Ba₂LaF₇ nanocrystals decreases with the increasing HT temperature. If it is controlled within 30 nm, the light scattering in grain boundaries can be avoided. Second, for large-sized crystals (e.g., up to micrometer scale), both light scattering and absorption can be attenuated by only minimizing the refractive index difference (<0.01) between crystals and glass matrix.^[15]

Figure 1b shows the DSC curves of both the P-GC and the three P-GC samples that were heat-treated at 600, 640 and 680 °C for 4 h, respectively. It is seen that P-GC undergoes glass transition with the onset temperature (T_g) and the two crystallization processes with the onset temperatures of T_{c1} and T_{c2} , respectively, and finally the melting with the offset temperature of T_m . The values of T_g , T_{c1} , T_{c2} and T_m are determined to be 559, 607, 792 and 871 °C, respectively, by the method described elsewhere.^[16] It is observed in Figure 1b and Table. S1 that T_g and T_{c1} first increase with both the HT temperature and duration, and then remain unchanged. The maximum T_g and T_{c1} values indicate that the crystallinity has reached the maximum at a sufficiently high extent of HT. In other words, the composition of the glass matrix phase does not vary with further HT, i.e., the glass structure does not change.^[17] The onset temperature of the main crystallization peak (T_{c2}) of P-GC decreases from 792 to 782 °C upon HT at 600 °C for 4 h, and then remains unchanged with further increasing HT temperature. However, the T_m value remains constant with increasing HT temperature. To determine the stability of the glass network structure against crystallization, P-GC samples were subjected to 4 cycles of DSC scans up to the maximum scanning temperatures ($T_{scan-max}$) of 580, 600, 620, 640, and 660 °C, respectively, at 10 °C/min. In Figure S2b and Table. S2, it is seen that T_g first sharply increases and then gradually approaches the highest value with repeating the DSC scans. This implies that the glass network connectivity increases with DSC scans, and reaches a maximum, due to the cease of crystallization.^[18] To study the first crystallization event of

both P-GC and the heat-treated samples, the crystallization enthalpy (ΔH) of each sample was calculated by integrating the exothermic peak (Figure 1b). It is evident that ΔH gradually decreases with increasing HT temperature, implying that the crystallization already takes place during HT. This means that P-GC has a strong tendency to crystallization before the main crystallization occurs around 800 °C (Figure 1b).^[19]

Figure 1c shows the XRD patterns of both P-GC and three heat-treated P-GC samples. The diffraction peaks of P-GC are identified to be the face-centered cubic (FCC) Ba_2LaF_7 crystal (PDF#48-0099), suggesting that a certain amount of crystals have already formed during melt-quenching.^[20] The intensities of the diffraction peaks increase with HT temperature and no new diffraction peaks appears. To determine the purity of the cubic Ba_2LaF_7 crystals, the XRD Rietveld refinement of the P-GC sample heat-treated at 640 °C for 4 h was performed using TOPAS software. The difference between the observed and calculated plots is shown in Figure S3. The cubic Ba_2LaF_7 nanocrystal structure and equivalent isotropic parameters are given in Table S3. It is seen that there is an excellent match between the observed and the calculated plots, suggesting that only the Ba_2LaF_7 crystals are present in the studied samples. From the XRD results, the crystallinity is found to increase from 42 to 64% with increasing the HT temperature up to 680 °C for 4 h (Table. S4). This implies that HT leads to the formation of Ba_2LaF_7 crystals in P-GC.

Figure 1d illustrates the Raman spectra acquired using the 532 nm laser and subsequently normalized by the intensity of the peak at 550 cm^{-1} for both P-GC and the heat-treated samples. The mid-frequency bands at 350-700 cm^{-1} are associated with the Si-O-Si (Al) symmetric stretching vibration mode in the glass matrix.^[22-23] Specifically, the peak at 418 cm^{-1} is assigned to a symmetric ring-breathing mode (five-fold ring structure) involving mainly oxygen motion, whereas the peaks at 550, and 610 cm^{-1} are attributed to the symmetric stretch of three-fold ring structures, respectively.^[24-25] Strikingly, a sharp peak in the low-frequency region appears at around 269 cm^{-1}

for P-GC, which is ascribed to the vibration of the Ba-F and La-F bonds in Ba_2LaF_7 crystals.^[25] This confirms that Ba_2LaF_7 crystals have already formed in the precursor glass during melt-quenching compared with the traditional oxyfluoride glasses (Figure S4a). Furthermore, the normalized intensity of the peak at 269 cm^{-1} increases with the HT temperature. Other peaks at 386, 416, 550, 616, and 689 cm^{-1} , which are associated with tetrahedral units in glass matrix, become weaker with the HT temperature, verifying an increase of the crystallinity in the studied samples upon HT.

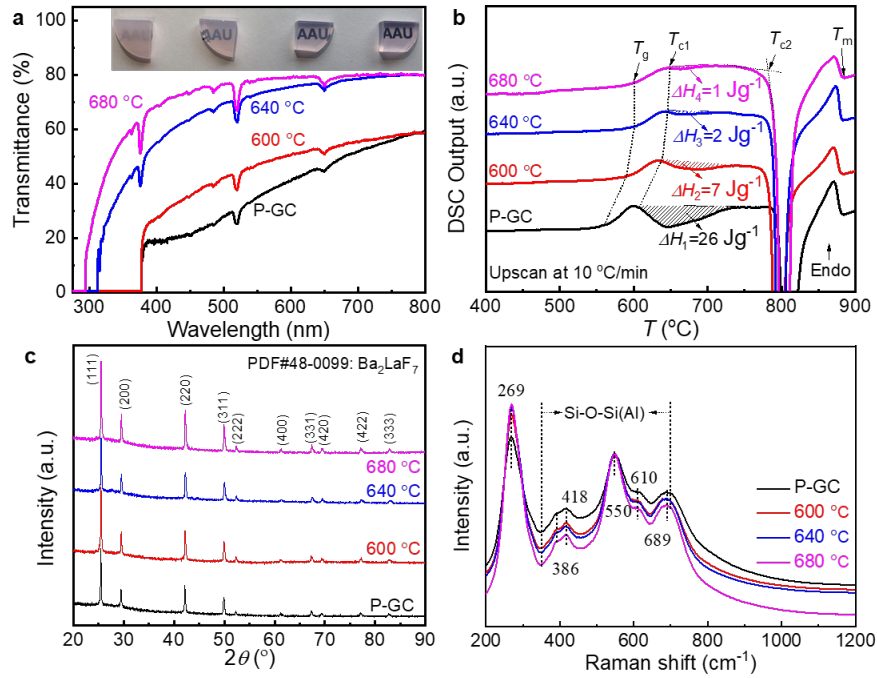


Figure 1. Impact of HT on optical and structural characteristics of precursor glass-ceramic (P-GC). (a) Transmittance of P-GC before and after HT at 600, 640, and 680 °C for 4 h. Inset: Photos of P-GC sample and P-GC samples heat-treated at 600, 640, and 680 °C for 4 h, respectively (from left to right). (b) DSC output (arbitrary unit) of P-GC and the heat-treated samples. The glass transition temperatures (T_g), the onset temperatures of both the first and second crystallization peaks (T_{c1} and T_{c2} , respectively) and the offset temperature of the melting peak, i.e., the melting point (T_m) (see the arrows). Hatched area: crystallization enthalpy. (c) XRD patterns. (d) Normalized Raman spectra, where the vibrational modes and the peak positions are indicated.

2.2. Evolution of crystals and its structural origin

Figures 2a-d show the SEM images of both P-GC and the heat-treated samples. For P-GC, there are three distinct regions: white flower-like, white, and black domains (Figure 2a), which

correspond to Ba_2LaF_7 crystals, fluoride-rich glass matrix, and silica-rich glass matrix, respectively. The silica-rich glass matrix contains $[\text{SiO}_4]$ and $[\text{AlO}_4]$ tetrahedral units. However, La^{3+} ions can be regarded as the network intermediate.^[26] Therefore, a few La^{3+} ions might enter the silica-rich network, forming $[\text{Si}(\text{La})\text{O}_4]$ tetrahedral units. Both $[\text{SiO}_4]$ and $[\text{AlO}_4]$ domains in the surface layer were etched by HF acid, so that the contrast between the fluoride-rich phases (see the white domains in Figure 2a) and the remaining silica-rich phases (see black domains) can be seen.^[27] Flower-like Ba_2LaF_7 crystals (180~190 nm) are distributed in the fluoride-rich phases. Ba_2LaF_7 crystals grow to about 220 nm and the tiny spherical Ba_2LaF_7 nanocrystals (about 5 nm) precipitate from the fluoride-rich phase upon HT at 600 °C for 4 h (Figure 2b). This implies that the formation of the fluoride-rich phase assists the growth of the existing crystals and the formation of Ba_2LaF_7 nanocrystals. Upon HT at 640 °C for 4 h, both the flower-like crystals and the nanocrystals grow to about 260 nm and 15 nm, respectively (Figure 2c). At 680 °C for 4 h, two types of Ba_2LaF_7 crystals further grow to 300 nm and 25 nm, respectively (Figure 2d). This indicates an increase of both the crystallinity and the average size of the flower-like Ba_2LaF_7 crystals with increasing HT temperature.

Molecular dynamics (MD) simulation is conducted to reveal the glass structural features of P-GC composition, which is then compared with the experimentally detected ones. Under rapid cooling condition of MD simulations, the simulated glass structure shows the regions of aluminosilicate-rich phase and fluoride-rich phase (Figure 2e), and this is a clear signature of phase separation.^[28] The high tendency of phase separation leads to the occurrence of the spontaneous crystallization in the P-GC composition during cooling under the current experimental condition. In addition, the fluoride-rich region detected by MD simulations has a chemical composition similar to that of the fluoride crystals found by EDS. As shown in Figure 2e, the oxide-rich phase is composed of a network structure with $[\text{SiO}_4]$ and $[\text{AlO}_4]$ tetrahedral units linked through corner-sharing of

bridging oxygen. In comparison, the fluoride-rich phase is rich in modifier cations, such as Na^+ , Ba^{2+} and La^{3+} , with coordination numbers of >4 . The structure of the fluoride-rich phase can be described by a polyhedral random packing model or be interpreted by Poulain's ionic glass model (Figure 2f).^[26-27] Al^{3+} , Na^+ , Ba^{2+} , and La^{3+} ions are preferentially distributed at the interface between oxide- and fluoride-rich phases and these cations not only act as network modifiers in the silicate phase but also connect the non-bridging $\text{O}_{1/2}^-$ and ionic F^- of fluoride phase.

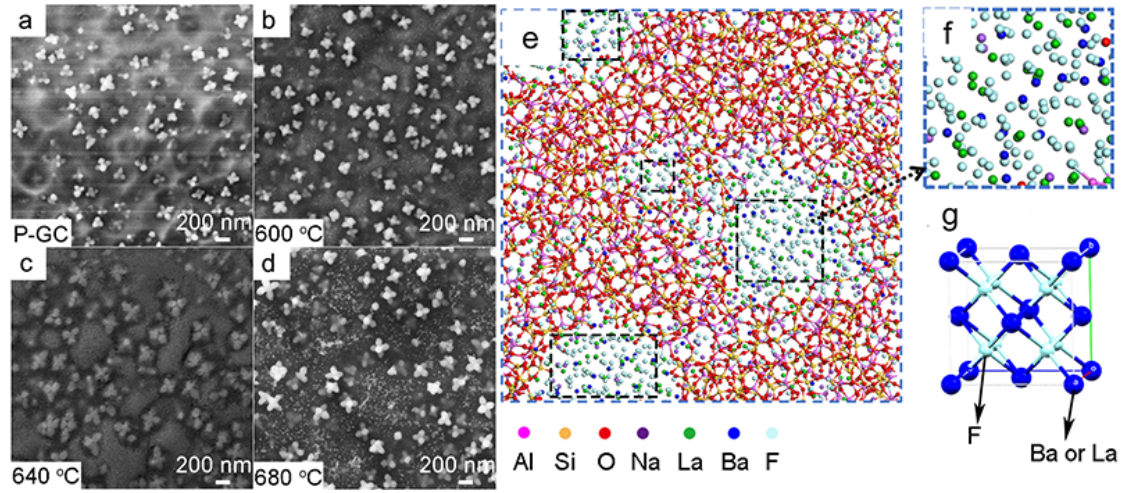


Figure 2. Revealing the structural origin of the crystal evolution by Scanning electron microscope (SEM) and Molecular dynamics (MD) simulation. a-d: The evolution of crystals with HT temperature; e-g: MD simulated structure of P-GC system. (a) P-GC; (b-d) the three P-GC samples heat-treated at 600, 640, 680 °C for 4 h, respectively. (e) MD simulated structure of P-GC composed of network-forming SiO_4 and AlO_4 tetrahedra and network modifiers. Note that Er^{3+} and Yb^{3+} are replaced by La^{3+} to perform MD simulations. (f) A signified structural domain taken from Figure e, which is enriched in network modifying ions and F^- ions. (g) Cubic lattice structure of a Ba_2LaF_7 crystallite.

2.3. Observation of crystal evolution at different length scales

Figure 3 shows the micrographs obtained by the aberration-corrected transmission electron microscopy (ACTEM) and high-resolution Transmission Electron Microscopy (HRTEM) for both P-GC and the heat-treated samples. For P-GC (image A in the first row of Figure 3), flower-like Ba_2LaF_7 crystals (about 190 nm) precipitate from the glass matrix. HRTEM image B (taken from the red dotted circle in image A) shows the crystal lattice fringes with the spacings of 0.345 nm and 0.295 nm that are indexed as the (111) and (220) plane of Ba_2LaF_7 crystals, respectively. The

SAED photograph (image C) reveals that Ba_2LaF_7 are single crystals. The HRTEM image D (taken from the black dotted box in image A) implies the amorphous nature of the matrix phase. This means that flower-like Ba_2LaF_7 crystals are distributed in the glass matrix of the P-GC sample.

Upon HT at 600 °C, the Ba_2LaF_7 crystals grow to approximately 220 nm (image A in the second row of Figure 3). It is seen that some spherical Ba_2LaF_7 crystals of about 6 nm are uniformly precipitated from the glass matrix. HRTEM image B is obtained from the black-dashed circle of image A. The interplanar distances between the adjacent fringes are determined to be 0.349 nm and 0.301 nm, which match with the (111) and (200) planes of Ba_2LaF_7 crystals, respectively. SAED photograph C confirms that the flower-like Ba_2LaF_7 are indeed single crystals. The inset in image D indicates that the spherical domains, whose lattice fringes lie in the (111) plane with d -spacing of 0.350 nm, are Ba_2LaF_7 single nanocrystals.

Upon HT at 640 °C (the third row of Figure 3), both flower-like and spherical Ba_2LaF_7 crystals (image A) further grow to the average sizes of about 260 nm and 15 nm, respectively. Obviously, two kinds of crystals are separately precipitated in the glass matrix. Most of the spherical Ba_2LaF_7 crystals are populated in some regions, in which they are well separated. These Ba_2LaF_7 crystals grow through the migration of Ba^{2+} , La^{3+} , and F^- ions to the nucleation sites. Thus, the composition of the glass matrix (see the regions around the flower-like crystals) is changed by the depletion of the network modifying ions such as Ba^{2+} and La^{3+} , and consequently, the network connectivity of the glass matrix increases. The SAED pattern in image C confirms that the Ba_2LaF_7 crystals are still single crystals after HT. In addition, the HRTEM micrograph (image B) shows a well-defined lattice structure with the interplanar spacings of 0.347 nm and 0.297 nm in the (111) and (200) planes of Ba_2LaF_7 crystals, respectively.

Upon HT at 680 °C, both the flower-like and the spherical Ba_2LaF_7 crystals grow to about 300 nm and 25 nm, respectively (see image A in the fourth row of Figure 3). Their crystal lattice

spacings were measured to be 0.35 and 0.305 nm (image B) in the (111) and (200) planes of Ba_2LaF_7 single crystals (image C), respectively. It is inferred that Ba^{2+} and La^{3+} ions are arranged in an ordered manner, being a typical feature of a single crystal. Image D shows the tiny nanocrystals further grow upon HT.

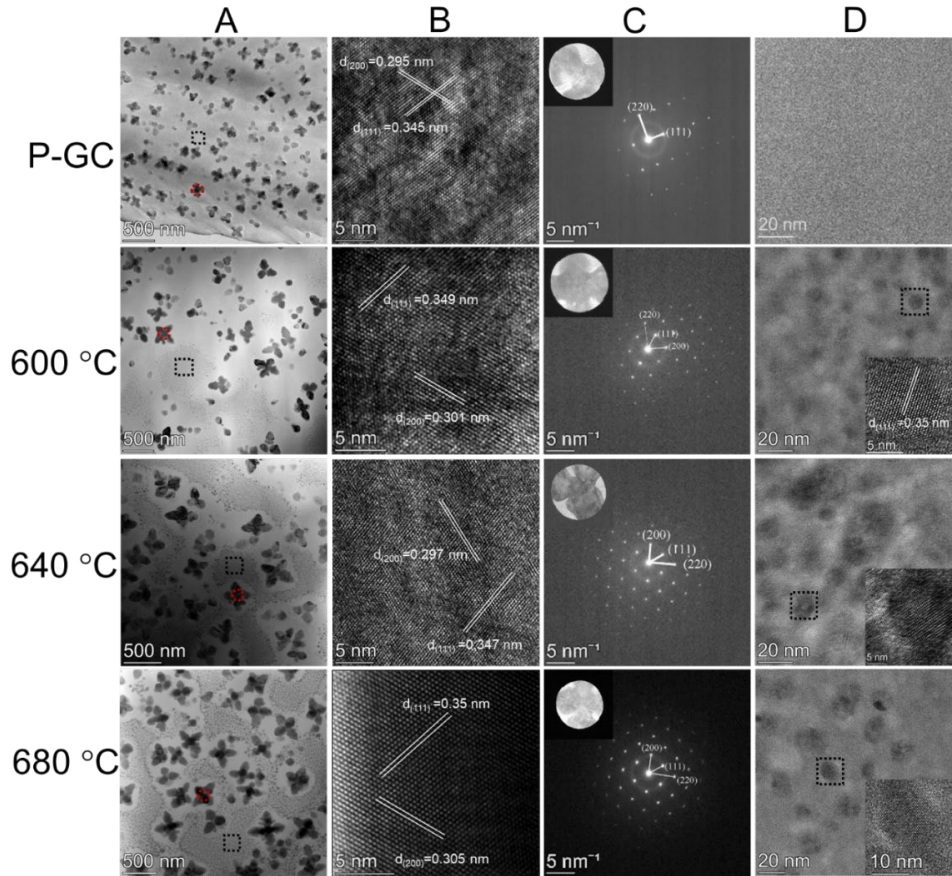


Figure 3. Probing the evolution of crystals during heat-treatment and the lattice structure by aberration-corrected transmission electron microscope (ACTEM) for both P-GC and the heat-treated P-GC samples. A: Overview images (with scale bar of 500 nm); B: Lattice structure; C: Electron diffraction of the domains (see inset) selected from red dashed circles in Figure A. Insets: D: Formation of the tiny spherical crystals and their evolution with HT temperature (see the black dashed squares in Figure A). Insets: Lattice structure of the tiny spherical crystals selected from black dashed squares in Figure D.

2.4. Local structural analysis of Si, Al and F atoms

To reveal the structural evolution during HT, we performed the ^{27}Al , ^{29}Si , and ^{19}F magic angle spinning (MAS) nuclear magnetic resonance (NMR) measurements on both P-GC and the heat-treated samples (Figures 4a, b, and c). It is seen in Figure 4a that ^{27}Al MAS NMR spectra of all the

samples feature the main resonance at about 60 ppm, which is attributed to four-coordinated aluminum (Al(IV)). Al³⁺ ions primarily exist in [AlO₄] tetrahedra besides a minor amount of [Al(O,F)₄].^[31] The small bumps are the spinning sidebands. After HT, the Al(IV) signal still appears at the same chemical shift as P-GC, suggesting that the coordination number of Al has no significant change. Note that some Al-F linkages in the interface regions could be replaced by the Al-O linkages upon HT owing to the increasing fraction of Ba₂LaF₇ crystals. This means that the coordination environment of Al could be altered.

Figure 4b illustrates ²⁹Si MAS NMR spectra of P-GC before and after HT. The resonance band at about -86 ppm is ascribed to Q⁽³⁾ species, where ⁽³⁾ denotes the sum of the numbers of Si-O-Si and Si-O-Al linkages per unit. However, it is hard to find out whether the Q⁽³⁾ units arise from the Si-O-Si or from Si-O-Al linkages. Thus, the coordination of Si⁴⁺ does not undergo an obvious change with HT temperature and remains as Q⁽³⁾.^[32] La³⁺ and F⁻ play a role as network modifiers, which lowers the network connectivity, thereby facilitating phase separation. It is likely that some of La³⁺ ions bond with non-bridging oxygen in the interphase regions, while some reside in the fluoride-rich phase composed of modifying oxides and fluorides, and some participate in the Ba₂LaF₇ crystals.

Figure 4c shows the ¹⁹F MAS NMR spectra of both P-GC and the heat-treated samples. All the spectra exhibit three broad signals at around -12, -142, and -185 ppm, which are denoted as F1, F2, and F3, respectively.^[30-31] The ratio of F1/F3 increases with increasing HT temperature owing to the increasing fraction of Ba₂LaF₇ crystals. F1 signal can be assigned to the F in La-F-Ba linkage.^[31] Both F2 and F3 signals are related to F species involved in the F-Al linkages of Al-F-Al and Na-F-Al, respectively.^[35] Upon HT, the F1 resonance shifts from -12 to -18 ppm, indicating that some of F ions participate in the formation of the Ba₂LaF₇ crystals, rather than stay in the glass matrix.^[36]

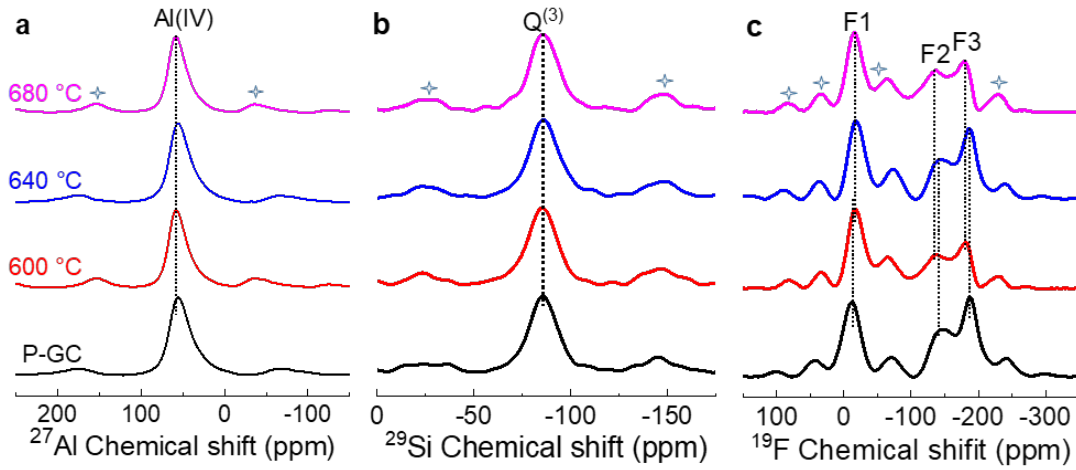


Figure 4. Structure characterizations by magic angle spinning (MAS) nuclear magnetic resonance (NMR). ^{27}Al (a), ^{29}Si (b), and ^{19}F (c) spectra of P-GC and the P-GC samples heat-treated at 600, 640 and 680 °C for 4 h. \star : spinning sidebands.

2.4. Origin of the transparency and luminescence enhancement

To explore the origin of the increase of transmittance with HT temperature, we measured the refractive indices (n) of both P-GC sample and the heat-treated ones at different wavelengths (Figure S5a). It is clearly seen that HT has led to a decrease in n values (Table. S5, SI). This means that the n values of the remaining glass matrix are lowered since that of Ba_2LaF_7 crystal is constant. n is proportional to the density of the samples,^[34-35] and hence the density exhibits the same variation trend with HT temperature as the n trend (Figure S5b).

Figure 5a illustrates n_d values at the wavelength of 588 nm and the n_d difference (Δn_d) between the studied samples and the pure Ba_2LaF_7 crystals for comparison. It is seen that Δn_d decreases with increasing HT temperature.^[39] When P-GC sample was heat-treated at 680 °C for 4 h, its n_d (1.5459) approaches that of Ba_2LaF_7 crystals ($\sim 1.54@588$ nm), and consequently the light scattering of the sample is greatly suppressed.^[40] Hence, this sample displays the highest transmittance. This is opposite to the trend for traditional GCs, where Δn_d increases with increasing HT temperature.

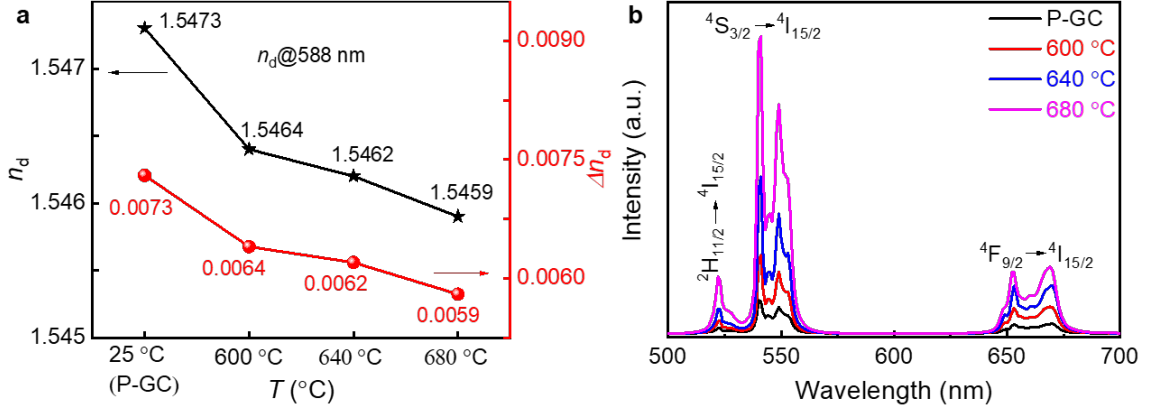


Figure 5. Effect of the HT temperature on the refractive index (n) and up-conversion (UC) luminescence of P-GC. (a) Refractive index (n_d) at the wavelength of 588 nm (black star symbols) and the refractive index difference (Δn_d) between the studied samples and the Ba_2LaF_7 crystallites (red sphere symbols). Error range of n_d : ± 0.0001 . (b) UC luminescence spectra obtained by using the 980 nm laser diode for the 4 studied samples.

To clarify the origin of the n trend with HT temperature, we performed EDS-elemental mapping analysis on both Ba_2LaF_7 crystals and the remaining glass matrices. Both the HAADF-STEM images of Ba_2LaF_7 crystals and the EDS-element mapping images of Ba, La, and F atoms are shown in Figure 6. The EDS-element mapping images for other types of atoms for P-GC and the three heat-treated samples are displayed in Figures S6-1, -2, -3, and -4, respectively. It is seen that the sizes of both the flower-like Ba_2LaF_7 crystals and the small spherical Ba_2LaF_7 crystals increase with HT temperature, and the concentrations of Ba, La, and F during HT also increase. Some Ba^{2+} and nearly all the La^{3+} and F^- diffuse from the glass matrix to both the existing flower-like Ba_2LaF_7 single-crystals and the small spherical Ba_2LaF_7 nanocrystals with increasing HT temperature. As a result of the escape of La^{3+} ions from the glass phase, the refractive index of the sample becomes lower, since La^{3+} ions are the main contributor to the refractive index of glass.^[41]

Figure 5b shows the UC emission spectra of both P-GC and the heat-treated samples under the 980 nm laser diode (LD) excitation. Compared to P-GC, the heat-treated samples exhibit much stronger UC emission arising from the transitions $^2H_{11/2} \rightarrow ^4I_{15/2}$ (523 nm), $^4S_{3/2} \rightarrow ^4I_{15/2}$ (541 and 548 nm), and $^4F_{9/2} \rightarrow ^4I_{15/2}$ (653 and 668 nm) of Er^{3+} . This enhancement can be attributed to the

following three factors. First, only a small portion of Er^{3+} and Yb^{3+} ions are present in Ba_2LaF_7 crystals in P-GC (Figure S6-1), but most of them exist in glass matrix. Since the glass matrix possesses higher phonon energy ($1200\text{--}1300\text{ cm}^{-1}$) than the crystals (270 cm^{-1}), the non-radiative relaxation rate of Er^{3+} and Yb^{3+} in the former is higher than that in the latter.^[25] Hence, the UC luminescence of the P-GC sample is weaker than that of the heat-treated samples. Second, both the content of Ba_2LaF_7 crystals and the transmittance of the studied samples increase with the HT temperature, and thus, UC luminescence is enhanced by lowering light scattering. Third, as the concentrations of Er^{3+} and Yb^{3+} ions in Ba_2LaF_7 crystals increase with HT temperature, the distance between Er^{3+} and Yb^{3+} in Ba_2LaF_7 crystals becomes shorter, leading to an increased probability of energy transfer between Er^{3+} and Yb^{3+} ions, and thereby to the enhancement of the UC luminescence. The UC luminescence of the studied P-GC is four times higher than that of the traditional GC (Figure S7a).^[25] Upon HT at $680\text{ }^\circ\text{C}$ for 4 h, the UC luminescence intensity is increased by about 23 times compared with the traditional GC. Thus, the studied P-GC is an excellent starting candidate for enhancing UC luminescence by proper HT.

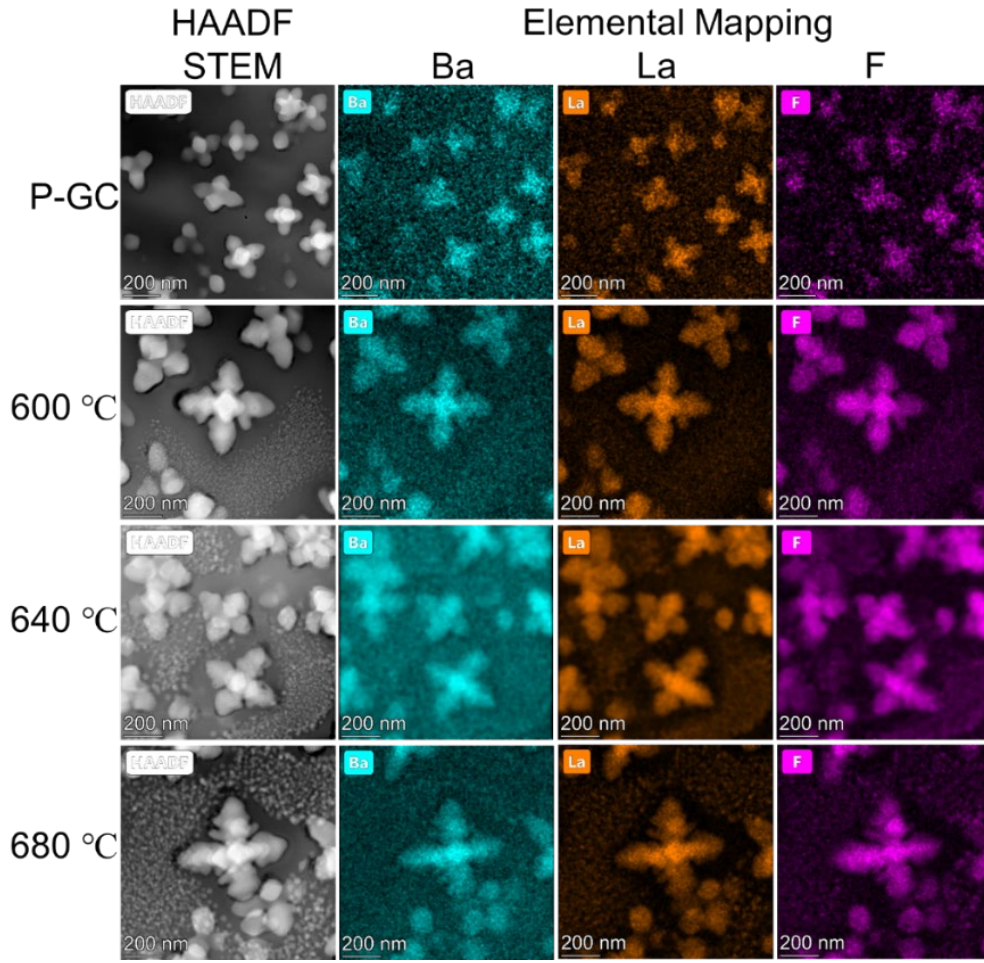


Figure 6. Effect of the HT temperature on the elements distribution around the crystals. Micrographs of P-GC and the heat-treated samples obtained by the High-Angle Annular Dark-Field Scanning Transmission Electron Microscope (HAADF-STEM) (See the first column); EDS-mapping images of the elements: Ba, La and F (see the second, third and fourth columns, respectively).

3. Conclusion

We prepared a novel type of functional glass ceramics via melt-quenching, that is, the translucent Er^{3+} - Yb^{3+} doped oxyfluoride glass-ceramic (P-GC) containing 200 nm sized flower-like Ba_2LaF_7 single-crystals. Interestingly, the transmittance of P-GC increases upon heat-treatment (HT) above T_g , and this is in contrast to common sense. Normally, HT leads to the growth of crystals, as well as to the formation of new Ba_2LaF_7 nanocrystals, and thereby lowering the transmittance of glass-ceramics. This anomalous phenomenon is attributed to the fact that the refractive index of the residual glass matrix approaches that of Ba_2LaF_7 crystals via HT, and thereby light scattering is

minimized. The mechanism of both crystal formation and growth was revealed by performing XRD, TEM and SEM analyses. The structural evolutions in the glass-ceramic during HT have been probed by NMR and TEM mapping. We found that HT can enhance not only the light transmittance, but also the UC luminescence of the studied glass-ceramic systems.

4. Molecular Dynamics Simulation Section

The structure of the precursor glass (PG) was simulated by using molecular dynamics (MD) simulations via the DL POLY 2.20 package developed at Daresbury Laboratory in the UK with a set of partial charge pairwise potentials with the form of Buckingham that has been successfully used in investigating the structures and phase separation of several oxyfluoride glass systems.^[31] In this study, we used La^{3+} ions to represent other rare earth ions such as Er^{3+} and Yb^{3+} ions hence the simulated glass has the composition of $45\text{SiO}_2\text{-}15\text{Al}_2\text{O}_3\text{-}12\text{Na}_2\text{O-}21\text{BaF}_2\text{-}8.5\text{LaF}_3$ (mol%). The input density (g/cm^3), as well as the simulation cell dimension and final density after equilibrium were listed in Table S6. The initial density was theoretically calculated and starting atoms positions were randomly generated.^[31] After generating the simulation bulk with atoms randomly distributed, the simulation bulk were heated to 6000 K and then cooled down to 300 K with a nominal cooling rate of 5 K/ps. The NVT and NVE ensembles were applied during this simulated melt and quench process at each temperature intervals during cooling. At 300 K, constant pressure relaxation with the NPT ensemble was used to allow the system to relax to its equilibrium volume. This is followed by NVE relaxations to generate configurations for final structural analysis. Further details of MD simulations of oxyfluoride glasses can be found in their recent papers.^[3,29,42]

5. Experimental Section

The precursor glass with the composition (mol%) of $45\text{SiO}_2\text{-}15\text{Al}_2\text{O}_3\text{-}12\text{Na}_2\text{O-}21\text{BaF}_2\text{-}7\text{LaF}_3\text{-}0.5\text{ErF}_3\text{-}1.0\text{YbF}_3$ was prepared by a melting-quench method. 20 g of the powdered mixture was melted in an electric furnace in air at 1450 °C for 45 min, and quickly cast onto a heating plate at

around 300 °C. Afterwards, to remove the permanent stress, the as-cast glass was annealed at 500 °C for 8 hours (h) and slowly cooled down to room temperature inside the furnace. The precursor glass sample contains about 42 vol% Ba₂LaF₇ crystals according to the XRD (see Figure S1a), and thus was denoted as the precursor glass-ceramic (P-GC). P-GC was cut into 4 small pieces of the same size and polished for both HT and property characterizations. To investigate the effect of HT on both the glass transition and the first crystallization behaviors of P-GC, the P-GC samples were heat-treated at 600, 640 and 680 °C for 4 hours (h), respectively.

Differential scanning calorimetry (DSC) (NETZSCH STA 449F3 Jupiter) measurements were carried out on both P-GC and the heat-treated P-GC samples in the temperature range from room temperature to 900 °C at the upscan rate of 10 °C/min in nitrogen. To study its crystallization kinetics and thermodynamics, P-GC was subjected to four DSC up- and downscan cycles. For each cycle, we chose five maximum scanning temperatures ($T_{\text{scan-max}}$) in the range between the glass transition temperature (T_g) and the temperature close to that of the first broad but shallow crystallization peak (T_{p1}) (see Figure S1b). Specifically, $T_{\text{scan-max}}$ was chosen to be 580, 600, 620, 640 and 660 °C. For each cycle, the sample was upscanned to $T_{\text{scan-max}}$ and subsequently cooled down to room temperature. XRD measurements were performed to identify the crystallization phase by a PANalytical diffractometer, operated at 40 kV and 40 mA, with Cu-K α ($\lambda = 1.5406 \text{ \AA}$) radiation during the 2θ range of 10-90° with a step size of 0.013°. The XRD data for Rietveld refinement of the structure was subjected to TOPAS for handling and refining the step analysis comprehensively, 2θ scan range is 10° - 90° with an interval of 0.02°. The Raman spectra were acquired using a micro-Raman spectrometer (inVia, Renishaw) in the range of 170 to 1200 cm⁻¹. The sample surface is excited by a 532 nm green HeNe laser for an acquisition time of 10 s. The as-precipitated crystallites in the studied samples were characterized by field-emission scanning electron microscopy (SEM, QUANTA 200) at the voltage of 30 kV. Before the SEM measurements,

the P-GC sample was etched in 7% HF solution for 25 s, while the heat-treated samples were etched for 15-20 s. The element compositions were determined by special aberration-corrected transmission electron microscope (ACTEM, FEI Titan Cubed Themis G2 300) equipped with energy-dispersive X-ray spectrometer (EDS), High-Angle Annular Dark Field transmission electron microscope (HAADF-STEM) and the selected area electron diffraction (SAED) at the voltage of 200 KV. The structure of the P-GC and the P-GC samples heat-treated at 600, 640 and 680 °C for 4 h were characterized by conducting the solid-state nuclear magnetic resonance (NMR) experiments (Bruker Avance III HD 500 MHz spectrometer (11.7 T)) at 25 °C. The single-pulse magic angle spinning (MAS) ^{19}F NMR signals were recorded at a resonance frequency of 470.5 MHz, using a 2.5 mm MAS NMR probe. The spinning rate was 24 kHz, and the 90° pulse length of 2 μs was used. The relaxation delay of ^{19}F in all the samples was 4 s. The ^{19}F chemical shifts were referenced to CFCl_3 , using AlF_3 ($\delta = -172.5$ ppm) as a secondary standard. ^{27}Al MAS NMR spectra were obtained at the resonance frequency of 130.2 MHz, operating with a 2.5 mm MAS probe at a spinning rate of 12 kHz. The typical pulse length was 0.7 μs (10° liquid flip angle). The relaxation delay was 0.5 s for all the samples. The chemical shifts of ^{27}Al were referenced to $\text{Al}(\text{NO}_3)_3$ (1 M) aqueous solution. ^{29}Si MAS NMR spectra were acquired at the resonance frequency of 99.3 MHz using a 4 mm MAS probe at a spinning rate of 6 kHz. A spin echo pulse scheme with the $\pi/2$ pulse length of 6 μs was used to acquire the spectrum. The relaxation delay time of P-GC and heat-treated P-GC samples was set as 300 s. The chemical shifts were referenced to tetrakis (trimethylsilyl) silane standard ($\delta = -9.7$ ppm).

The optical absorption spectra in the wavelength range of 275 to 800 nm were measured using a Varian Cary 50 spectrophotometer. The refractive index values (n) of both P-GC and the heat-treated P-GCs were measured at various wavelengths by KALNEW Precision Refractometer KPR-2000 at 25 °C. The UC photoluminescence spectra in the wavelength range of 500-700 nm were

recorded with a HITACHI F-7000 fluorescence spectrophotometer under the 980 nm laser excitation (excitation power was 0.5 W and the slit was 1 nm). The lifetime measurements were carried out using the method described in Ref.^[43] The UC photoluminescence decay curves of both P-GC and the P-GC sample heat-treated at 680 °C for 4 h were recorded by FLSP-980 spectrophotometer (Edinburgh Instruments Ltd., Edinburgh, UK), and the excitation source was 980 nm laser with the frequency of 500Hz.

Supporting Information

Supporting Information is available from the Wiley Online Library or from the author.

Acknowledgments

This work is supported by the China scholarship council (CSC, No. 201808530502), the National Natural Science Foundation of China (No. 51862020), Shandong Province (ZR2020ME025), and the Taishan Youth Scholar Project of Shandong Province (tsqn202103098). We are grateful to Dr. Xiaoming Zhang and Dr. Liwei Song for performing TEM measurements, and Jingbo Yu for conducting refractive index and solid-state NMR measurements.

Conflict of Interest

The authors declare no conflict of interest.

References

- [1] P. P. Fedorov, A. A. Luginina, A. I. Popov, *J. Fluor. Chem.* **2015**, 172, 22.
- [2] X. F. Liu, J. J. Zhou, S. F. Zhou, Y. Z. Yue, J. R. Qiu, *Prog. Mater. Sci.* **2018**, 97, 38.
- [3] Z. J. Fang, Z. Chen, W. C. Peng, C. Y. Shao, S. P. Zheng, L. L. Hu, J. Qiu, B. O. Guan, *Adv. Opt. Mater.* **2019**, 7, 1.
- [4] T. C. Ouyang, S. L. Kang, Z. S. Zhang, D. D. Yang, X. J. Huang, Q. W. Pan, J. L. Gan, J. R. Qiu, G. P. Dong, *Adv. Opt. Mater.* **2019**, 7, 1.
- [5] C. G. Lin, C. Bocker, C. Rüssel, *Nano Lett.* **2015**, 15, 6764.

- [6] R. R. Deng, F. Qin, R. F. Chen, W. Huang, M. H. Hong, X. G. Liu, *Nat. Nanotechnol.* **2015**, *10*, 237.
- [7] S. C. Lv, M. Q. Cao, C. Y. Li, J. Li, J. R. Qiu, S. F. Zhou, *ACS Appl. Mater. Interfaces* **2017**, *9*, 20664.
- [8] X. H. Xu, W. F. Zhang, D. C. Yang, W. Lu, J. B. Qiu, S. F. Yu, *Adv. Mater.* **2016**, *28*, 8045.
- [9] Z. M. Zhao, F. F. Hu, Z. M. Cao, F. F. Chi, X. T. Wei, Y. H. Chen, C. K. Duan, M. Yin, *Ceram. Int.* **2017**, *43*, 14951.
- [10] C. F. Bohren, D. R. Huffman, in *Absorpt. Scatt. Light by Small Part.*, **2007**.
- [11] J. B. Qiu, Q. Jiao, D. C. Zhou, Z. W. Yang, *J. Rare Earths* **2016**, *34*, 341.
- [12] T. Jiang, W. P. Qin, D. Zhao, *Mater. Lett.* **2012**, *74*, 54.
- [13] F. Wang, J. Wang, X. G. Liu, *Angew. Chemie-Int. Ed.* **2010**, *49*, 7456.
- [14] Y. Gao, Y. B. Hu, D. C. Zhou, J. B. Qiu, *J. Eur. Ceram. Soc.* **2017**, *37*, 763.
- [15] T. Berthier, V. M. Fokin, E. D. Zanotto, *J. Non. Cryst. Solids.* **2008**, *354*, 1721.
- [16] Q. J. Zheng, Y. F. Zhang, M. Montazerian, O. Gulbiten, J. C. Mauro, E. D. Zanotto, Y. Z. Yue, *Chem. Rev.* **2019**, *119*, 7848.
- [17] Y. Z. Yue, R. Von der Ohe, S. L. Jensen, *J. Chem. Phys.* **2004**, *120*, 8053.
- [18] Z. C. Li, D. C. Zhou, L. R. Jensen, J. B. Qiu, Y. F. Zhang, Y. Z. Yue, *J. Am. Ceram. Soc.* **2021**, *104*, 4471.
- [19] J. Y. Zhang, L. Longley, H. Liu, C. W. Ashling, P. A. Chater, K. A. Beyer, K. W. Chapman, H. Z. Tao, D. A. Keen, T. D. Bennett, Y. Z. Yue, *Chem. Commun.* **2019**, *55*, 2521.
- [20] Z. C. Li, D. C. Zhou, Y. Y. Yang, P. R. Ren, R. Zhu, T. Han, J. B. Qiu, *J. Alloys Compd.* **2018**, *731*, 1044.
- [21] Y. Z. Peng, J. S. Zhong, X. Y. Li, J. K. Chen, J. J. Zhao, X. S. Qiao, D. Q. Chen, *J. Eur. Ceram. Soc.* **2019**, *39*, 1420.
- [22] Q. H. Liu, Y. Tian, C. Z. Wang, F. F. Huang, X. F. Jing, J. J. Zhang, X. H. Zhang, S. Q. Xu, *Phys. Chem. Chem. Phys.* **2017**, *19*, 29833.
- [23] H. Aguiar, J. Serra, P. González, B. León, *J. Non. Cryst. Solids.* **2009**, *355*, 475.
- [24] P. González, J. Serra, S. Liste, S. Chiussi, B. León, M. Pérez-Amor, *J. Non. Cryst. Solids.* **2003**, *320*, 92.
- [25] X. P. Fan, J. Wang, X. S. Qiao, M. Q. Wang, J. L. Adam, X. H. Zhang, *J. Phys. Chem. B* **2006**, *110*, 5950.
- [26] B. Park, H. Li, L. R. Corrales, *J. Non. Cryst. Solids.* **2002**, *297*, 220.
- [27] C. G. Lin, L. G. Li, C. Bocker, C. Rüssel, *J. Am. Ceram. Soc.* **2016**, *99*, 2878.
- [28] C. Massobrio, J. C. Du, M. Bernasconi, P. S. Salmon, *Cham: Springer Series in Materials Science*, USA **2015**.

- [29] J. J. Zhao, X. X. Xu, X. T. Chen, Q. Xu, Z. Luo, X. S. Qiao, J. C. Du, X. P. Fan, G. D. Qian, *J. Eur. Ceram. Soc.* **2019**, *39*, 5018.
- [30] M. Poulain, *Nature* **1981**, *293*, 279.
- [31] J. J. Zhao, R. H. Ma, X. K. Chen, B. B. Kang, X. S. Qiao, J. C. Du, X. P. Fan, U. Ross, C. Roiland, A. Lotnyk, L. Kienle, X. H. Zhang, *J. Phys. Chem. C* **2016**, *120*, 17726.
- [32] M. M. Smedskjaer, J. C. Mauro, S. Sen, Y. Z. Yue, *Chem. Mater.* **2010**, *22*, 5358.
- [33] J. B. Yu, L. L. Hu, J. J. Ren, *Inorg. Chem.* **2021**, *60*, 3401.
- [34] X. Y. Zhang, L. L. Hu, J. J. Ren, *J. Phys. Chem. C* **2020**, *124*, 1594.
- [35] T. J. Kiczinski, J. F. Stebbins, **2002**, *306*, 160.
- [36] F. Muñoz, A. De Pablos-Martín, N. Hémono, M. J. Pascual, A. Durán, L. Delevoye, L. Montagne, *J. Non. Cryst. Solids* **2011**, *357*, 1463.
- [37] H. N. RITLAND, *J. Am. Ceram. Soc.* **1955**, *38*, 86.
- [38] Y. Y. Huang, A. Sarkar, P. C. Schultz, *J. Non. Cryst. Solids* **1978**, *27*, 29.
- [39] T. Y. Sun, Y. H. Li, W. L. Ho, Q. Zhu, X. Chen, L. M. Jin, H. M. Zhu, B. L. Huang, J. Lin, B. E. Little, S. T. Chu, F. Wang, *Nat. Commun.* **2019**, *10*, 1.
- [40] T. Wang, B. T. Liu, Y. Lin, Q. H. Yang, W. Gao, M. J. Li, J. B. Qiu, X. Yu, X. H. Xu, S. F. Y. *Opt. Lett.* **2020**, *45*, 5986.
- [41] A. Masuno, H. Inoue, K. Yoshimoto, Y. Watanabe, *Opt. Mater. Express* **2014**, *4*, 710.
- [42] J. J. Zhao, X. X. Xu, K. Ren, Z. Luo, X. S. Qiao, J. C. Du, J. B. Qiu, X. P. Fan, G. D. Qian, *Adv. Theory Simulations* **2019**, *2*, 1.
- [43] R.F. Wang, D. C. Zhou, J. B. Qiu, Y. Yang, C. Wang, *J. Alloys Compd.* **2015**, *629*, 310.

Supporting Information for
Transformation from Translucent into Transparent Rare Earth Ions Doped
Oxyfluoride Glass-Ceramics with Enhanced Luminescence

Zhencai Li, Chunying Chen, Weihui Shen, Lars R. Jensen, Xvsheng Qiao, Jinjun Ren, Jincheng Du, Yanfei Zhang, Jianbei Qiu, Yuanzheng Yue

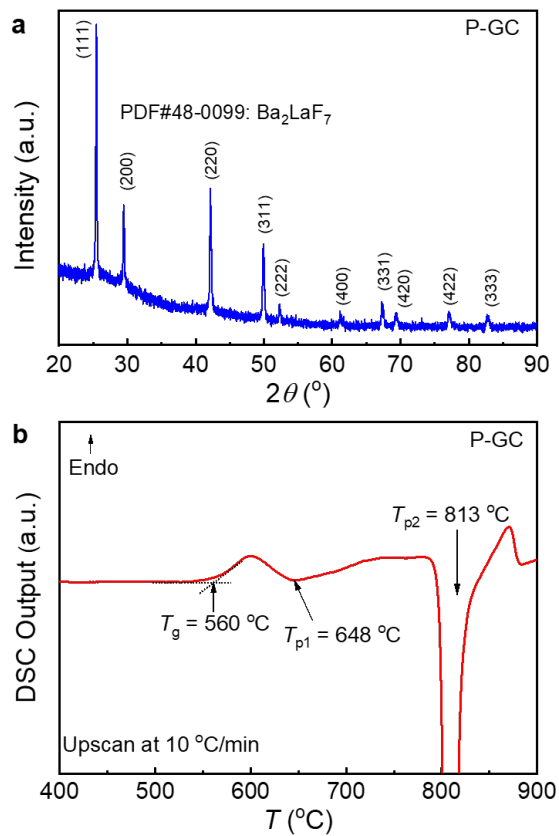


Figure S1. (a) X-ray diffraction (XRD) patterns of the precursor glass-ceramic (P-GC). Bars: The simulated pattern of cubic Ba_2LaF_7 (PDF#48-0099). (b) DSC output (in arbitrary unit) of P-GC as a function of temperature, exhibiting the glass transition temperature (T_g) and the temperatures of the first and second crystallization peaks (T_{p1} and T_{p2}).

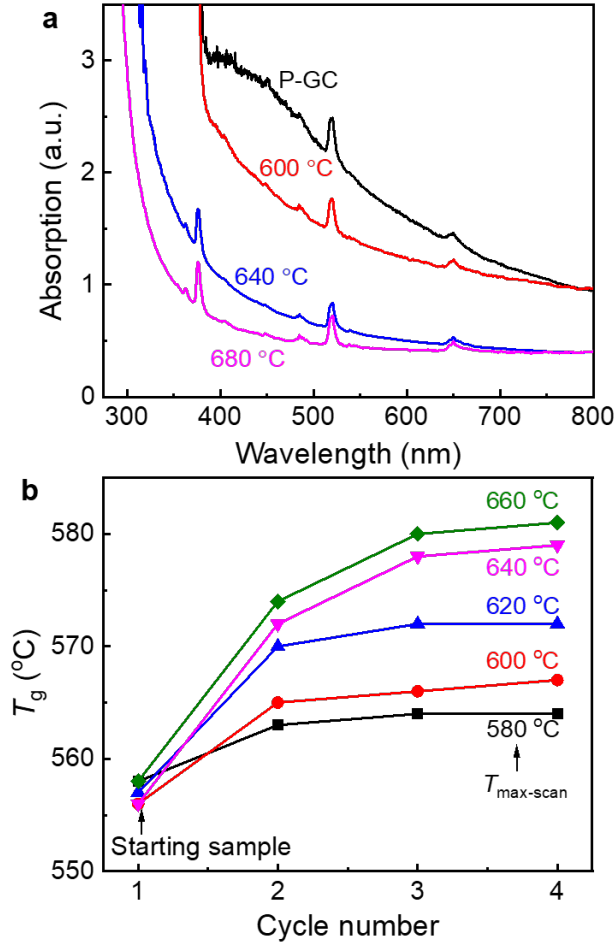


Figure S2. (a) Absorption spectra of P-GC before and after heat-treatment (HT) at 600, 640, and 680 °C for 4 hours (h), respectively. (b) T_g variation of the starting sample (P-GC) with increasing the scanning cycles for each maximum scanning temperature ($T_{\text{scan-max}}$). Note: for each cycle, the sample was upscanned to $T_{\text{scan-max}}$ and subsequently cooled down to room temperature at 10 °C/min.

The absorption spectra of both P-GC and three heat-treated P-GC samples in the wavelength range of 275 to 800 nm are shown in Fig. S2(a). Each of the spectra contains five main absorption peaks at around 362, 376, 486, 522, and 651 nm, which correspond to the transitions from the ground state $^4I_{15/2}$ to the excited states: $^2G_{7/2}$, $^4G_{11/2}$, $^2H_{9/2}$, $^2H_{11/2}$, and $^4F_{9/2}$ of Er^{3+} ions, respectively.^[1-2] Strikingly, the absorption intensity for the three heat-treated P-GC samples decreases with increasing the HT temperature, and this trend is opposite to that for traditional GCs.

Table S1. The glass transition onset temperatures (T_g in °C) and the onset temperatures (T_{cl} in °C) of first crystallization peaks of both the precursor glass-ceramic (P-GC) and the P-GC samples subjected to HT at 600, 640, and 680 °C for 1, 2 and 4 h, respectively.

T_{ht} (hrs)		1		2		4	
		T_g	T_{cl}	T_g	T_{cl}	T_g	T_{cl}
T_{ht} (°C)	P-GC	558	607	558	607	558	607
	600	582	630	591	635	594	638
	640	588	634	592	637	602	647
	680	587	638	594	640	601	651

Table S2. The T_g values (°C) of the P-GC samples that were upscanned to 580, 600, 620, 640, and 660 °C using DSC, respectively, and 4 scans for each maximum scanning temperature.

$T_{max-scan}$ (°C)		580	600	620	640	660
<i>Cycle number</i>	Scan 1	558	556	557	556	558
	Scan 2	563	565	570	572	574
	Scan 3	564	566	572	578	580
	Scan 4	564	567	572	579	581

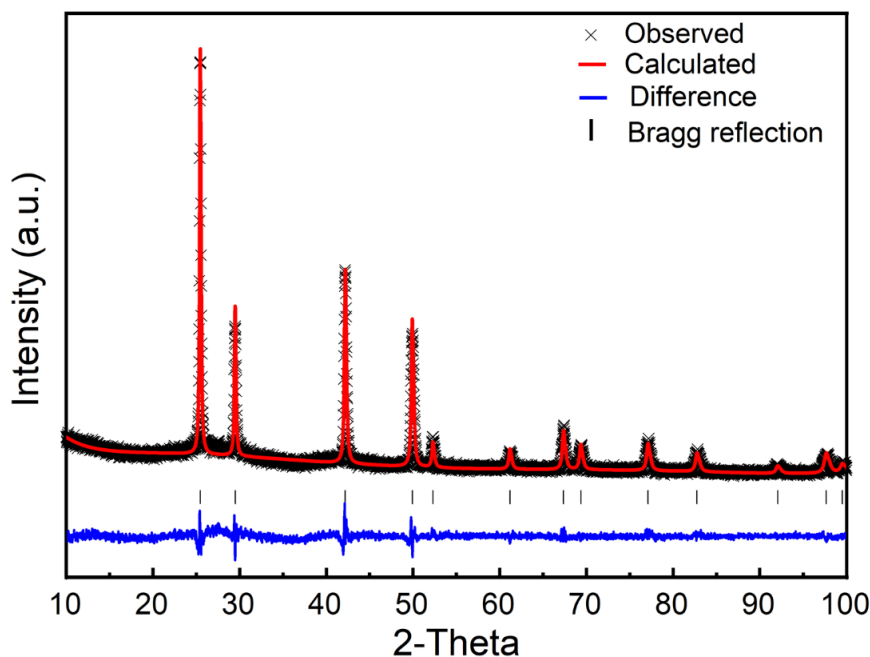


Figure S3. Rietveld refinement patterns of Ba_2LaF_7 crystals for P-GC sample heat-treated at 640 °C for 4 h. The observed raw XRD data (×) and the calculated pattern (red line). Black vertical lines in the profile indicate the Bragg's positions of the allowed reflections for Cu $K\alpha_1$ and $K\alpha_2$. The blue curve at the bottom is the difference in the observed and the calculated intensities on the same scale.

Table S3. Details of the Ba_2LaF_7 Crystal Structure and Equivalent Isotropic Parameters

Structure		Cubic			
Space group		Fm-3m (225)			
Lattice parameters		$a = b = c = 6.055 \text{ \AA}$, $\alpha = \beta = \gamma = 90^\circ$			
Z		4			
Volume of unit cell		222.04 \AA^3			
Atom	Wyckoff positions	x	y	z	Occupancy
Ba	4a	0	0	0	0.6667
La	4a	0	0	0	0.3333
F1	8c	0.25	0.25	0.25	0.629
F2	48i	0.5	0.3163	0.3163	0.0879

Table S4. Crystallinity in both P-GC and the three P-GC samples heat-treated at 600, 640, and 680 °C for 4 h, respectively.

	P-GC	600 °C	640 °C	680 °C
Crystallinity	42 %	44 %	57 %	64 %

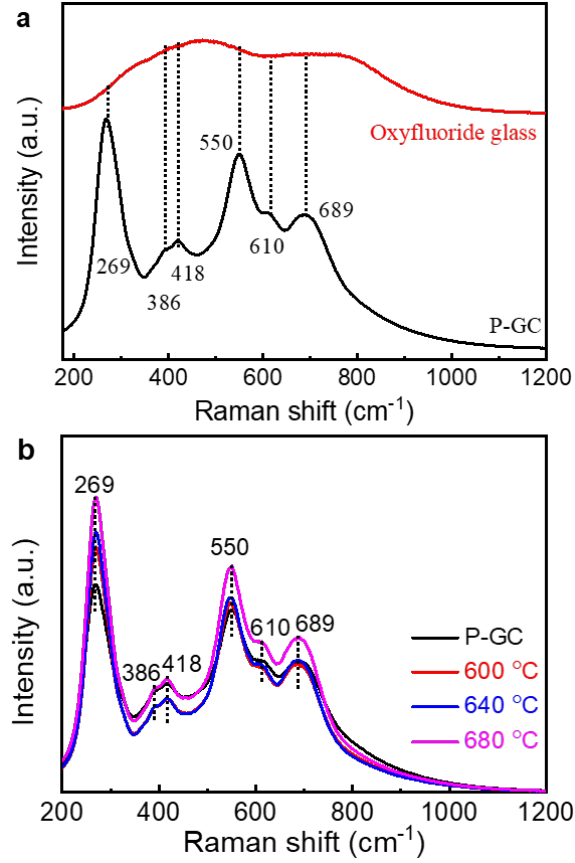


Figure S4. (a) Raman spectra between the P-GC sample and amorphous glass with the molar composition of $45\text{SiO}_2\text{-}15\text{Al}_2\text{O}_3\text{-}12\text{Na}_2\text{O-}21\text{BaF}_2\text{-}7\text{La}_2\text{O}_3\text{-}0.5\text{ErF}_3\text{-}1.0\text{YbF}_3$. (b) Raman spectra of P-GC and three heat-treated samples.

Table S5. Refractive index of the investigated both P-GC and the heat-treated samples.

Sample name	P-GC	600 °C	640 °C	680 °C
n_h (404.66 nm)	1.56264	1.56196	1.56146	1.56093
n_g (435.84 nm)	1.55858	1.54792	1.55742	1.55701
n_f (486.13 nm)	1.55372	1.55233	1.55249	1.55222
n_e (546.07 nm)	1.54931	1.54844	1.54837	1.54801
n_d (587.56 nm)	1.54732	1.54636	1.54623	1.54585
n_c (656.27 nm)	1.54458	1.54367	1.54332	1.54322
n_r (706.52 nm)	1.54308	1.54210	1.54163	1.54158

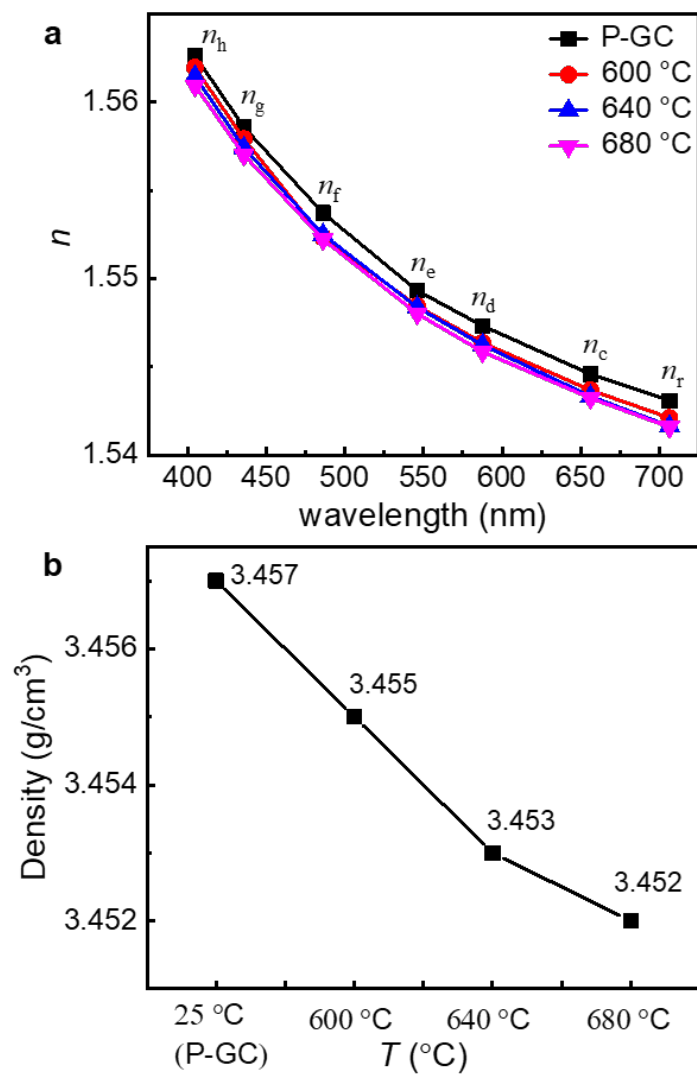


Figure S5. (a) n as a function of the light wavelength for P-GC and the heat-treated samples. (b) Density of both the P-GC sample and the heat-treated samples.

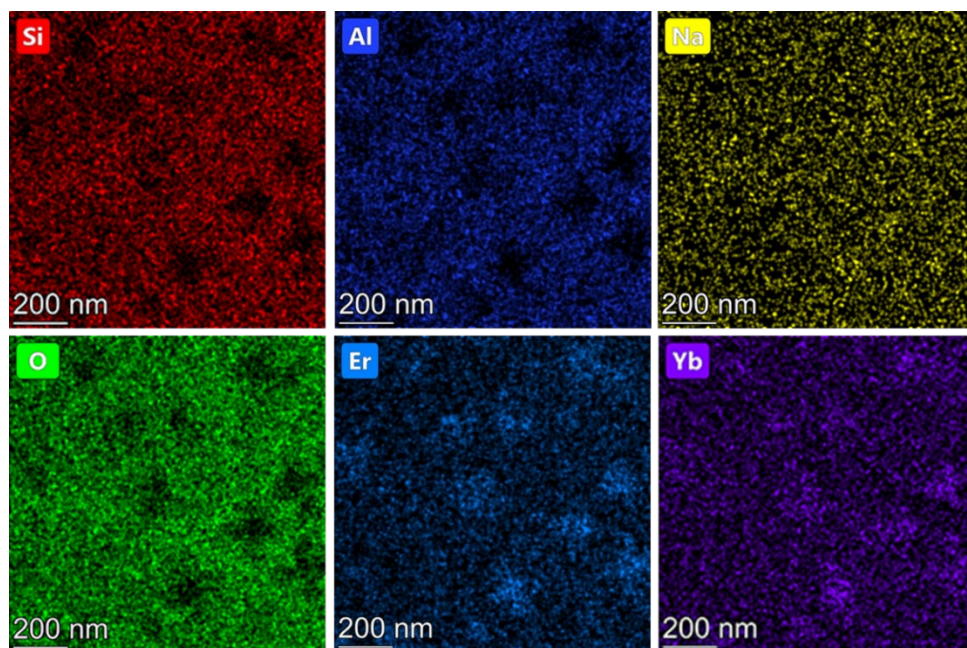


Figure S6-1 EDS element mapping images of the P-GC sample

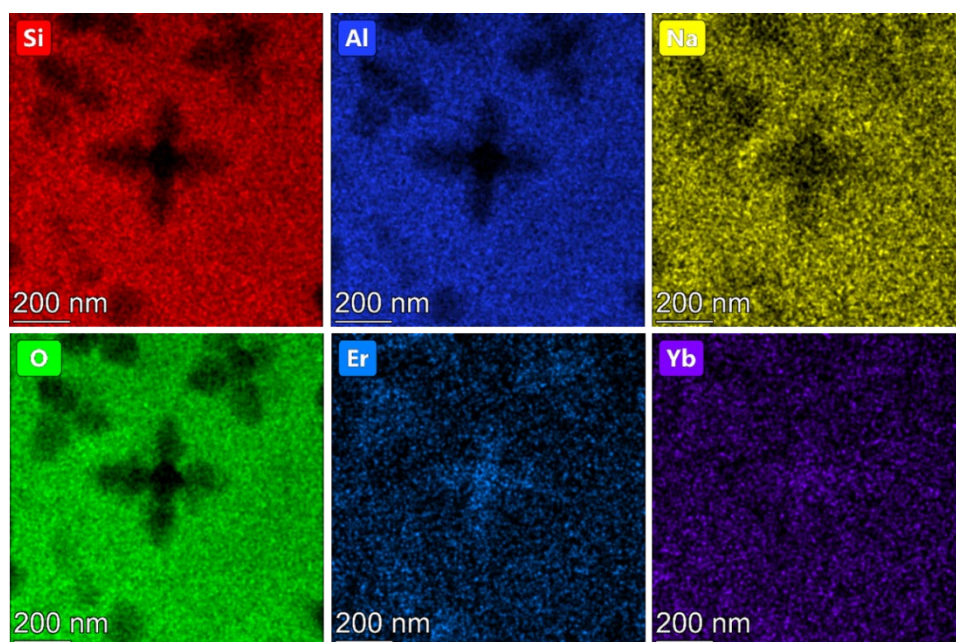


Figure S6-2 EDS element mapping images of the P-GC sample heat-treated at 600 °C for 4 h.

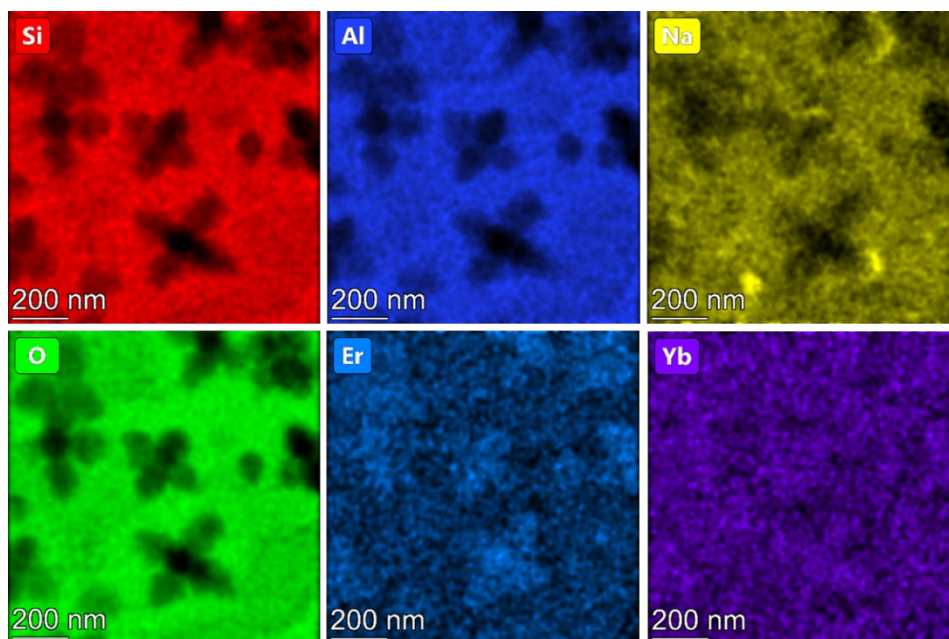


Figure S6-3 EDS element mapping images of the P-GC sample heat-treated at 640 °C for 4 h.

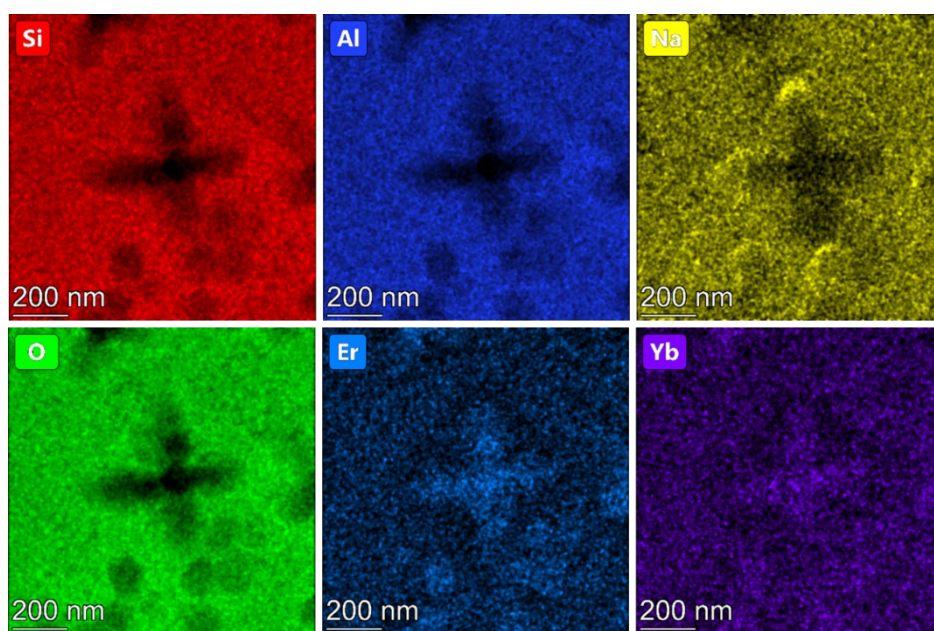


Figure S6-4 EDS element mapping images of the P-GC sample heat-treated at 680 °C for 4 h.

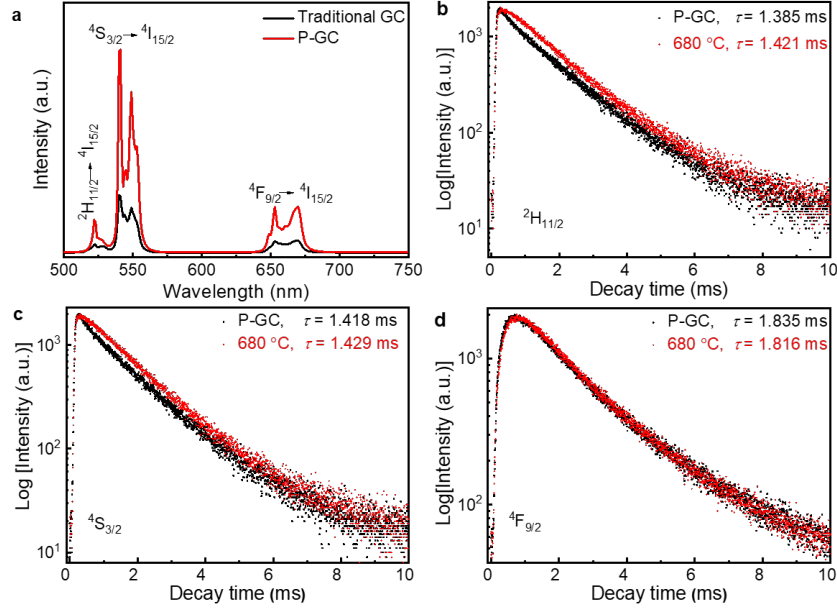


Figure S7. (a) Up-conversion luminescence spectra of P-GC and Traditional GC containing Ba₂LaF₇ crystals. (b-d) Decay lifetime of Er³⁺ in ²H_{11/2}, ⁴S_{3/2}, and ⁴F_{9/2} states for both P-GC and the P-GC sample heat-treated at 680 °C for 4 h, respectively.

In order to further demonstrate the energy transfer from Yb³⁺ to Er³⁺ ions, the UC luminescence decay curves for ²H_{11/2} → ⁴I_{15/2} (523 nm), ⁴S_{3/2} → ⁴I_{15/2} (541 nm), and ⁴F_{9/2} → ⁴I_{15/2} (653 nm) transitions of Er³⁺ ions at the excitation wavelength of 980 nm for both P-GC and the P-GC treated at 680 °C for 4 h are shown in Figures S9b-d. It can be seen that all decay curves can be well fitted by the second-order exponential decay mode as the following equation:^[3]

$$I = A_1 e^{(-t/\tau_1)} + A_2 e^{(-t/\tau_2)} \quad (3)$$

Where I is the luminescence intensity, A_1 and A_2 are the fitting parameters, t is the time, τ_1 and τ_2 are the slow and fast decay components (long and short lifetime), respectively. Using these above parameters, the average lifetime τ can be calculated by the following equation:

$$\tau = (A_1 \tau_1^2 + A_2 \tau_2^2) / (A_1 \tau_1 + A_2 \tau_2) \quad (4)$$

The average lifetime of ²H_{11/2}, ⁴S_{3/2}, and ⁴F_{9/2} states for both the P-GC and the HT samples are 1.385 and 1.421, 1.418, and 1.429, 1.835 and 1.816 ms, respectively. These results imply that the heat-

treated sample has a higher probability of energy transfer between Er^{3+} and Yb^{3+} ions.

Table S6. The amount of Si, Al, Na, Ba, La, O and F used, the total amount of atoms, the initial density (g/cm^3), as well as simulation cell size (\AA) and final density (g/cm^3) at 300 K.

Sample name	Si	Al	Na	Ba	La	O	F	Total number of atoms	Initial density	Final intensity	Final cell dimension (cubic, \AA)
PG	1350	900	720	630	255	4410	2025	10290	3.468	3.380	53.15

References

- [1] Y. Gao, Y. B. Hu, D. C. Zhou, J. B. Qiu, *J. Eur. Ceram. Soc.* **2017**, 37, 763.
- [2] H. K. Dan, D. C. Zhoua, R. F. Wang,, T. M. Hau, Q. Jiao, X. Yu, J. B. Qiu, *J. Rare Earths* **2013**, 31, 843.
- [3] R. F. Wang, J. Liu, Z. Zhang, *J. Alloys Compd.* **2016**, 688, 332.

The melting temperature effect on the optical properties of the rare earth co-doped oxyfluoride glass-ceramics

Zhencai Li^{1,2}, Linling Tan³, Dacheng Zhou², Lars R. Jensen⁴, Jinjun Ren⁵, Yanfei Zhang^{6,*}, Jianbei

Qiu^{2,*}, Yuanzheng Yue^{1,*}

¹Department of Chemistry and Bioscience, Aalborg University, 9220 Aalborg, Denmark

²School of Material Science and Engineering, Kunming University of Science and Technology, Kunming 650093, China

³Laboratory of IR Materials and Devices, The Research Institute of Advanced Technologies, Ningbo University, Ningbo 315211, PR China

⁴Department of Materials and Production, Aalborg University, 9220 Aalborg, Denmark

⁵Shanghai Institute of Optics and Fine Mechanics, Chinese Academy of Sciences, Shanghai 201800, China

⁶School of Materials Science and Engineering, Qilu University of Technology (Shandong Academy of Sciences), Jinan 250353, China

Abstract

We prepared four $\text{Er}^{3+}\text{-Yb}^{3+}$ co-doped oxyfluoride glass samples with the same chemical composition ($45\text{SiO}_2\text{-}15\text{Al}_2\text{O}_3\text{-}12\text{Na}_2\text{O-}21\text{BaF}_2\text{-}7\text{LaF}_3\text{-}0.5\text{ErF}_3\text{-}1.0\text{YbF}_3$) using different melting temperatures (1450, 1500, 1550 and 1590 °C) under the same quenching condition. It was found that one sample was glassy, whereas the other three contained fluoride crystals, i.e., they were glass-ceramics (GCs). We investigated the effect of the melting temperature on the crystallization, structure and optical properties of the four samples. These samples became phase-separated when lowering the melting temperature and, hence, Ba_2LaF_7 crystals were more easily precipitated, leading to a decrease in light transmittance, but an enhancement of the up-conversion (UC) luminescence. The crystallinity of the four samples was increased by isothermal heat-treatment (HT) for 2 hours above T_g , and this altered the light transmittance, but enhanced the UC luminescence. Thus, this work implies that the optical performances of the rare-earth doped oxyfluoride glass-ceramics could be optimized both by varying the melting temperature and by performing HT.

1. Introduction

An oxyfluoride glass-ceramic (GC) is composed of both glass phase and fluoride crystals, and is produced by heat-treating its parent or precursor glass (PG).¹ The PG is obtained by quenching its liquid state at a sufficient rate in order to bypass crystallization.² It was reported that the phase separation, e.g., separation between the fluoride-rich and the aluminosilicate oxide -rich glass phases in oxyfluoride precursor glasses (PGs), would assist the formation of nanocrystals.³ In other words, the fluoride crystals can be precipitated from the fluoride-rich phases in the oxyfluoride PGs via appropriate heat-treatment (HT). However, the growth of fluoride crystals in some oxyfluoride PGs is limited by the energy barrier for ionic diffusion in the liquid around crystals, and hence large crystals cannot be obtained.⁴ It is obvious that the small-sized fluoride crystals are difficult to accommodate more rare-earth (RE) ions for optimizing optical properties for applications. To achieve large-sized fluoride crystals in oxyfluoride PGs, some of the present authors recently designed numerous compositions, from which large fluoride crystals can be generated even during melt-quenching.⁵ The thus-derived oxyfluoride GCs contained different kinds of fluoride crystals, such as NaLuF₄, KTb₂F₇, and K₃YF₆.^{6,7,8}

Compared with traditional oxyfluoride GCs, the melt-quenching derived oxyfluoride GCs have the following two advantages. First, the latter ones contain larger-sized fluoride crystals with low phonon energy, which can accommodate RE ions, and this gives superior optical performances.⁹ Second, the preparation of such new types of GCs is simpler and more energy-saving since the HT procedure for traditional oxyfluoride GCs can be skipped.¹⁰ Thus, the melt-quenching derived oxyfluoride GCs have potential to be used as high performance optical materials. However, the origin of the formation of the fluoride crystals in the oxyfluoride PGs has not been clarified yet. To do so, in this work we take a new strategy, i.e.,

varying the melting temperature to probe the impact of the structural heterogeneity and phases separation on the tendency of fluoride crystal formation.

We prepared the $\text{Er}^{3+}\text{-Yb}^{3+}$ co-doped melt-quenching derived oxyfluoride precursor glass/GCs by quenching the glass melts from four different melting temperatures. To study the structural and morphological evolution of the glass/GCs during the crystallization process, we performed X-ray diffraction (XRD), the Raman spectroscopy and scanning electron microscopy (SEM) on both the melt-quenching derived and the heat-treated samples. In addition, we measured the phase transition of the studied samples by using the differential scanning calorimetry (DSC). We characterized the optical properties of the studied materials and gave implication on the optimum melting temperature for fabricating GCs with high optical performances.

2. Experimental

The melt-quenching derived oxyfluoride glass/GCs with the molar composition of $45\text{SiO}_2\text{-}15\text{Al}_2\text{O}_3\text{-}12\text{Na}_2\text{O-}21\text{BaF}_2\text{-}7\text{LaF}_3\text{-}0.5\text{ErF}_3\text{-}1.0\text{YbF}_3$ were prepared by the melt-quenching method. 10 g raw materials were mixed in proportion and put into an alumina crucible with a lid, which were heated in an electric furnace under air atmosphere to 1450, 1500, 1550, and 1590 °C, respectively, and kept for 45 min. Then the melt was cast quickly onto a stainless-steel plate preheated at 300 °C. Subsequently, the derived samples were annealed at 400 °C for 8 hours to release thermal stress and then cooled down to room temperature within the furnace. The above-derived samples melted at 1450, 1500, 1550, and 1590 °C were denominated as PG-1, PG-2, PG-3 and PG-4, respectively. Upon heat treatment (HT) for PG-1, PG-2, PG-3, and PG-4 at 640, 640, 620, and 640 °C for 2 hours, the heat-treated PG samples were named GC-1, GC-2, GC-3, and GC-4, respectively.

To investigate the thermodynamic properties of the studied samples, differential

scanning calorimetry (DSC, NETZSCH STA 449F3 Jupiter) was carried out at a heating rate of 10 °C/min under the nitrogen atmosphere. X-ray diffraction (XRD) measurements were performed to identify the crystallization phase by a powder diffractometer operated at 45 KV and 40 mA, using Cu-K α as the radiation. Raman spectra in the range of 175-1200 cm⁻¹ were obtained from a micro-Raman spectrometer (inVia, Renishaw) and by using a 532 nm green HeNe laser for 10 s at room temperature. The microstructure of the samples was characterized by field-emission scanning electron microscopy (SEM, QUANTA 200) at the voltage of 30 kV. The chemical compositions of the samples were determined by the special aberration-corrected transmission electron microscope (ACTEM, FEI Titan Cubed Themis G2 300) equipped with High-Angle Annular Dark Field transmission electron microscope (HAADF-STEM) and the selected area electron diffraction (SAED) at the voltage of 200 KV. The optical absorption spectra in the wavelength range of 275 to 1000 nm were measured using a Varian Cary 50 spectrophotometer. The local coordination environment of PG sample was characterized by the solid-state nuclear magnetic resonance (NMR) experiments (Bruker Avance III HD 500 MHz spectrometer (11.7 T)) at 25 °C. ²⁷Al magic angle spinning (MAS) NMR spectra were obtained at the resonance frequency of 130.2 MHz, operating with a 2.5 mm MAS probe at a spinning rate of 12 kHz. The typical pulse length was 0.83 μ s (10° liquid flip angle). The relaxation delay was 0.5 s for all the samples. The chemical shifts of ²⁷Al were referenced to Al(NO₃)₃ (1 M) aqueous solution. The Up-conversion (UC) luminescence spectra in the wavelength range from 500 to 700 nm were recorded with a HITACHI F-7000 fluorescence spectrophotometer under the 980 nm laser excitation.

3. Results and Discussions

3.1 Calorimetric analysis

Figs. 1(a) and (b) show the DSC output curves of both the melt-quenching derived PG (PG-1, PG-2, PG-3, and PG-4) and the heat-treated PG (GC-1, GC-2, GC-3, and GC-4)

samples, respectively. The onset temperatures of the glass transition peak (T_g), the first the crystallization peak (T_{c1}) and the melting peak (T_{m1}), and the second onset temperatures of the crystallization peak (T_{c2}) and the melting peak (T_{m2}) are determined from the DSC curves and their values are shown in Table 1, respectively. As shown in Fig. 1(a) and Table 1, with increasing the melting temperature to 1550 °C, both T_g and T_{c1} slightly decrease and then increase with further increasing the melting temperature to 1590 °C, implying the glass network connectivity first decreases and then increases since the glass structure determines T_g and T_{c1} .¹² In addition, T_{c2} values in PG samples gradually increase with increasing melting temperature, indicating that the second crystallization becomes more difficult owing to the more homogeneous melt at higher melting temperature. As the first melting peak in each PG-2, PG-3, and PG-4 sample might be overlapped by its second crystallization peak, T_{m1} is only presented in the curve of PG-1 sample. The values of T_{m2} exhibit slight variation between the range of 961 and 981 °C in all curves of PG samples.

As shown in Fig. 1(b), both T_g and T_{c1} of the corresponding GC samples increase upon heat treatment (HT) compared to each PG samples, respectively. This is because the concentration of $[\text{SiO}_4]$ and $[\text{AlO}_4]$ tetrahedral units increases and thus strengthens the glass network connectivity with HT.¹³ For each GC samples, The value of T_{c2} decreases upon HT compared with its PG counterpart, implying that the second crystallization in the remaining glass matrix becomes easier. However, the T_{m1} values in the GC samples are similar to those in PG-1 sample. This indicates that these values are ascribed to the melting point of Ba_2LaF_7 crystals as these melting peaks appear in GC-2, GC-3, and GC-4 samples after HT. Meanwhile, each T_{m2} of the GC samples is lower than that of the corresponding PG samples.¹⁴

To study the first crystallization event of both PG and GC samples, the corresponding crystallization enthalpy (ΔH) calculated by integrating the first crystallization peak are shown

in Figs. 1(a and b), respectively. The values of ΔH in Fig. 1(a) gradually decrease with PG samples obtained via increasing the melting temperature, indicating that the first crystallization ability and the degree of structural heterogeneity decrease with increasing the melting temperature.¹⁵ For GC samples, their values of ΔH in Fig. 1(b) become weak even vanish upon HT compared with the corresponding PG samples. This implies that their first crystallization ability decreases even disappears after HT. Therefore, each GC sample owns higher crystallinity than its corresponding PG sample.

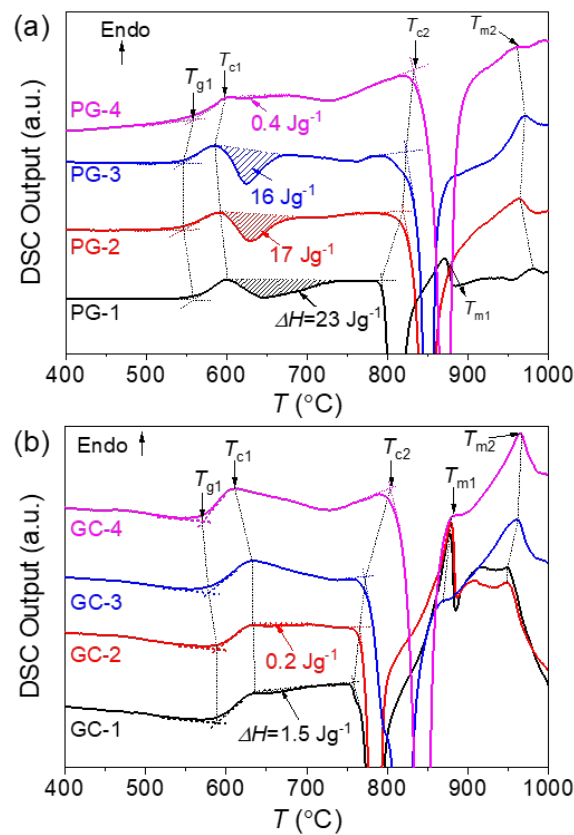


Figure 1. (a and b) Differential scanning calorimetry (DSC) output (arbitrary unit) of both PG (PG-1, PG-2, PG-3, and PG-4) and GC samples (GC-1, GC-2, GC-3, and GC-4), respectively. The onset temperatures of the glass transition temperatures (T_g), the first and second crystallization peaks (T_{c1} and T_{c2}), and the first and second melting peaks, i.e., the melting point (T_{m1} and T_{m2}) are marked in figure, respectively. The area of the first exothermic peak (i.e., the hatched area) represents the crystallization enthalpy (ΔH) determined by the extent of the crystal formation in each sample.

Table 1. Both the onset temperatures (in °C) of the glass transition (T_g), the first crystallization (T_{c1}), the second crystallization (T_{c2}), the first melting peak (T_{m1}), and the second melting peak (T_{m2}) of PG and GC samples, respectively.

T (°C)	T_g	T_{c1}	T_{c2}	T_{m1}	T_{m2}
----------	-------	----------	----------	----------	----------

<i>samples</i>	<i>PG-1</i>	559	601	793	872	981
	<i>PG-2</i>	547	593	819	~	965
	<i>PG-3</i>	546	587	824	~	970
	<i>PG-4</i>	558	600	831	~	961
	<i>GC-1</i>	591	637	758	877	950
	<i>GC-2</i>	590	635	765	879	951
	<i>GC-3</i>	578	633	772	870	963
	<i>GC-4</i>	571	612	803	881	967

To study the thermal stability of the PG samples, each of the four PG samples was max scanned to the temperatures (above T_{g1}) of 740, 700, 720, and 690 °C, respectively, for three times at the rate of 10 °C/min. The subsequent cooling process experienced the same rate as the prior heating rate. The varied T_g values in each sample determined from their corresponding DSC curves are shown in Figs. 2(a), (b), (c), and (d), respectively. Compared to the first up-scan, T_g values first sharply increase upon the second up-scan and then increase slowly even unchangeable at the third up-scan. Significantly, the area of the first crystallization peak in each DSC curve decreases with the number of cycles and then remains nearly constant. This could be explained by the formation of diffusion barrier at the interfaces between crystal and glass matrix after the first max-scan, which hinders the diffusion of F^- , La^{3+} , and Ba^{2+} ions to both the regions of existing Ba_2LaF_7 crystals and new nucleation sites.¹⁶ Thus, the glass network structure remains unchangeable.

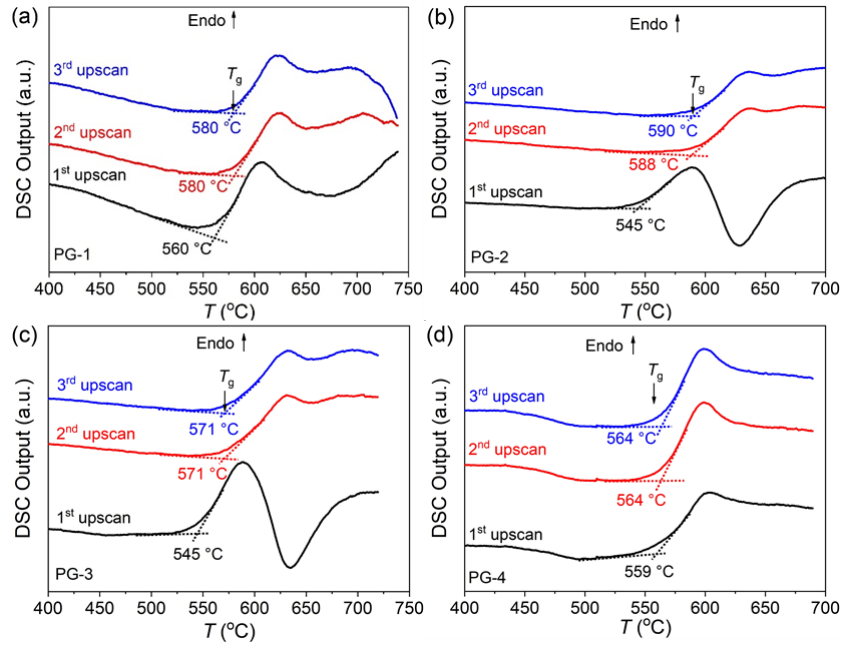


Figure 2. DSC output (arbitrary unit) of the PG-1 (a), PG-2 (b), PG-3 (c), and PG-4 (d) samples by repeated scan to maximum scanning temperature of 740, 700, 720, 690 °C, respectively, for three times at the same heating and cooling rate of 10 °C/min.

3.2 Structural analysis

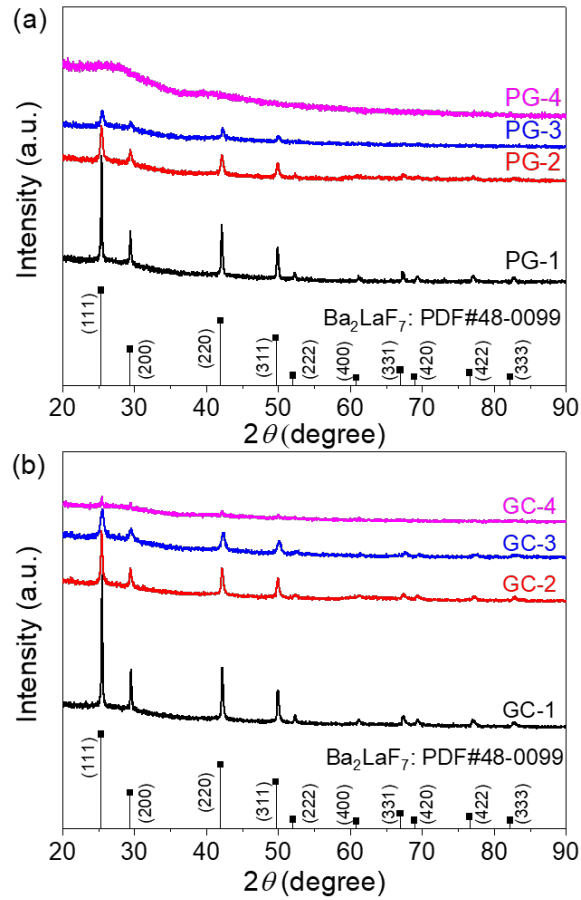


Figure 3. (a) X-ray diffraction (XRD) patterns of PG-1, PG-2, PG-3, and PG-4 samples, respectively. (b) XRD patterns of GC-1, GC -2, GC -3, and GC-4 samples, respectively. Bars represent cubic Ba₂LaF₇ crystal data (PDF#48-0099).

Fig. 3(a) shows the XRD patterns of the four PG samples. Obvious diffraction peaks were found in PG-1, PG-2 and PG-3 samples although their intensities become weaker with increasing the melting temperature. These peaks are well attributed to the face-centered cubic (FCC) Ba₂LaF₇ crystal (PDF#48-0099).⁶ However, no distinct diffraction peaks appear in the XRD pattern of PG-4 sample instead by two weak and broad humps, which is belonging to the characteristic diffraction peak of glass. The above-mentioned suggests that increasing the melting temperature can weaken the self-crystallization of Ba₂LaF₇ in the PG samples due to the lowered structural heterogeneity in the glass melt. Upon HT, the diffraction peaks in the XRD patterns of GC-1, GC-2, and GC-3 samples become more intensive. More importantly, several weak diffraction peaks corresponding to Ba₂LaF₇ crystal appear in the XRD pattern of GC-4 sample. In short, the content of Ba₂LaF₇ crystals in GC samples increases upon HT.¹⁷

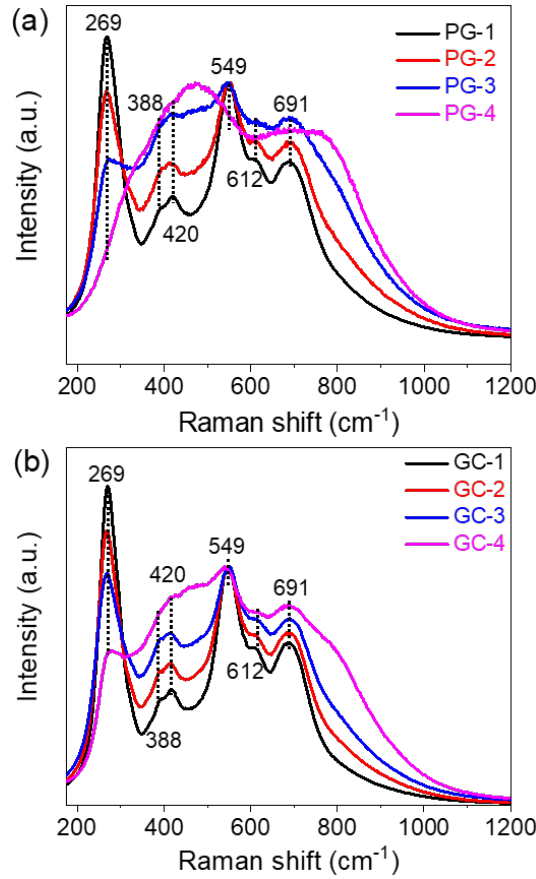


Figure 4. Normalized Raman spectra of PG (a) and GC (b) samples, respectively. Noting: Raman spectra of PG-1 sample normalized by the maximum intensity; Raman spectra of other samples normalized by the intensity of the peak at around 549 cm^{-1} , respectively.

Figs. 4(a) and (b) show the normalized Raman spectra of PG and GC samples, respectively. It can be seen from Fig. 4 (a) that the Raman peak at 269 cm^{-1} becomes weaker and disappears with increasing the melting temperature, while appears two broad Raman peaks in the spectrum of PG-4. This peak at 269 cm^{-1} should be ascribed to the vibration bonds of Ba-F and La-F in Ba_2LaF_7 crystals, further confirming that the formation of Ba_2LaF_7 crystals in PG-1, PG-2 and PG-3 samples during quenching while the amorphous nature of PG-4.¹⁸ That is, both the content of Ba_2LaF_7 crystals and the structural heterogeneity in PG samples decrease with increasing the melting temperature.¹⁹ The other Raman peaks at 388-691 cm^{-1} can be assigned to Si-O-Si (Al) symmetric stretching vibration modes, while the Raman peak at around 800 cm^{-1} in PG-4 is related to bending vibration

modes.²⁰ In addition, the peaks at 425, 550, and 691 cm^{-1} are contributed to the symmetric stretch of five-, four- and three-fold ring structures, respectively.^{21,22} To investigate the effect of HT on both the further crystallization and local microstructure, the Raman spectra of GC samples are illustrated in Fig. 4(b). Compared to the Raman spectra of PG-1, PG-2, and PG-3 in Fig. 4a, the Raman peak corresponding to Ba_2LaF_7 crystal at 269 cm^{-1} becomes stronger upon HT, consisting with the XRD results (Fig. 3). Moreover, the weak Raman peak at 269 cm^{-1} appears in GC-4 sample, implying that the crystallization of Ba_2LaF_7 takes place upon HT. Meanwhile, the Raman peaks of tetrahedral unit also occur in GC-4 sample, which is like that in other GC samples.

Fig. 5 shows the TEM images of PG-1, PG-4, GC-1, and GC-4 samples, respectively. As shown in Fig. 5(a), flower-like Ba_2LaF_7 crystals are present in the glass matrix of PG-1, which size increases with the HT. The interplanar distances between the adjacent fringes are determined to be 0.35 nm, which match with the (111) plane of Ba_2LaF_7 crystals. Furthermore, some additional spherical Ba_2LaF_7 nanocrystals appear in GC-1 sample (Fig. 5(c)). Fig. 5(b) confirms the glassy nature of the PG-4 sample since there are no distinct lattice fringes. After HT, some ordered domains (about 10 nm) with regular lattice fringe denoted by the dashed circles are present in the glass matrix (Fig. 5(d)), which are conformed to be Ba_2LaF_7 crystals by measuring the interplanar spacing of 0.35 nm in the (111) plane (Inset of Fig. 5(d)).

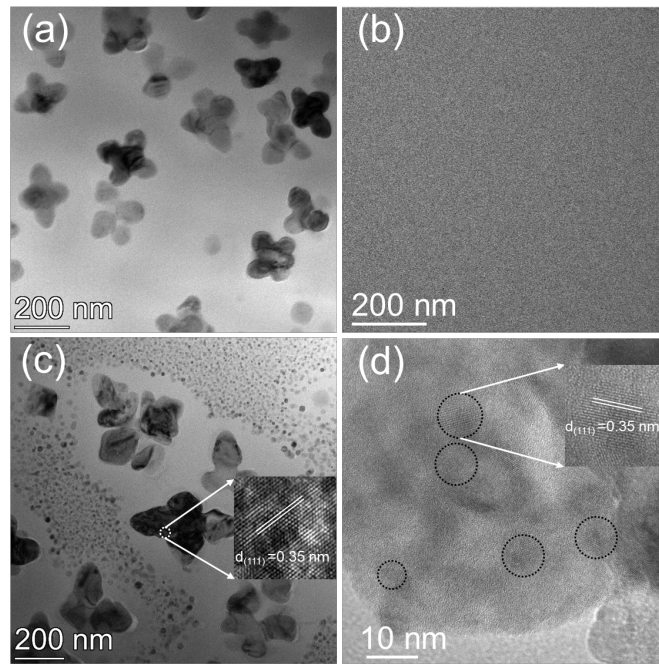


Figure 5. AC-TEM images of both PG-1 (a), PG-4 (b), GC-1 (c), and GC-4 (d) samples, respectively. Note that the flower-like domains (PG-1), small dot regions (GC-1), and regions marked with dashed circles (GC-4) present Ba_2LaF_7 crystals.

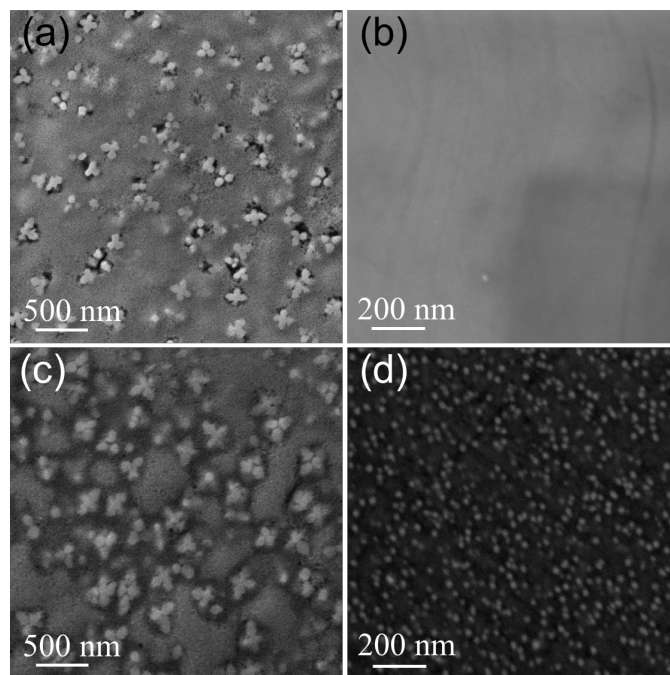


Figure 6. SEM micrographs of both the PG and the corresponding GC samples, (a) PG-1; (b) PG-4; (c) GC-1; (d) GC-4. For PG-1 and GC-1, white flower-like domains and grey regions are Ba_2LaF_7 crystals and tiny spherical Ba_2LaF_7 nanocrystals, respectively. GC-4, small dot regions are new-formed Ba_2LaF_7 nanocrystals, embedding in the glass matrix (large black areas).

SEM micrographs of PG-1, PG-4, GC-1 and GC-4 are shown in Fig. 6. In Fig. 6(a), some flower-like Ba_2LaF_7 crystals of about 200 nm (white domains) are distributed uniformly in the parent glass matrix, which grow to larger size, i.e., around 300 nm, along with some new-formed tiny spherical Ba_2LaF_7 nanocrystals about 20 nm in the residual glass matrix upon HT (Fig. 6(c)). For PG-4 sample (Fig. 6(b)), no crystals are observed in the glass matrix, which suggests that PG-4 is oxyfluoride glass. After HT, some spherical nanocrystals with the size of about 10 nm precipitate from the glass matrix (Fig. 6(d)).²³ This phenomenon agrees well with the TEM results.

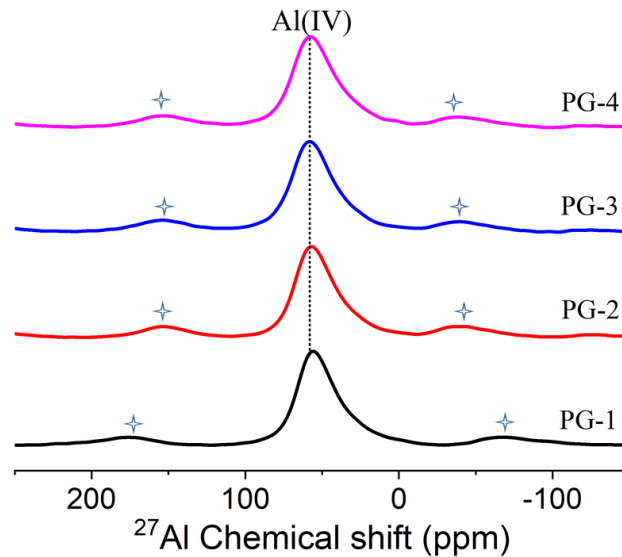


Figure 7. ^{27}Al magic angle spinning (MAS) NMR spectra of PG-1, PG-2, PG-3, and the PG-4 samples, respectively. (✱) denotes spinning sidebands.

To reveal the effect of melting temperature on the microstructures of the PG samples, we performed the ^{27}Al magic angle spinning (MAS) nuclear magnetic resonance (NMR) measurements (Fig. 7). It is seen that ^{27}Al MAS NMR spectra of all the samples feature the main resonance at about 60 ppm, which are attributed to four-coordinated aluminum (Al(IV)).²⁴ In addition, the Al(IV) signal in PG-2, -3 and -4 samples as the same chemical shift as PG-1, suggesting that the coordination environment of Al has no significant change with increasing melting temperature. It is reported for PG-1 sample that Al^{3+} ions can be

distributed both in the interface regions and in glass network to form $[\text{Al}(\text{O},\text{F})_4]$ and $[\text{Al}(\text{O})_4]$ tetrahedra, respectively. However, some Al-F linkages in the interface regions could be replaced by the Al-O linkages with increasing the melting temperature due to the volatilization of F element. This means that the coordination environment of Al could be slightly altered. Noting that the small bumps are the spinning sidebands.

3.3 Optical properties

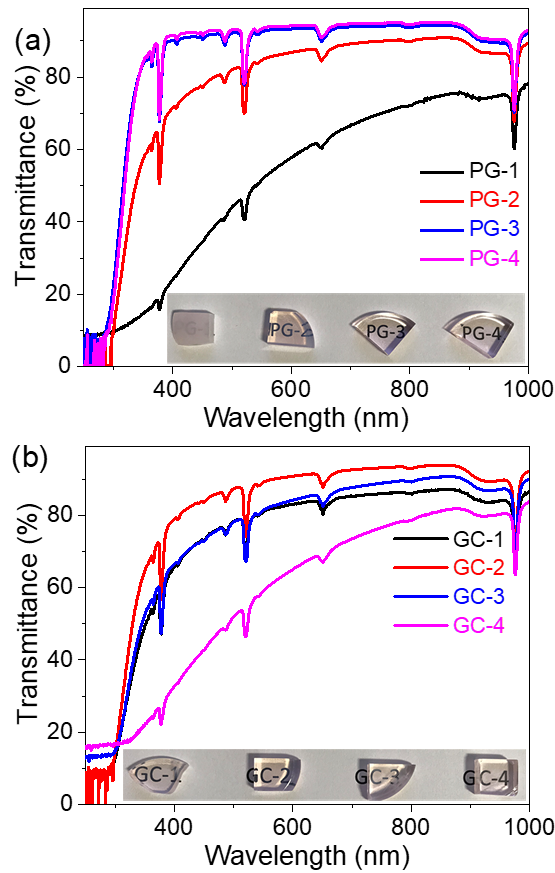


Figure 8. (a) Transmittance spectra of PG samples (PG-1, PG-2, PG-3, and PG-4); (b) Transmittance spectra of GC samples (GC-1, GC-2, GC-3, and GC-4), respectively.

Fig. 8 shows the transmittance spectra in the range of 275 to 1000 nm of PG and GC samples, respectively, and their corresponding optical images. Four main absorption peaks of Er^{3+} ions at around 378, 488, 523, and 653 nm are observed and attributed to the transitions from the ground state $^4\text{I}_{15/2}$ to the excited states $^4\text{G}_{11/2}$, $^4\text{F}_{7/2}$, $^2\text{H}_{11/2}$, and $^4\text{F}_{9/2}$, respectively.¹² In addition, the absorption peaks at around 978 nm are observed in the transmission spectra,

which corresponds to the transitions of Yb^{3+} : $^2\text{F}_{7/2} \rightarrow ^2\text{F}_{5/2}$. The transmittance of PG sample (Fig. 8(a)) gradually increases with increasing the melting temperature, illustrated by the highest optical transmittance around 95% (per 1 mm) of PG-4 sample. This is because both the size of Ba_2LaF_7 crystals and refractive index differences between the crystal phase and the remaining glass matrix in PG-1 sample are the largest compared to other PG samples, thus leading to the strongest light scattering effect and the lowest transmittance.

Interestingly, it displays an anomalous scenario that the transmittance of PG-1 and PG-2 samples increases upon HT although the crystals increases in the corresponding GC samples compared with that of traditional glass-ceramics.¹ This implies that the HT can adjust the refractive index of the residual glass matrix to match that of the crystals, resulting in a decrease in light scattering. However, the transmittance of GC-3 and GC-4 samples decreases upon HT, which means the refractive index differences between the crystals and the glass matrix are larger than that in PG-3 and PG-4 samples.

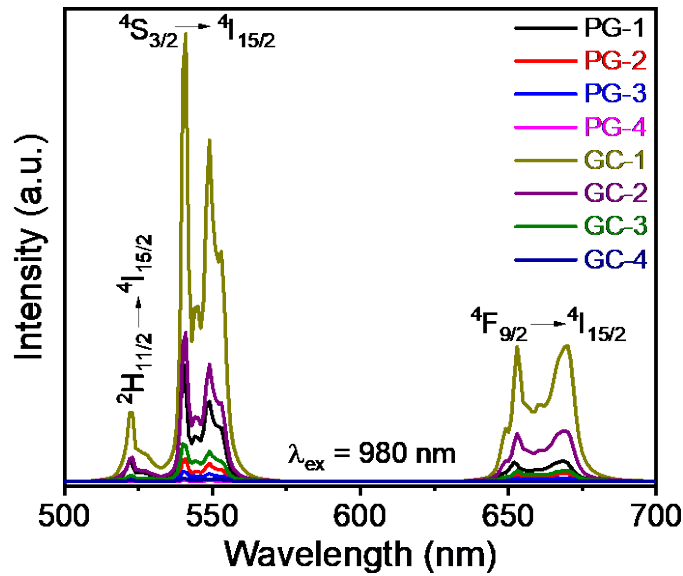


Figure 9. Up-conversion (UC) luminescence spectra of Er^{3+} - Yb^{3+} co-doped PG and GC samples.

Fig. 9 shows the UC luminescence spectra in the wavelength range from 500 to 700 nm of Er^{3+} - Yb^{3+} co-doped PG and GC samples obtained by excitation of the 980 nm laser. The

characteristic UC luminescence peaks at 523, 541, and 653 nm are attributed to the transitions from the excited states: $^2H_{11/2}$, $^4S_{3/2}$, and $^4F_{9/2}$ to the ground state: $^4I_{15/2}$ of Er^{3+} ions, respectively. It is seen that the UC luminescence intensity of PG samples decreases with the increasing melting temperatures. In addition, GC samples exhibit higher UC luminescence intensity compared with the corresponding PG samples. Meanwhile, the stark splitting of these energy levels in GC samples is more pronounced compared with the corresponding PG samples.²⁵ The above results can be ascribed to the fact that the incorporation of more Er^{3+} ions into the low phonon energy environment of Ba_2LaF_7 nanocrystals can reduce the probability of nonradiative relaxation.²⁶

4. Conclusion

In this work, Er^{3+} - Yb^{3+} co-doped melt-quenching derived oxyfluoride precursor glass (PG) samples were prepared by adjusting the melting temperature. The effect of melting temperature on crystallization behavior, structural evolution, optical and mechanical properties was investigated. The crystallization enthalpy at the first crystallization peak decreased with increasing the melting temperature, indicating that their crystallization capability of PG samples decreases with increasing the melting temperature. Interestingly, the transmittance of PG samples increases with increasing the melting temperature, which can be attributed to the fact that the microstructure of PG samples becomes more homogeneous than that of PG samples prepared by decreasing the melting temperature. In addition, the Up-conversion luminescence intensity of PG samples decreases with increasing the melting temperature. Upon heat treatment (HT), GC samples exhibit higher crystallinity and UC luminescence compared with the corresponding PG samples. Thus, this study not only offers a new path via controlling the melting temperature to design PG samples but also investigates the impact of HT on tailoring optical and mechanical properties.

Acknowledgments

This work is supported by the China scholarship council (CSC, No. 201808530502), the National Natural Science Foundation of China (No. 12064021), and the Taishan Youth Scholar Project of Shandong Province (tsqn202103098).

Declaration of Competing Interest

The authors declare that they have no known competing financial interests or personal relationships that could have appeared to influence the work reported in this paper.

References:

- (1) Liu, X.; Zhou, J.; Zhou, S.; Yue, Y.; Qiu, J. Transparent Glass-Ceramics Functionalized by Dispersed Crystals. *Prog. Mater. Sci.* **2018**, *97*, 38–96.
- (2) Qiao, A.; Bennett, T. D.; Tao, H.; Krajnc, A.; Mali, G.; Doherty, C. M.; Thornton, A. W.; Mauro, J. C.; Greaves, G. N.; Yue, Y. A Metal-Organic Framework with Ultrahigh Glass-Forming Ability. *Sci. Adv.* **2018**, *4* (3), 1–8.
- (3) Bocker, C.; Wiemert, J.; Rüssel, C. The Formation of Strontium Fluoride Nano Crystals from a Phase Separated Silicate Glass. *J. Eur. Ceram. Soc.* **2013**, *33* (10), 1737–1745.
- (4) Bhattacharyya, S.; Boeker, C.; Heil, T.; Jinschek, J. R.; Höche, T.; Rüssel, C.; Kohl, H. Experimental Evidence of Self-Limited Growth of Nanocrystals in Glass. *Nano Lett.* **2009**, *9* (6), 2493–2496.
- (5) Zhao, Z.; Hu, F.; Cao, Z.; Chi, F.; Wei, X.; Chen, Y.; Duan, C. kui; Yin, M. Self-Crystallized Ba₂LaF₇:Nd³⁺/Eu³⁺ Glass Ceramics for Optical Thermometry. *Ceram. Int.* **2017**, *43* (17), 14951–14955.
- (6) Shen, W.; Yang, Y.; Li, Z.; Khan, M. I.; Cao, E.; Zhou, D.; Qiu, J. Effect of Melting Temperature on the Structure of Self-Crystallized Ba₂LaF₇ Glass-Ceramics. *J. Non. Cryst. Solids* **2019**, *523* (August), 119579.
- (7) Chen, D.; Wan, Z.; Zhou, Y.; Huang, P.; Ji, Z. Ce³⁺ Dopants-Induced Spectral Conversion from Green to Red in the Yb/Ho: NaLuF₄ Self-Crystallized Nano-Glass-Ceramics. *J. Alloys Compd.* **2016**, *654*, 151–156.
- (8) Cao, J.; Li, X.; Wang, Z.; Wei, Y.; Chen, L.; Guo, H. Optical Thermometry Based on Up-Conversion Luminescence Behavior of Self-Crystallized K₃YF₆:Er³⁺ Glass Ceramics. *Sensors and Actuators, B: Chemical*. 2016, pp 507–513.
- (9) Hu, F.; Chen, W.; Jiang, Y.; Song, W.; Wei, R.; Guo, H. Tm³⁺-Doped Na_{0.5}-XYb_{0.5+x}F_{2+2x} Self-Crystallization Glass Ceramics: Microstructure and Optical Thermometry Properties. *J. Lumin.* **2019**, *214* (December 2018), 0–4.
- (10) Xu, X.; Zhang, W.; Yang, D.; Lu, W.; Qiu, J.; Yu, S. F. Phonon-Assisted Population Inversion in Lanthanide-Doped Upconversion Ba₂LaF₇Nanocrystals in Glass-Ceramics. *Adv. Mater.* **2016**, *28* (36), 8045–8050.

- (11) To, T.; Jensen, L. R.; Smedskjaer, M. M. On the Relation between Fracture Toughness and Crack Resistance in Oxide Glasses. *J. Non. Cryst. Solids* **2020**, *534* (February), 119946.
- (12) Li, Z.; Zhou, D.; Jensen, L. R.; Qiu, J.; Zhang, Y.; Yue, Y. Er³⁺-Yb³⁺ Ions Doped Fluoro-Aluminosilicate Glass-Ceramics as a Temperature-Sensing Material. *J. Am. Ceram. Soc.* **2021**, No. April, 4471–4478.
- (13) Zheng, Q.; Zhang, Y.; Montazerian, M.; Gulbiten, O.; Mauro, J. C.; Zanutto, E. D.; Yue, Y. Understanding Glass through Differential Scanning Calorimetry. *Chem. Rev.* **2019**, *119* (13), 7848–7939.
- (14) Liu, H.; Qiao, A.; Gao, Y.; Tao, H.; Zhao, X.; Hu, Y.; Yue, Y. Reversible Formation-Melting of Nano-Crystals in Supercooled Oxyfluoride Germanate Liquids. *J. Eur. Ceram. Soc.* **2019**, *39* (16), 5373–5379.
- (15) Liu, S.; Kong, Y.; Tao, H.; Sang, Y. Crystallization of a Highly Viscous Multicomponent Silicate Glass: Rigidity Percolation and Evidence of Structural Heterogeneity. *J. Eur. Ceram. Soc.* **2017**, *37* (2), 715–720.
- (16) Lin, C.; Bocker, C.; Rüssel, C. Nanocrystallization in Oxyfluoride Glasses Controlled by Amorphous Phase Separation. *Nano Lett.* **2015**, *15* (10), 6764–6769.
- (17) Zhao, J.; Xu, X.; Li, P.; Li, X.; Chen, D.; Qiao, X.; Du, J.; Qian, G.; Fan, X. Structural Origins of RF₃/NaRF₄ Nanocrystal Precipitation from Phase-Separated SiO₂-Al₂O₃-RF₃-NaF Glasses: A Molecular Dynamics Simulation Study. *J. Phys. Chem. B* **2019**, *123* (13), 3024–3032.
- (18) Kang, S.; Huang, Z.; Lin, W.; Yang, D.; Zhao, J.; Qiao, X.; Xiao, X.; Xu, S.; Qiu, J.; Du, J.; Dong, G. Enhanced Single-Mode Fiber Laser Emission by Nano-Crystallization of Oxyfluoride Glass-Ceramic Cores. *J. Mater. Chem. C* **2019**, *7* (17), 5155–5162.
- (19) Fan, X.; Wang, J.; Qiao, X.; Wang, M.; Adam, J. L.; Zhang, X. Preparation Process and Upconversion Luminescence of Er³⁺-Doped Glass Ceramics Containing Ba₂LaF₇ Nanocrystals. *J. Phys. Chem. B* **2006**, *110* (12), 5950–5954.
- (20) Peng, Y.; Zhong, J.; Li, X.; Chen, J.; Zhao, J.; Qiao, X.; Chen, D. Controllable Competitive Nanocrystallization of La³⁺-Based Fluorides in Aluminosilicate Glasses and Optical Spectroscopy. *J. Eur. Ceram. Soc.* **2019**, *39* (4), 1420–1427.
- (21) Aguiar, H.; Serra, J.; González, P.; León, B. Structural Study of Sol-Gel Silicate Glasses by IR and Raman Spectroscopies. *J. Non. Cryst. Solids* **2009**, *355* (8), 475–480.
- (22) 2017-PCCP-Different Dominant Transitions in Holmium and Ytterbium Codoped Oxyfluoride Glass and Glass Ceramics Originating from Varying Phonon Energy Environments.Pdf.
- (23) Astruc, A.; Célérier, S.; Pavon, E.; Mamede, A. S.; Delevoye, L.; Brunet, S. Mixed Ba_{1-x}La_xF_{2+x} Fluoride Materials as Catalyst for the Gas Phase Fluorination of 2-Chloropyridine by HF. *Appl. Catal. B Environ.* **2017**, *204*, 107–118.
- (24) Zhao, J.; Ma, R.; Chen, X.; Kang, B.; Qiao, X.; Du, J.; Fan, X.; Ross, U.; Roiland, C.; Lotnyk, A.; Kienle, L.; Zhang, X. From Phase Separation to Nanocrystallization in Fluorosilicate Glasses: Structural Design of Highly Luminescent Glass-Ceramics. *J. Phys. Chem. C* **2016**, *120* (31), 17726–17732.

- (25) Qiu, J.; Jiao, Q.; Zhou, D.; Yang, Z. Recent Progress on Upconversion Luminescence Enhancement in Rare-Earth Doped Transparent Glass-Ceramics. *J. Rare Earths* **2016**, *34* (4), 341–367.
- (26) Jiajia Cai, M. Y. Up-Conversion Luminescence and Optical Thermometry Properties of Transparent Glass Ceramics Containing CaF₂ Yb³⁺Er³⁺ Nanocrystals.

ISSN (online): 2446-1636
ISBN (online): 978-87-7573-920-2

AALBORG UNIVERSITY PRESS